# Modelling of Flow Phenomena during DC Casting

**PROEFSCHRIFT**

ter verkrijging van de graad van doctor
aan de Technische Universiteit Delft,
op gezag van de Rector Magnificus Prof. dr. ir. J.T. Fokkema,
voorzitter van het College voor Promoties,
in het openbaar te verdedigen op dinsdag 29 november 2005 te 15:30 uur

door

Jan ZUIDEMA

materiaalkundig ingenieur
geboren te Rotterdam.

Dit proefschrift is goedgekeurd door de promotor:

Prof. ir. L. Katgerman

Samenstelling promotiecommissie:

| | |
|---|---|
| Rector Magnificus, | voorzitter |
| Prof. ir. L. Katgerman | Technische Universiteit Delft, promotor |
| Prof. dr. R. Boom | Technische Universiteit Delft & Corus |
| Prof. dr. I.M. Richardson | Technische Universiteit Delft |
| Prof. dr. R.I.L. Guthrie | McGill University Montreal Canada |
| Prof. dr. P.S. Grant | University of Oxford |
| Dr. D.G. Eskin | Netherlands Institute for Metals Research |
| Dr. W. Boender | Corus |

# Contents

# Chapter 1

# Introduction

## 1.1 History of Aluminium

Aluminium was presented at the world exhibition in Paris in 1855. With its high specific strength aluminium is much better suited for aeronautic applications. Because flight was not invented yet, it remained until the 20th century before mass production of aluminium was introduced. In 1900 thousand tonnes of aluminium were produced. The annual amount of primary production from 2003 was 22 million tonnes[1]. Because producing aluminium from aluminium oxide into aluminium is quite energy consuming, it takes about 5 times as much energy per tonne produced compared to iron, one third of the aluminium applied worldwide is recycled. Though only produced for about one and a half century yet today more aluminium is produced than all other non-ferrous metals combined.

## 1.2 The production route from bauxite to billets and slabs

The route from bauxite into aluminium products starts with the Bayer-process [2]. Aluminium oxide is extracted by dissolving bauxite in a heated soda-containing solution. In the Hall/Heroult process aluminium is separated from the aluminium oxide by electrolysis [3]. The produced primary aluminium is cast into billets or slabs for further processing. Recycled aluminium is also remelted and cast into billets and slabs. The billets are feed-stock for the extrusion process [4-7], while the slabs are further processed through milling [8] .

The most common process of making billets and slabs from the aluminium is direct-chill casting or DC Casting [9-11]. This thesis will deal with this process and particularly with the start-up phase of casting. The casting process is complicated in nature due to the coupled convection and conduction phenomena combined with the transformation of molten aluminium into solid. Pure aluminium has a ultimate tensile strength of 40-50 MPa. To get strengths of 300-500 MPa pure aluminium is mostly alloyed with elements such as copper, magnesium, manganese, silicon or zinc. This complicates the production because of a

phenomenon which is called macro-segregation. Macro-segregation is the spatial distribution of alloying elements within the cast product [12].

## 1.3 Overview of topics covered

A short description of the topics covered in this thesis is given below.

**Chapter 2: Process description of DC Casting:**

In Chapter 2 of this thesis the principles of DC Casting are explained. The route from re-melting the primary or recycled aluminium until the finished slabs or billets is described. Also attention is paid to the mathematical description of the physical processes and its implications on the modelling of the process. Although this thesis covers mainly the macroscopic modelling of DC Casting in Chapter 2 also some fundamental aspects of solidification will be covered. Without these aspects it is difficult to understand physical phenomena that are observed during experiments.

An overview of different techniques available for measuring velocities in fluids is also described in this chapter . This literature review was used to decide the method used to measure velocities in molten aluminium alloys as is described in chapter 4.

**Chapter 3: Thermal Boundary Conditions:**

Establishment of the correct thermal boundary conditions is the subject of chapter 3. Inverse calculations based on the results of a laboratory water cooling set-up are used to determine the correct heat transfer functions in the secondary cooling region of the DC Casting process [13-15]. In this region the heat flux goes from almost zero to some mega Watts in only a couple of millimetres.

**Chapter 4: Velocity Measurement Techniques:**

A variety of methods to measure velocity are described. The method most suitable for measuring velocities in DC Casting will be covered in more detail. The design of a probe is given. Results from measurements with the probe in liquid tin are given.

**Chapter 5: Mould Filling:**

The filling stage of DC Casting is described in this chapter. Fully 3 dimensional transient calculations were performed on the start-up of mould filling of a rectangular mould through a combo bag [16]. Several experiments were performed to validate the calculated results. Calculations of the filling are compared to results from  video recordings and temperature measurements taken during the DC Casting experiments.

**Chapter 6: Upstream Fluid Flow Effects :**

Some methods to influence the fluid flow upstream of the mould to be able to remove unwanted particles from the melt are discussed in this chapter. A method employing weirs and dams is described first. A novel approach to remove particles from a stream of liquid aluminium is presented after that [17, 18]. It makes use of

the concept of a cyclone to suspend the heavier particles in the bottom of the separator and swirl the liquid aluminium upwards out of the system.

The thesis will be followed by appendices. The Flow-3D scripts for the calculations are given there. The custom FORTRAN code that is needed for the correct description of the thermal boundary conditions is also given.

## References

1.      www.world-aluminium.org, *International Aluminium Institute Statistical Report*. 2004.
2.      Stobart, P.D., *Centenary of the Hall & Heroult Processes, 1886-1986*. 1986: International Primary Aluminium Institute, London, UK.
3.      Habashi, F., *Hall, Heroult and the production of aluminum*. Canadian Mining and Metallurgical Bulletin, 2002. **95**(1062): p. 109-113.
4.      Siegert, K., T. Kretz, and S. Huber. *Extrusion of aluminium materials*. 2000: VDI-Verlag GmbH, Dusseldorf, Germany.
5.      Storen, S., *The Theory of Extrusion--Advances and Challenges*. International Journal of Mechanical Sciences, 1993. **35**(12): p. 1007-1020.
6.      Field, A. *The extrusion of aluminium*. 1992: Institute of Metals and Materials Australasia, Victoria, Australia.
7.      Radtke, H., *Extrusion of Aluminium Materials: Methods, Tools, Profitability*. Wire World. Int, 1978. **20**(4): p. 156-161.
8.      Molenkamp, J.A., *Milling of Aluminium*. Aluminium (Netherlands) , no. 2, pp. 23-29. Mar. 1990, 1990.
9.      Grandfield, J.F. *DC casting of aluminium: a short review of process development*. 1997: Minerals, Metals and Materials Society/AIME, Warrendale, USA.
10.     Grandfield, J.F. and P.T. McGlade, *DC casting of aluminium: process behaviour and technology*. Materials Forum, 1996. **20**: p. 29-51.
11.     Katgerman, L. and S.C. Flood. *Modelling of DC Casting of Aluminium Alloys*. 1991: Japan Institute of Light Metals, Tokyo,  Japan.
12.     Venneker, B.C.H. and L. Katgerman, *Modelling issues in macrosegregation predictions in direct chill castings*. Journal of Light Metals, 2002. **2**(3): p. 149-159.
13.     Opstelten, I.J. and J.M. Rabenberg, *Determination of the experimental boundary conditions during aluminum DC casting from experimental data using inverse modeling*. in *Light Metals 1999 (USA)*. 1999, Minerals, Metals and Materials Society/AIME. p. 449-457.
14.     Zuidema, J., Jr., I.J. Opstelten, and L. Katgerman, *Boiling Curve Approach for Thermal Boundary Conditions in DC Casting*, in Continuous Casting, K. Ehrke and W. Schneider, Editors. 2000, DGM/WIley-VCH, Weinheim, Germany. p. 138-142.
15.     Zuidema, J., Jr., et al., *Secondary cooling in DC casting: modeling and experimental results*, in *Light Metals 2001 (USA)*. 2001, Minerals, Metals and Materials Society/AIME. p. 873-878.
16.     Zuidema, J., Jr. and L. Katgerman. *Modelling metal-entry in the DC cast process using Flow-3D*. in *Modelling of Casting, Welding and advanced Solidification Processes IX*. 1999. Aachen: Shaker Verlag GmbH.
17.     Zuidema, J., Jr. and L. Katgerman, *Upstream fluid flow effects in aluminium DC casting*, in *Aluminum Alloys 2002: Their Physical and Mechanical Properties Pts 1-3*. 2002. p. 65-70.

18.    Zuidema, J., Jr. and L. Katgerman. *Cyclone Separation of Particles in Aluminium DC Casting.* in *Modelling of Casting, Welding and Advanced Solidification Processes X*. 2003. USA: TMS. p. 607-614.

# Chapter 2

## Modelling and measuring DC Casting phenomena

### *2.1 DC Casting*

Direct chill casting or in its abbreviated form DC Casting is the common process for making aluminium products out of primary aluminium or recycled aluminium. Ingots produced by DC Casting are further processed by rolling or extrusion. Products made by this processing route include aluminium profiles, body parts for airspace, automobiles and packaging sheet. In this chapter the DC Casting process from the melting furnace until the casting station is described. The process line is given in Fig. 2.1. The process starts with the melting of primary aluminium or secondary aluminium and alloying to the desired composition in holding furnaces. The molten aluminium is then transferred to the casting furnace. In the casting furnace the temperature is increased to 50 °C above the liquidus temperature of the alloy. From the casting furnace aluminium is transferred through a launder system to the casting station. During degassing entrapped gases are removed from aluminium by blowing a Argon/Nitrogen mixture through the melt, that is stirred at the same time. In the last part of the launder system grain-refiner is added in the form of wire into the molten aluminium. When big rectangular ingots or slabs are produced, 4 moulds are normally connected to the launder system. When smaller round ingots or billets are produced much more moulds are filled at the same time. As soon as molten aluminium enters the mould, solidification will start at the mould walls and bottom. The hydraulic ram will lower the bottom block when the mould is filled to the desired melt level and the solidified shell has grown thick enough to support the liquid core. The melt level is kept at the same height during the rest of the process. This part of the process is shown in Fig 2.2. When the desired length is reached the furnace is tilted back and the billets are ready for further processing. To achieve high enough production rates, effective cooling is important. This cooling is achieved by a water-jet below the mould on the surface of the just solidified aluminium. This also explains the name for the process: direct chill

casting. The water is chilling the aluminium, thereby enhancing the speed at which solidification takes place.

Production speeds are typically a few centimetres per minute. From about 1 meter length until its final length, casting takes place at quasi steady state. This means that when we are looking at a fixed position in space at the casting system, temperatures and velocities of the aluminium do not change with time. The distance between the isotherm where solidification begins, the liquidus, and ends, the solidus, is different for different alloys.
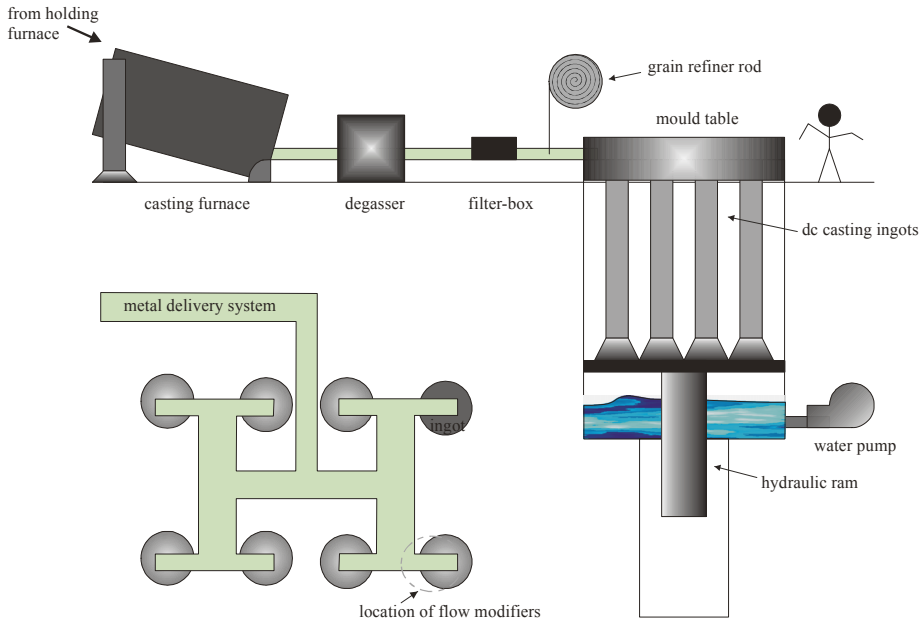


*Fig. 2.1. Layout of a vertical direct chill casting station*

Depending on the alloy system, the temperature difference between the liquidus and solidus can be 50 ℃ or more. For processing this temperature difference between the liquidus and the solidus can cause undesired effects, like macrosegregation and hot-cracking. Macrosegregation is the segregation of alloying elements by convection, causing compositional differences over the cross-section of the ingot. This is an unwanted phenomenon, because mechanical properties are dependent on the chemical composition of the alloy. Hot-cracking is the formation of cracks during the cooling from the liquidus to the solidus temperature. The reason that cracks form in this temperature range has its origin in the permeability of the partly solidified state or mushy state. Solidifying aluminium shrinks upon solidification. When liquid aluminium, flowing through the mushy zone to the solidifying aluminium cannot compensate the shrinkage, a micro-pore will form. This micro-pore can be the initiation of a crack when the internal stresses are high enough. Cracks formed can continuously grow with the casting speed. Another possibility is the formation of a large crack from the

micro-pore at a much lower temperature or even after casting has finished. This is called a cold crack.
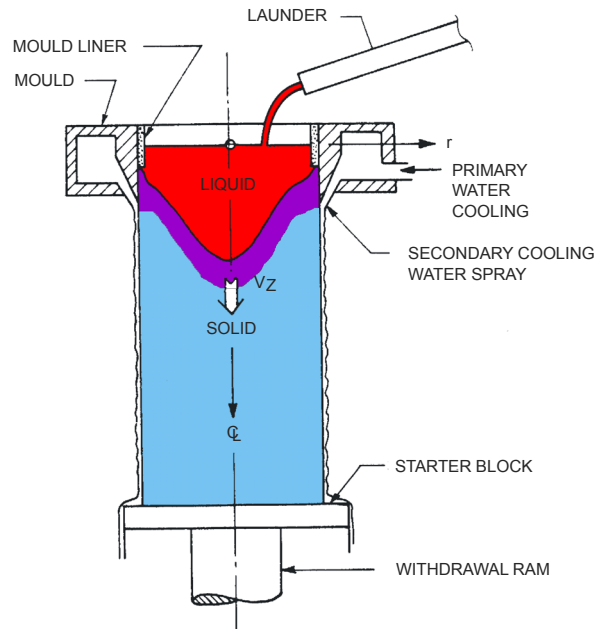


*Fig. 2.2. Schematic representation of DC Casting in steady state.*

## 2.2  Start-up effects

Many defects during DC Casting evolve during the start-up phase of the process. These include [1]:

- Centre cracks and surface cracks.

- Butt curl

- Hang ups

- Bleed outs.

- Surface defects such as cold folding or oxide patches.

- Swell

Higher alloy contents and larger sections will promote the occurrence of these phenomena.

### Cracks

Different kind of cracks can be distinguished. Centre cracks are mostly star shaped and surface cracks grow from the surface towards the centre of the billet. Cracks can also be classified based upon when they were formed. Cracks formed in the region between the liquidus temperature and the solidus temperature are

called hot cracks. Cold cracks are the cracks that are formed below the solidus temperature.

## Butt curl

Because of the very high stresses built up during the solidification contraction, the bottom or butt of the ingot bends up at the sides. This effect is usually called butt curl.

## Hang ups

When molten aluminium freezes to the water-cooled mould, the movement of the aluminium is suddenly interrupted. When only a small amount freezes, the force pulling the bottom block down is big enough to tear of the frozen solid, leaving only a marking of the surface. When the amount of aluminium frozen to the mould is to high, the bottom block will move down, but the ingot will remain attached to the mould. This is a dangerous situation. During the start-up, the butt formation can also cause hang-ups. The formed butt does not fit anymore in the mould and gets stuck.

## Bleed outs

As the butt deforms it can move away from the mould and the cooling water, producing an unsupported and uncooled shell. Because of metallostatic pressure and superheat of the liquid pool liquid is forced through the shell. Similarly gap formation as a result of deformation can allow the metal to escape.

## Surface quality

The surface appearance of billets and slabs is largely affected by mould design, cooling conditions and the casting rate. The main causes of bad surfaces are:

- Unsatisfactory mould surface conditions
- Alloy composition
- Unsuitable casting speed
- Unsatisfactory mould lubricant
- Inefficient methods of level control

## Swell

The cross section of the first part of the casting is approximately 7% greater than the steady state section. This can be the reason for the build up of stress in the solid state.

## 2.3  DC Casting model building blocks

A good numerical model of DC Casting is a model that adequately describes distinct features of the process[2]. To assess the correctness of the numerical model, validation of the results by means of  measurements is necessary. Important process parameters to measure are:

In steady state;

- Sump depth

- Temperatures at characteristic points

- Velocities at characteristic point[*]

During start-up;

- Inlet free surface shape

- Initial velocity[*]

- Temperature as function of time

- Filling rate.


All these process parameters can be determined either directly or indirectly[*]. The velocities can in theory be measured directly, but as described in the chapter on velocity measurements, the technique to do the measurements is not fully developed yet.

## 2.4  Numerical modelling

Modelling the physics of DC Casting gives insight in the process in a way that cannot be achieved by experiments. With modelling of DC Casting some of the phenomena that can be modelled are:


- fluid flow modelling;

- solidification modelling;

- thermo-mechanical modelling.


Thermo-mechanical modelling is used to describe the material behaviour from the formation of a coherent solid structure down to room temperature and will not be covered in this work, but is described by other theses.[3, 4] Modelling fluid flow combined with solidification modelling is described in this thesis.

Aluminium is a metal and therefore not translucent. Seeing the aluminium flow in the mould is restricted to the surface or real-time x-ray techniques must be applied. Knowing the velocity field during casting together with the temperature distribution can help to understand what measures need to be taken to prevent phenomena like macrosegregation and hot cracking. The velocity field and

temperatures during DC Casting can be modelled by solving the equations of momentum and energy together. Good knowledge of the thermo-physical properties of the alloy and the boundary conditions are necessary to solve the equations.

The number of actual experiments needed to verify the models is lower when numerical simulations are used. Validation experiments however cannot be avoided. In the next paragraph the equations that need to be solved will be given. Boundary conditions will be covered at the end of this chapter. Before the transport equations will be described, the basics of the finite volume approach are explained.

## The transport equations

### Continuity

The equations that describe the transport of a continuum are derived from balances that act over a certain volume. The balances that need to be solved are the continuity of mass, momentum and energy. Typically the balances are applied to a very small volume of fluid: a control volume (Fig 2.3). The balance for these quantities states[5]:

$$\Phi_{in} - \Phi_{out} + P = 0, \tag{2.1}$$

where $\Phi_{in}$ is the flux of quantity that enters the control volume, $\Phi_{out}$ is the flux that leaves the control volume and $P$ is the production of that quantity within the control volume. This very simple equation is the basis of the equations of mass, motion and energy. The equations will be given in Cartesian and cylindrical coordinates. When cylindrical coordinates are used $x$ is used to represent the radius $r$ and $y$ is used to represent the angle $\theta$. The equation of mass or the continuity equation is given by

$$V_F \frac{\partial \rho}{\partial t} + \mathbf{AR}\nabla \cdot \rho \vec{v} + \xi \frac{\rho u A_x}{x} = \frac{S_\rho}{\rho}, \tag{2.2}$$

where $\rho$ is the density and $\vec{v}$ is the velocity vector and $\mathbf{A}$ are the fractional areas open to flow. $\mathbf{A}$ is given by

$$\mathbf{A} = diag[A_x \quad A_y \quad A_z]. \tag{2.3}$$

$\mathbf{R}$ is a transformation matrix that is given by

$$\mathbf{R} = diag\left[1 \quad {}^{r_m}\!\!/_r \quad 1\right] \tag{2.4}$$

when using cylindrical coordinates and $\mathbf{R}$ is an identity matrix when using Cartesian coordinates. $\xi$ is 1 for cylindrical coordinates and 0 for Cartesian coordinates.

$S_\rho$ are mass sources.

## Equations of momentum

The equations of momentum (or motion) are given by

$$V_F \frac{\partial}{\partial t} \rho \vec{v} = -\left[\mathbf{AR}\nabla \cdot \rho \vec{v}\vec{v}\right] - \mathbf{R}\nabla p - \left[\mathbf{AR}\nabla \cdot \boldsymbol{\tau}\right] + \rho \vec{g} + \frac{\xi}{x}\vec{T} + S_{\vec{v}},$$ (2.5)

where $p$ is the pressure, $\boldsymbol{\tau}$ is the stress tensor, and $\vec{g}$ is the gravity. The vector $\vec{T}$ is given by

$$\vec{T} = \left[A_x \tau_{xx} - A_y(\tau_{yy} + v^2) \quad A_x + A_y(\tau_{xy} + uv) \quad A_x \tau_{xz}\right]$$ (2.6)

Additional Source terms are given by $S_{\vec{v}}$ in which buoyancy and solidification drag are represented.

### Energy equation

The energy equation is given by

$$V_F \frac{\partial \rho I}{\partial t} + \mathbf{AR}\nabla \cdot \rho I \vec{v} + \xi \frac{\rho I u A_x}{x} = -\mathbf{AR}p\nabla \cdot \vec{v} - \xi \frac{u A_x p}{x}$$
$$+ \mathbf{AR}\nabla \cdot (k\nabla T) + S_I$$ (2.7)

where $I$ is the macroscopic internal energy, $C_v$ is the heat capacity at constant volume, $k$ is the thermal conductivity, and $S_I$ are source terms. In most textbooks the equation of energy is given in terms of enthalpy. For the readers familiar with this approach the energy equation in this form will be given for Cartesian coordinates only. With the help of continuity (Eq. 2.2) and the definition of enthalpy, $H = I + p/\rho$ the following equation can be derived for the energy equation in terms of enthalpy [6]:

$$\rho C_p \frac{DH}{Dt} = \nabla \cdot (k\nabla T) + T\beta \frac{Dp}{Dt} + S_{I'}$$ (2.8)

In this equation the substantial derivative is used for brevity. This substantial time derivative $D/Dt$ is given by

$$\frac{D}{Dt} = \frac{\partial}{\partial t} + \vec{v} \cdot \nabla$$ (2.9)

In (Eq. 2.8) $C_v$ is replaced by the heat capacity at constant pressure $C_p$. The relation between these to quantities is given by

$$C_v = C_p - \frac{\alpha}{\beta \rho},$$ (2.10)

where $\alpha$ is the thermal expansion coefficient and $\beta$ is the isothermal compressibility. Either the energy or the enthalpy balances are used in CFD. For the model either form can be chosen.

### Fluid interface determination

The volume of fluid (VOF) function is used to describe the fluid interface and the free surface. This function $F(x,y,z,t)$ satisfies the equation [7]

$$\frac{\partial F}{\partial t} + \frac{1}{V_F}\left[\frac{\partial}{\partial x}(FA_x u) + R\frac{\partial}{\partial y}(FA_y v) + \frac{\partial}{\partial z}(FA_z w) + \xi \frac{FA_x u}{x}\right] = F_S$$ (2.11)

where $F_S$ is the time rate of change of the volume fraction associated with the mass source for the fluid. The interpretation of $F$ for free surface flow is that where $F=1$ fluid exists and where $F=0$ no fluid exists. This region where $F=0$ is a

region with constant pressure without fluid mass. Physically, this is a vapour or gas region whose density is insignificant with respect to the fluid density.

## Segregation

Macrosegregation of binary alloys can be modelled. The transport equation for the solid-liquid mixture composition , $C_m$, is

$$V_F \frac{\partial C_m}{\partial t} + \left( u A_x \frac{\partial C_l}{\partial x} + v R A_y \frac{\partial C_l}{\partial y} + w A_z \frac{\partial C_l}{\partial z} \right) =$$

$$\frac{\partial}{\partial x}\left( A_x D_l \frac{\partial C_l}{\partial x} \right) + R \frac{\partial}{\partial y}\left( R A_y D_l \frac{\partial C_l}{\partial y} \right) + \frac{\partial}{\partial z}\left( A_z D_l \frac{\partial C_l}{\partial z} \right)$$

$$+ \frac{\partial}{\partial x}\left( A_x D_s \frac{\partial C_s}{\partial x} \right) + R \frac{\partial}{\partial y}\left( R A_y D_s \frac{\partial C_s}{\partial y} \right) + \frac{\partial}{\partial z}\left( A_z D_s \frac{\partial C_s}{\partial z} \right)$$

(2.12)

In this equation $C_s$ and $C_l$ are the composition of the solid and liquid phase respectively, $D_s$ and $D_l$ the mass diffusion coefficients.

## Density evaluation

To be able to correctly describe fluid flow effects occurring during solidification, including macrosegregation, buoyancy forces associated with small density differences are needed. In such cases it is necessary to represent the density as a function of temperature and composition. The density as a linear function of temperature and composition is given by

$$\rho = \rho_0 \left( 1 - \beta_S (c - c^*) - \beta_T (T - T^*) \right). \tag{2.13}$$

In this equation $c$ is the composition of the liquid in the control volume and $T$ is the temperature. The values with a * are reference values. $\rho_0$ is the liquid density at composition $c^*$ and temperature $T^*$. $\beta_S$ is the solutal and $\beta_T$ the thermal expansion coefficient

## Mushy zone approximations

At low solid fraction values, $f_s < f_{s,coh}$, crystals of the solid phase are sparse and float freely in the liquid without forming a coherent solid structure [8]. The solid/liquid mixture can be than approximated as a single fluid with the mixture viscosity dependent on the solid fraction according to

$$\mu = \mu_0 \left( 1 - \frac{f_s}{f_{s,per}} \right)^{-1.55} \tag{2.14}$$

In this equation $f_{s,per}$ is the percolation limit. The percolation limit is the solid fraction above which no liquid movement is possible. Between $f_{s,coh}$ and $f_{s,per}$ the fluid movement is modified by a drag force source term in Eq. 2.5 that is given by

$$K u_i \rho = C_{drg} \frac{f_s^2}{(1 - f_s)^3} u_i \rho \tag{2.15}$$

where the drag coefficient is defined by

$$C_{drg} = \frac{\nu}{\kappa_0} \tag{2.16}$$

In this equation $\kappa_0$ is the commonly used Kozeny-Carman constant in m². When the solid fraction is higher than $f_{s,per}$ then $C_{drg}$ is given an infinitely large number, forcing the velocity to the speed of the solid phase.

**Boundary and initial conditions**

To be able to calculate the DC Casting process we need to specify the boundary conditions of the simulation domain. Necessary information can be provided in different ways. Two types of boundary conditions are important: thermal and inflow. The heat flux at the mould wall and the water-cooling region below the mould for example can be described as function of temperature. and is also dependent on the cooling water conditions. The inflow boundary condition at the top of the mould needs to be taken from experimental practice. The sensitivity of the boundary conditions on the solution of the fluid flow and solidification calculations needs to be determined by variation of those conditions.

**Thermal boundary conditions**

In Chapter 3 the variation methodology is explained for the secondary cooling boundary conditions. The method used is called inverse modelling, because we normally use the boundary conditions to calculate the temperature response in a system and now we have the temperature response and want to know the boundary conditions.

**Inflow boundary conditions**

For the inflow boundary condition a more experimental approach is used. Because the filling of the mould is a transient process it is impossible to measure the velocity using a magnetic probe at the mould entrance. The reason for this will be explained in Chapter 4 on velocity measurements. The velocity can however be approximated from video recordings of the filling stage. By analysing the thickness of the jet entering the mould and the velocity we can make an estimation of the mean size of the jet and filling rate. The inflow boundary condition contains also the temperature at the inlet. The inlet temperature determines the viscosity of the liquid aluminium and thus influences the flow pattern. The influence of all the inflow boundary conditions on the solidification will be assessed in Chapter 5.

**Discretisation and description of the finite volume method**

The equations are not ready for use in computing temperatures and velocities during DC Casting. The differential equations have to be solved with the proper initial conditions and boundary conditions. Closed form analytical solutions to the Navier-Stokes equations do not exist except for some simplified cases[5]. The solution to the NS equations can be found only approximately by discretising the differential equations at a set of points in space. The finite volume method defines a set of small volumes. A set of discrete points within these volumes is defined. The differential equations are discretized using these points. A short description of the finite volume method is given in the next paragraph.

**Description of the finite volume method**

The finite volume method is a method to divide the system we are interested in, e.g. a DC Casting mould, into a number of small connected volumes. These volumes are assumed to have a constant value for all physical variables at a certain time. The properties of a volume can be changed by transport of momentum or energy in or out of the volume or production of momentum or energy inside the volume. When  the DC Casting mould is divided into a number of finite volumes, a number of interior volumes and boundary volumes is created. Interior volumes are volumes completely surrounded by other volumes and boundary volumes are the volumes that are on the outside of the system have at least at one face no neighbour. In order to solve this system initial conditions need to be specified for every volume. For the boundary volumes additional conditions need to be specified. These are called boundary conditions and  specify variables in these volumes and/or gradients of these variables.

**Discretisations used**

The discretisations used by Flow-3D are given here. All discretisations are approximations that can introduce errors. Possible errors are numerical dispersion and numerical diffusion[9]. Numerical diffusion cannot be avoided completely, but when care is taken to use the 'right' scheme it can be reduced substantially.

A first-order approximation of the momentum equation in the x-direction in Cartesian coordinates is given by

$$u_{i,j,k}^{n+1} = u_{i,j,k}^{n} + \delta t^{n+1} \left( -\frac{p_{i+1,j,k}^{n+1} - p_{i,j,k}^{n+1}}{(\rho \delta x)_{i+\frac{1}{2},j,k}^{n}} + gx - fux - fuy - fuz + visx - bx - wsx \right), \qquad (2.17)$$

where the upper indices are the times and the lower indices represent the position in x,y and z direction respectively. In Figs. 2.3 and 2.4 the loci of variables in a control volume and a *x-z* plane of a control volume are shown to clarify the indices used in Eqns. 2.17 and 2.18.
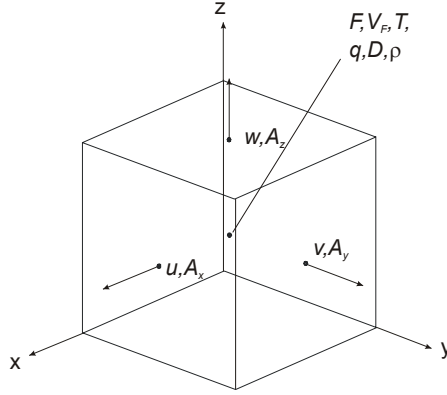
*Fig. 2.3. Location of variables in a mesh cell in Flow-3D.*

In this equation $(\rho \delta x)^n_{i+\frac{1}{2},j,k}$ is given by

$$(\rho \delta x)^n_{i+\frac{1}{2},j,k} = \left(\rho^n_{i,j,k}\delta x_i + \rho^n_{i+1,j,k}\delta x_{i+1}\right)/2 \text{ and} \tag{2.18}$$

*fux, fuy* and *fuz* are the advetive fluxes in *x, y* and *z* direction. The viscous acceleration term is given by *visx*. The flow loss for a baffle normal to the *x*-direction is represented by *bx*. wsx is the viscous wall acceleration in the *x*-direction and *gx* includes gravitational, rotational, and general non-inertial accelerations. For the y- and z-direction similar relations can be written down.
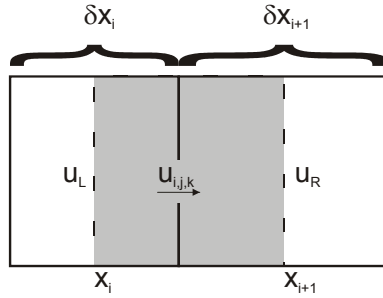


*Fig. 2.4. Control volume in* x-z *plane used in finite-difference approximation for* u *momentum.*

The standard scheme to solve the NS equations is a first order upwind scheme. Because this scheme suffers from numerical diffusion it was not used. Instead a second order monotonicity preserving method was used to solve the differential equations. [7] This scheme requires slightly more CPU time than the first-order method. The scheme computes the value fluxed through a cell face, $Q^\#$, for a variable Q that is advected as

$$Q^\# = Q_i + \tfrac{1}{2} A(1-C)\delta x_i, \tag{2.19}$$

where $Q_i$ is the cell-centred value, C is the Courant number, $\dfrac{u_i \delta t}{\delta x_i}$, and $\delta x_i$ is the

cell size. A is a second-order approximation to the first derivative of $Q$ at the location

$$x_0 = \tfrac{1}{6}(1 - 2C)\delta x_i \qquad\qquad (2.20)$$

within the cell. When the derivatives are second-order accurate then A can easily be computed from two neighbouring first derivatives by linear interpolation. To ensure monotonicity, it is necessary to restrict the value of the derivative A. According to Reference [11], the value of A is not allowed to exceed twice the minimum magnitude of the centred Q derivatives used in its computation,

$$A \le 2\min\left(\dfrac{dQ}{dx_i}, \dfrac{dQ}{dx_{i+1}}\right). \qquad\qquad (2.21)$$

If the two centred derivatives appearing in (Eq. 2.21) are of opposite sign, then A is set to zero and the donor-cell approximation is used.

## 2.5  Verification of the model

For verification of the model a test-case is needed, that has some of the features of the DC Casting case, but on the other hand has an analytical solution. Such a problem is the Smith and Hutton problem that defines a rotating flow through a rectangular cavity (see Fig. 2.5). To verify more features of the model a problem was found that has close resemblance with the flow conditions in the sump of DC Casting. This problem is the driven cavity problem (Fig. 2.6). The model performed reasonable good in both problems [10] although there were better discretisation schemes. The best performing schemes were better, but for the scope of understanding phenomena in DC Casting the numerical scheme chosen in the previous paragraph was accurate enough, while at the same time being relatively easy to implement and moreover quickly converging.
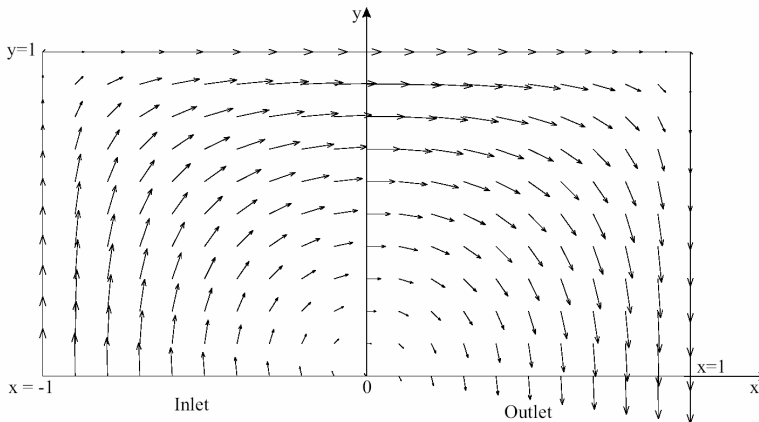


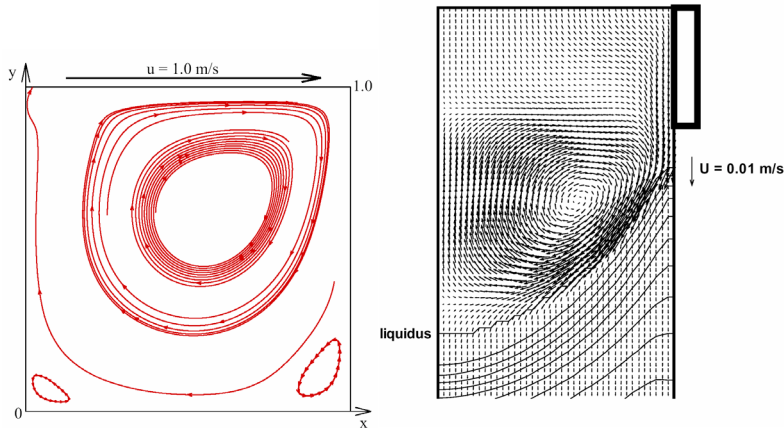*Fig. 2.5. Velocity field in the Smith & Hutton problem.*

*Fig. 2.6. Schematic picture of the driven-cavity benchmark (on the left) showing the streamline pattern of the primary, secondary and additional corner vortices. On the right a calculated results of a vertical slice of a DC Casting of a Al 4.5% Cu alloy is given.*

## 2.6   Validation of the model

With measured data of castings it is possible to validate the different sub models that are in the model of DC Casting. Experiments that simulate distinct features of DC Casting were performed in order to isolate a distinct sub model from the complete model. An example is the validation of the secondary cooling sub model. This model has been developed and validated in a specially designed rig which is described in chapter 3. Another example is the filling of the DC Casting mould at the start of a casting. The bottom block closes down the mould section and liquid aluminium is entering this cavity. The free surface model was validated for this case. In chapter 5, this case is described. Two more cases of DC Casting related problems were investigated to validate the models. The last case is the application of a cyclone for the removal of particles from the launder system. The particle model could be tested and validated for this case. This is described in chapter 6.

## 2.7   Velocity Measurement

One important aspect, that is necessary for validation of numerical results of DC Casting cases, is measurement of the magnitude and direction of velocities during casting. There are numerous methods suitable for measuring velocities, but only a few are in fact suitable for molten metals. In this paragraph on overview is given of a wide variety of techniques available to measure velocities in fluid media. At the end of the paragraph the results are summarized with respect to the applicability of the technique to the case of DC Casting.

### Techniques based on mechanical response

### Pitot tubes

Pitot tubes (named after the French scientist Pitot) offer an extremely simple and convenient method of measuring time-averaged velocities in fluid flows [12]. The basis for the use of Pitot tubes is formed by Bernoulli's equation, which describes the relationship between pressure and velocity of the steady flow through the channel:

$$p + \tfrac{1}{2}\,\rho V^2 + \rho gh = const, \tag{2.22}$$

where $p$ is the pressure, $\rho$ is the density, $V$ is the velocity, $h$ is the elevation, and $g$ is the acceleration of gravity.

This equation gives simple ratio between steady flow parameters for a substance of constant density.
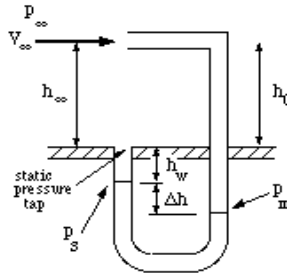


*Fig. 2.7. Pitot tube in a wind tunnel.*

The Pitot tube is one of the simplest and most useful instruments ever devised. It simply consists of a tube bent at right angles (Fig. 2.7). Pitot tubes do not measure the velocity of fluid directly. One can rather measure the dynamic pressure arisen from the flow.

By pointing the tube directly upstream into the flow and measuring the difference between the pressure sensed by the Pitot tube and the pressure of the surrounding air flow, it can give a very accurate measure of the velocity. In fact, it is probably the most accurate method available for measuring flow velocity on a routine basis, and accuracy better than 1% is easily possible.

Fig. 2.8 shows a schematic drawing of a Pitot tube used in aircrafts as speedometers. Several small holes are drilled around the outside of the tube and a centre hole is drilled down the axis of the tube. The outside holes are connected to one side of a device called pressure transducer. The centre hole in the tube is kept separate from the outside holes and is connected to the other side of the transducer. The transducer measures the difference in pressure in the two groups of tubes by measuring the strain in a thin element using an electronic strain gauge.

Since the outside holes are perpendicular to the direction of travel, these tubes are pressurized by the local random component of the air velocity. The pressure in these tubes is the static pressure ($p_s$). The centre tube, however, is pointed in the direction of travel and is pressurized by both the random and the ordered air

velocity. The pressure in this tube is the total pressure ($p_t$). The pressure transducer measures the difference in total and static pressure ($p_t - p_s$), or dynamic pressure $p_d$.

With the difference in pressures measured and knowing the local value of media density ($\rho$) from pressure and temperature measurements, we can use Bernoulli's equation to calculate the velocity:

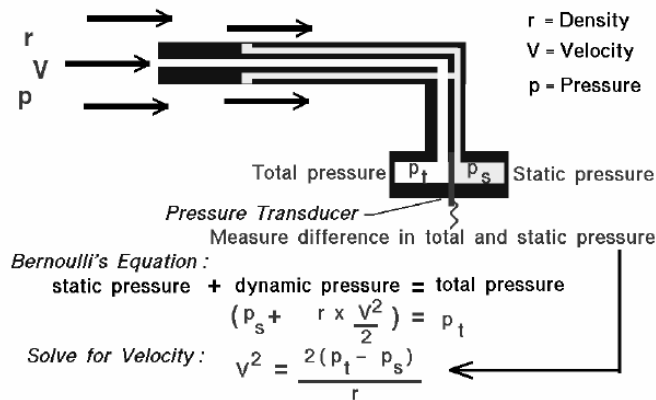$$V^2 = [2 \times (p_t - p_s)] / \rho. \tag{2.23}$$



Fig. 2.8 Schematic drawing of a speedometer of an aircraft.

There are, however, some practical limitations:

First of all the Pitot tube is not adequate for measuring velocities of recirculating flows typical of flows in moulds of DC Casting because this device itself introduces disturbances in the flow pattern. Secondly, the introduction of such a measuring tube in high-temperature and aggressive metallic melts is a difficult task.  In addition, if the velocity is low, the difference in pressures is very small and hard to accurately measure with the transducer. Errors in the instrument could be greater than the measurement! So Pitot tubes do not work well for very low velocities.

At the present time, Pitot tubes are mainly used for measuring velocities in air and gas flows.

**Propeller type velocimeter**

This type of meters was originally developed for measuring water flow velocity in water models. The measurement principle is based on the unique relationship between the rotation speed of a propeller and the velocity of approaching flow. The diameter of the propeller could be as small as 1 mm and, hence the spatial resolution is relatively good and suitable for velocity measurements in water models of continuous casting [13, 14].The use, however, of such a device in the flows of molten metals results in experimental difficulties. First of all, the materials of the propeller and the shaft should be very stable in molten metal, without size and weight distortion.

**Reaction probes**

Velocimeters the measurement principle of which is based on the detection of hydrodynamic drag action on a solid body are called the reaction probes [13].

The mean drag force $F_d$ for a probe is given by the following formula [13]:

$$F_d = C_d \, S \, \rho V^2 / 2, \tag{2.24}$$

where $C_d$ is the drag coefficient, $S$ is the cross-section area of the probe in the direction normal to the measured velocity component, $\rho$ is the fluid density, and $V$ is the mean velocity.

The principle of measuring is quite simple. However, the practical implementation could be tricky. First of all, it is necessary to estimate $C_d$, which generally is the function of three variables [13]:

$$C_d = f(\text{Re}, \text{Tu}, \lambda/D), \tag{2.25}$$

where Re is Reynolds number (Re $= VD/\nu$, here $\nu$ is the kinematic viscosity of the fluid and $D$ is the diameter of the spherical probe); Tu is the turbulence intensity (Tu $= V'/V$, here $V'$ is the mean turbulence component); and $\lambda$ is the turbulence scale.

The drag coefficient can be found in literature or determined experimentally using models. For example, $C_d$ for a rectangular plate with a plane normal to the flow direction changes from 1.12–1.16 (square) to ~2.0 (rectangular with large ratio of side lengths). Fig. 2.9 shows the drag coefficient of a spherical probe as a function of Re and Tu. The solid line denotes the standard drag coefficient [13].
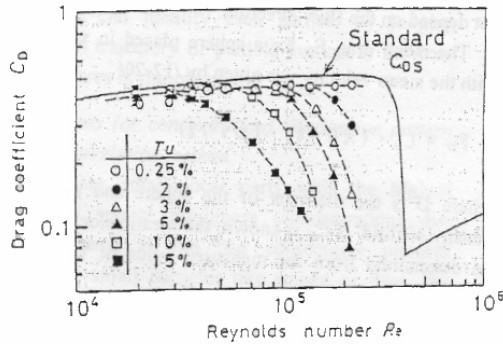


*Fig. 2.9. Drag coefficient of sphere as a function of Re and Tu  [13].*

An example of such a probe [15-18] is given in Fig. 2.10. The principle is that the pressure of the fluid flow on the receiver (plate [15, 17] or sphere [16, 18]) placed in a certain point in the fluid is transmitted to the sensor located outside the fluid. Thus obtained electrical signal is then amplified, processed and recorded in a data acquisition system. The probe (plate or sphere, *1* in Fig. 2.10) is rigidly connected to the arm *2* which transmits the force (pressure) to the spring element *3* with the strain gauge *4*. The spring element is fixed on another rigid arm *5*

enabling its movement and fixation. The probe for measuring the vertical component of the velocity has the attachment *6* with the spring *7* to compensate for the buoyancy. The probe for the horizontal velocity has the attachment *8* allowing the rotation of the probe. The probe itself is made from a material resistant to the melt. This could be tantalum [16, 18], quartz, ceramics or other stable materials.

Different types of sensors can be used to measure the pressure or drag force. In most cases these are strain gauges pre-calibrated using an independent flow meter. The reliability of disk-type probe can be questioned in turbulent flows, as the action of the flow onto the disk changes dramatically with a slight change in the attack angle or the incident angle between the disk plane and the flow direction. Such a shortcoming can be overcome by using a sphere. In this case, the drag does not depend on the flow direction.

The sphere diameter should be large enough to considerably exceed the turbulence scale and small enough to assure the measurement of the local mean velocity. There are several problems which can significantly decrease the reliability and accuracy of the measurements. Among them the buoyancy of the probe and the arm, friction between the fluid and the arm, drag of the arm, solidification of the melt and/or accumulation of oxides on the arm, effect of surface tension of the melt mirror on the drag, etc.
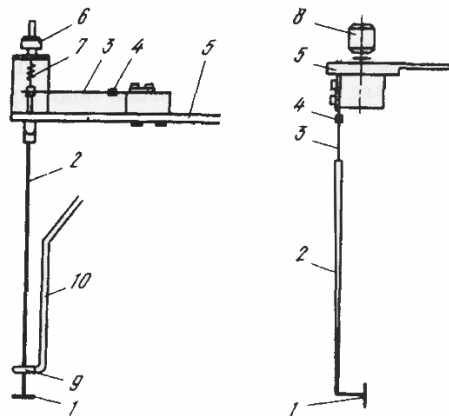


*Fig. 2.10. Diagram of reaction velocimeter with a disk probe: for vertical (left) and horizontal (right) velocity components [15]. Notation is explained in the text.*

Moore [16] designed a reaction perforated-sphere probe and performed experiments on measuring velocities of mercury in an induction furnace. His drag probe consisted of a 6.55-mm perforated tantalum spherical shell with an open area ratio of 0.5. The wall of the shell was less then 0.2 mm thick. The shell was perforated with 48 holes which were deeply countersunk on both sides. The perforation was found to effectively eliminate the effect of vortex shedding and also increase the drag force as compared with the solid shell of the same diameter. A sketch and photographs of the probe are given in Fig. 2.11. The drag force

experienced by the perforated shell and a short connecting rod was transmitted to a thin (0.165 mm) stainless steel beam which was protected from the flow with a stainless steel protective cylindrical shield. The beam thickness was chosen such that at the maximum expected flow velocity the drag force on the shell would produce a bending moment on the beam such that the foil strain gauges, attached at both sides, would produce a total strain of 0.12%. This precaution ensured that the probe was built to maximum sensitivity while at the same time keeping the strain at an acceptable level. The beam was carefully cut and ground in order to prevent any accumulated stresses. High-fatigue-life strain gouges were bonded to both sides of the beam to secure maximum sensitivity and essential temperature compensation. The gauges were then covered with protective coating (silicon rubber compound) to prevent interaction with the liquid. In the final stage of probe construction, a thin rod 0.25 mm in diameter was connected to the beam.

The probe was calibrated in the rotating vessel and the drag force was found to be proportional to the squired mean velocity, Fig. 2.12. The Moore probe was successfully applied to the movement of liquid mercury inside a coreless induction furnace [16].

A similar probe was constructed with a graphite sphere and used in molten metals by Lillicrap [19]. Other known experiments [13, 15, 17] performed using the probe of this type showed that the drag probe can be useful when measuring the velocity of molten metal near the bath surface in the absence of waves. The range of measured velocities is from 0.1 to 1.5 m/s with an accuracy of ± 0.02 m/s [15].
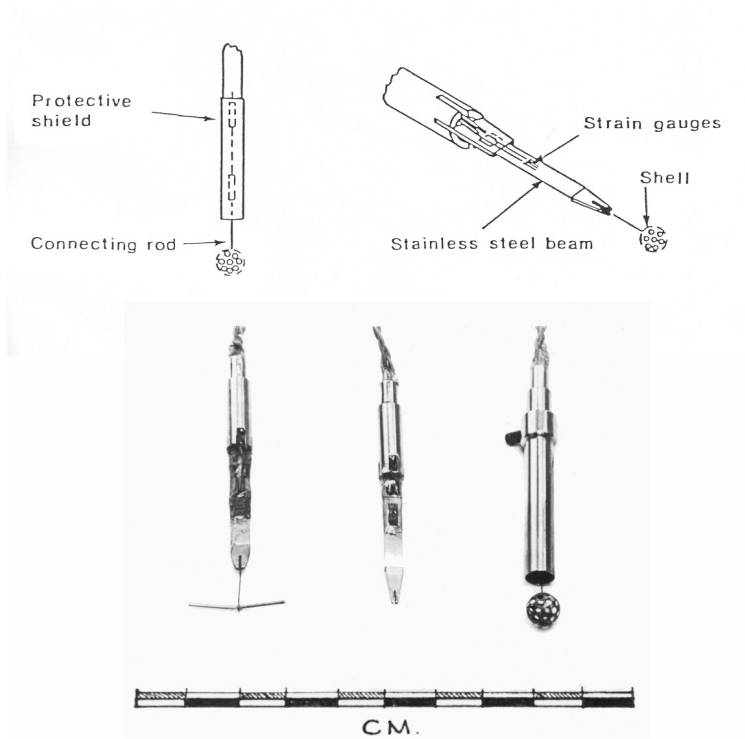
*Fig. 2.11. Top: scheme of the drag probe with (left) and without (right) protective shield and bottom: real probes used by Moore [16].*
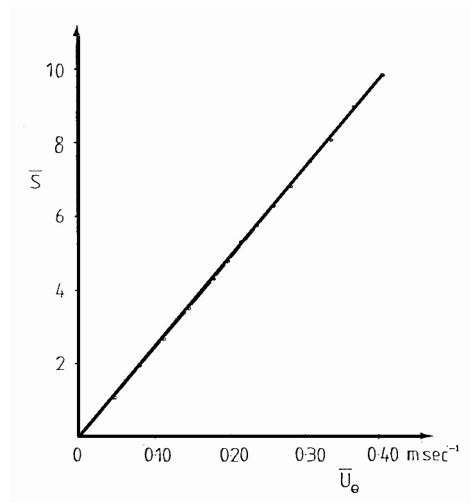


*Fig. 2.12. Calibration plot for the drag probe: $\bar{S}$ is the output signal from a probe and $\bar{U}$ is the mean velocity [16].*

**Karman vortex probe**

When a long circular cylinder is immersed in a free stream with its axis perpendicular to the flow direction as shown in Fig. 2.13, the flow around the cylinder is governed by the Reynolds number. If the Reynolds number Re is larger than approximately 40, vortices are created by the cylinder [13]. These very regular patterns are called Karman's vortex streets. These vortices create a periodical force with the direction normal to the flow direction, which is exerted on the cylinder. As a result, the cylinder begins to oscillate with the same frequency as the shedding frequency of Karman's vortex streets.
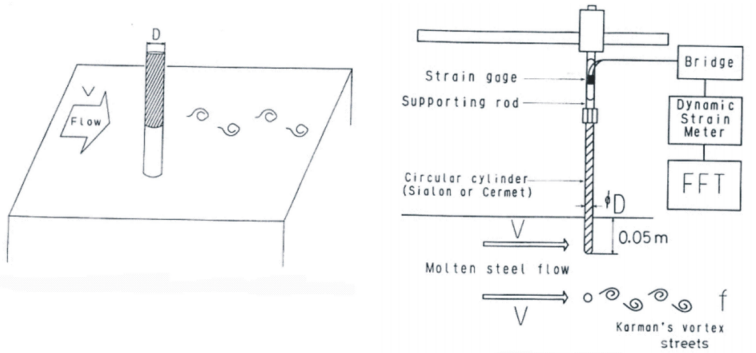


*Fig. 2.13. Origin of Karman's vortex streets behind a cylinder (top) and scheme of Karman vortex probe (bottom) [20].*

The shedding frequency of Karman's vortex streets, $f$, is correlated with the flow velocity, $V$, and the cylinder diameter, $D$, in terms of the Strouhal number St as follows:

$$St = fD/V. \tag{2.26}$$

It is known [13, 20] that St values are almost constant over a wide range of Reynolds numbers of $3 \times 10^2$ to $3 \times 10^5$. When the Reynolds number falls in this range[*], the velocity of the fluid approaching the cylinder can be readily determined by measuring the shedding frequency and using Eq. 2.26.

The oscillation frequency of the cylindrical probe is determined by measuring the strain on the surface of the supporting rod as shown in Fig. 2.13. Iguchi *et al.* [20] point out two advantages of the Karman probe: the measured values are independent of the depth (the depth of cylinder immersion in the melt should be more than 6 times the cylinder diameter) and of the physical properties of the melt (within the mentioned above range of Re). The cylinder can be made of high-temperature ceramics and used in very hot melts. Actually, this probe has been used for measuring velocities of molten steels with a temperature as high as 1600 °C, Fig. 2.14 [13, 20]. The velocities were measured at a depth of 50 mm in the range from 0.2 to 0.7 m/s. Prior to the measurements, the probe should be calibrated, e.g. in water or in a melt of Wood's metal. The array of oscillating

---

[*] During DC Casting of aluminium alloys the Reynolds number of the melt flow varies in the range 500 to 5000.

voltage signal from the probe is processed by fast Fourier analyzer (could be done within LabVIEW software or in Excel) to reveal the shedding frequency. The limiting factor of the Karman vortex probe is that it measures subsurface velocities.

Dring and Jones [21] reported the device based on the Karman-probe principle but enabling simultaneous measurement of the fluid velocity, density and viscosity. Briefly, the system consists of a double-ended tuning fork resonant element with piezoceramic chips fixed to its surface. The resonant element is pre-tensioned in a circular housing to ensure constant Young's modulus. The device is placed behind the bluff body (cylinder) and measures the frequency spectra generated by vortices. In addition, the device acts as another bluff body and produces its own vortices. The damping of the resonator is a function of viscosity and flow rate. This device is quite exotic and has been tested only in air and oil. It requires very accurately maintained conditions, especially pressure and temperature. Therefore, it can hardly be used in molten metals.
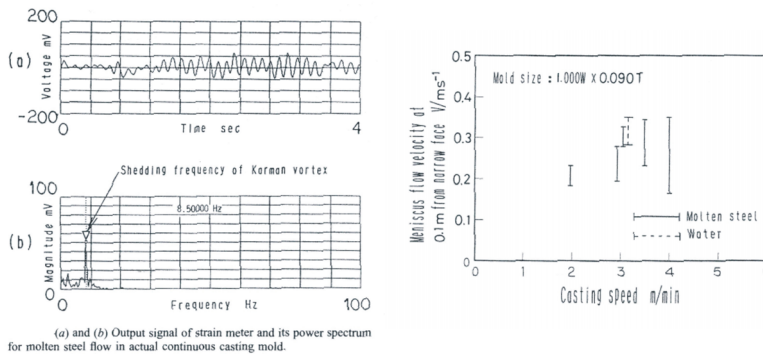


Fig. 2.14. An example of measurements performed on molten steel (a, b) and the relation between meniscus flow velocity and casting speed upon DC Casting of a steel slab 1 × 0.09 m [20].

**Mechano-optical technique**

Zhilin et al. [22] suggested and Eckert et al. [23] further developed a technique for measuring local velocities in opaque fluids. This technique is based on the separation of a direct mechanical interaction between the flow and the sensor tip and the optical acquisition and processing of the signal. The method was tested at temperatures as high as 350 ºC (Pb–Bi and Sn–Bi melts).

The measuring device consists of a mechanical sensor, which is in the direct contact with the fluid, mounted rigidly on an optical system used to acquire the data (Fig. 2.15). The thin tip of the probe (50 μm dia.) acts as a sensitive part. It is formed as a thin-walled glass cone. A small glass rod (pointer) with a length of about 30–40 mm is placed inside this glass tube and connected with the sensor tip only at the front over a length of approximately 1 mm. The initial position of the free end of this pointer is in the centre of the glass tube. The moving fluid elastically deforms the tip as shown in Fig. 2.15. Consequently, the free end of the pointer shifts inside the tube, and this displacement can be registered optically. This deflection is a function of the fluid velocity at the tip position. The evaluation of the amplitude and the direction of the pointer displacement allows one to

resolve two velocity components perpendicular to the sensor axis. An endoscope combined with a special lens system and a CCD-array (the silicon <u>C</u>harge-<u>C</u>oupled <u>D</u>evice) is used to observe the pointer image. The pictures are digitized and analyzed frame-by-frame.

Obviously, the used material should be stable in the melt and its elastic characteristics should be stable within the used temperature range. For temperatures below 350 ℃, borosilicate glass has been used. However, quartz glass should be tested for higher temperatures (up to 1000 ℃).

The basic principles for determining the velocity are the same as in the case of reaction probes.

The deflection $h$ of the sensor tip can be written as [23]:

$$h = (C_w \rho v^2 l^4)/(2E\pi r^2 \delta), \tag{2.27}$$

where $C_w$ is the drag coefficient that can be determined during calibration tests; $l$, $r$ and $\delta$ are the length of the tip, the radius of the tube tip and the thickness of tube wall, respectively; $\rho$ is the fluid density; $E$ is the Young modulus of the glass; and $v$ is the fluid velocity.
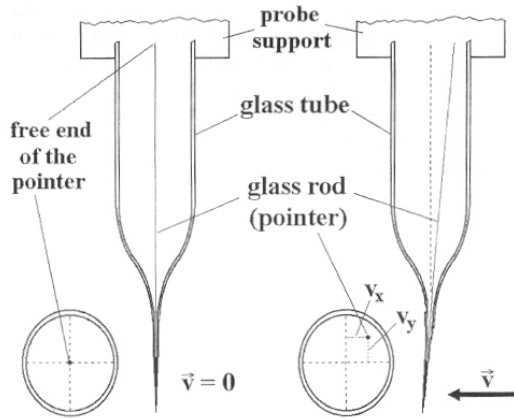


*Fig. 2.15. Measuring principle of the mechano-optical probe [23].*

The deflection of the sensor tip can be derived from the measured displacement of the pointer free side.

The sensitivity of the sensor can be further increased by attaching a small sphere to the sensor tip. In this case Eq. (2.27) can be rewritten as:

$$h = (C_w \rho v^2 r_s^2 l^3)/(6Er^3 \delta), \qquad\qquad \text{Eq. (2.28)}$$

were $r_s$ is the radius of the sphere (e.g. 1 mm).

The use of the sphere increases the sensitivity of the probe by a factor of three [23] as shown in Fig. 2.16.

The test of this technique on eutectic InGaSn melt driven by rotating magnetic field [23] showed that the probe is insensitive to electrical noise and external

magnetic fields and capable of measuring fluid velocities in the range 0.03–0.25 m/s.
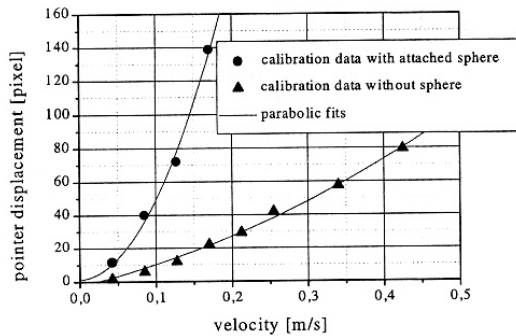


*Fig. 2.16. Calibration data obtained with a mechano-optical sensor in water with and without a sphere attached to the sensor tip [23].*

## Techniques based on particles-tracers

### Particle imaging velocimetry

The technique of particle imaging velocimetry (PIV) is widely used for measuring velocities of transparent media due to the following advantages [13]:

- instantaneous measurement of the entire flow field;

- contact-free (non-intrusive) measurement;

- easy extraction and processing of physical information through velocity data;

- applicability for a wide range of velocities, from slow flows to supersonic speeds.

The term "velocity" used in PIV is in fact the velocity of particle motion or the moving velocity of local fluid elements with certain particle concentration distribution. The particle velocity can be taken as the fluid flow velocity only when the particle or particle concentration distribution pattern moves with the fluid flow without relative velocity.

Whenever any technique of PIV is applied, the fluid flow is visualized by one of the existing visualization techniques, and then the digital images are processed in a computer. The techniques of PIV can be classified as follows [13].

*Multiple exposure technique*

Within this technique the velocity of a particle can be measured directly by dividing the particle path length with the exposure time (path line method) or from the distance between particle images photographed in a stroboscopic light and the pulse interval (stroboscopic method).

*Methods using consecutive time step images*

In "four-consecutive-time-step" particle tracking velocimetry (PTV), the flow patterns formed by particles-tracers are photographed at short time intervals, each particle is tracked and identified, and then the particle velocities are calculated. The identification of a particle is based on the smoothness of its apparent trajectory.
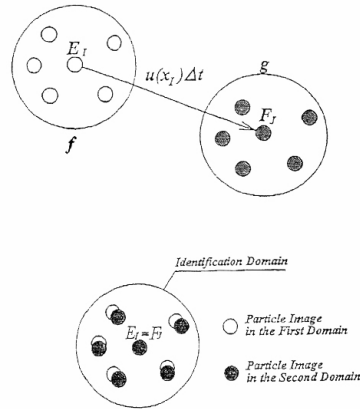


*Fig. 2.17. Principle of cross-correlation technique of PIV [13].*

In "brightness (or concentration)-distribution-pattern" cross-correlation method, the velocity is calculated from the movement of small local parts with highest brightness similarity in two consecutive pictures. In this case the image cross-correlation method is used.

The essence of the cross-correlation technique is described in Fig. 2.17. We assume that the time interval between two consecutive pictures is short enough and fixed and that flow velocities do not change abruptly, hence, the similarity of flow patterns is preserved. Suppose that coordinates of all particles in pictures $f$ and $g$ are determined. The principle of particle identification is based then on finding out the best similarity in the distribution patterns around a reference particle in first picture and a candidate particle in the second picture. In order to estimate the similarity in the two particle-distribution patterns $f$ and $g$, the following cross-correlation coefficient is used $C_{fg} = L/(nm)^{1/2}$, where $n$ and $m$ are the particle numbers in the correlation domains at time $t$ and $t + \Delta t$, respectively, and $L$ is the sum of logical products in the two sub regions $f$ and $g$.
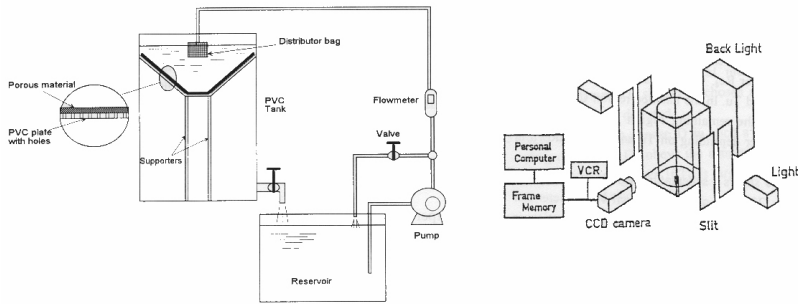
*Fig. 2.18. Sketch of the physical model of DC Casting and PIV setup used by Xu et al.[24].*

PIV was used numerously for studying the flow patterns in water models of casting. For example Xu *et al.* [24] applied PIV for the physical model of DC Casting of aluminium. They used the setup shown in Fig. 2.18. The illumination of the transparent PVC mould with water and latex particles (150–200 μm) was performed through a slit collimator by a halogen light source. The images were recorded by a CCD camera connected to a computer. The frame-to-frame movement of particles images was analyzed by PIV software to produce vector plots of velocities (Fig. 2.19) over an interval of 33 ms between frames.
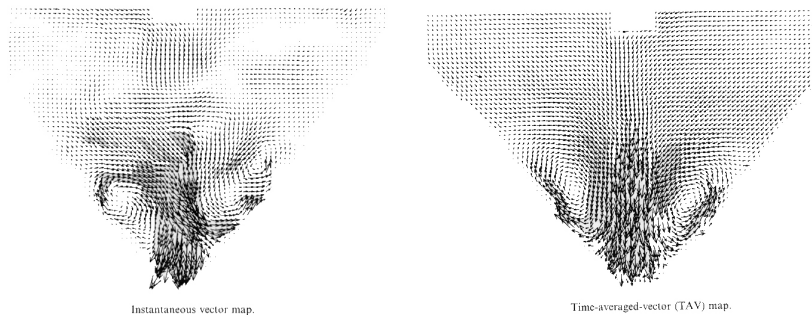


*Fig. 2.19. Example of flow velocity patterns in the sump of DC Casting (water model) [24].*

For obvious reasons the PIV cannot be used for direct studies of flow patterns and velocities in real molten metals. However, the flow velocity on the surface of a molten metal bath can be measured by recording tracer motions on the bath surface and subsequently processed using one of the mentioned PIV methods.

Molten metal velocities inside the opaque liquid bath can be measured by tracing radio-isotopic particles using radioscopy. Koster *et al.* [25] have developed a radioscopic technique allowing one to monitor real-time convection in opaque liquids (gallium melts).

**Doppler velocimetry**

Doppler velocimetry uses the Doppler effect of laser beams or ultrasonic wave reflected from a moving body. Laser Doppler velocimetry (LDV) is widely used in

a variety of engineering fields, e.g. in water model experiments for continuous casting moulds and launders. This optical technique makes it possible to measure the local instantaneous velocity of tracer particles suspended in the flow [13]. These tracer particles should be small in order to prevent interference with the genuine flow pattern and to follow the fluid motion. The modification of LDV is a phase Doppler velocimeter in which two lasers are used to obtain information both on the velocities and the size distribution of particles [26].

The use of ultrasound waves has obvious advantages over laser [27]: efficient instantaneous flow mapping (velocity field map); applicability to opaque fluids; and record of the spatiotemporal velocity field without prior knowledge of the flow. Therefore, let's consider this technique in more detail.

Fig. 2.20 shows a common configuration of the ultrasound beam and flow. The UDV method is based on pulsed ultrasound echography. An ultrasound pulse is emitted from the transducer along the measuring line, and the same transducer receives the echo reflected from the surface of micro particles suspended in the liquid.

All velocity profile information is contained in the echo. Information on the position from which the ultrasound is reflected, $x$, is extracted from the time delay $\tau$ between the start of the pulse burst and its reception:

$$x = c\tau/2, \tag{29}$$
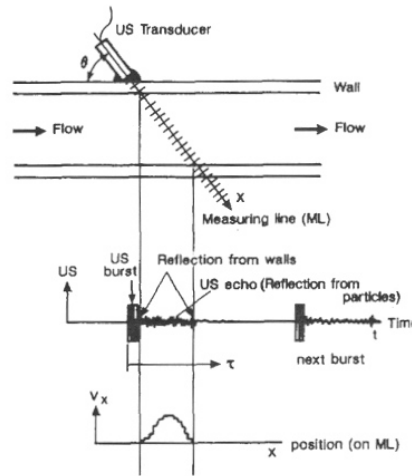
where $c$ is the speed of sound in the media.



Fig. 2.20. Principle of UVP: arrangement between an ultrasound beam and a flow in a channel (top); echo signal (middle); and reconstructed velocity profile (bottom) [27].

At the same time, the velocity information is derived from the Doppler shift frequency at that instant:

$$V = c f_D / 2 f_0, \tag{30}$$

where $V$ is the velocity of the particle; $f_D$ is the Doppler shift velocity; and $f_0$ is the basic frequency of ultrasound.

Thus the velocity profile can be obtained by analyzing the echo signal. In practice, the echo signal is processed after acquiring a set of data (e.g. scanning 128 channels simultaneously [27]):

$$[2\pi f_D(\tau_i)], \tag{31}$$

this is converted to the velocity profile V($x_i$) using Eqs. (29) and (30).

The essential part of this method is to detect the Doppler shift frequency as a function of time. Since Doppler shift occurs within a much shorter time than the time period corresponding to the required spatial resolution, it is difficult to obtain these frequencies with high resolution from a single echo. Takeda [27] suggested to use a special procedure that included repeated pulse emission, filtering out the basic ultrasonic frequency, sampling the echo with a construction of a waveform, and the processing of this waveform to obtain the velocity profile.

The limiting condition for the method can be written as follows [27]:

$$V_{max}P_{max} < c^2/8f_0, \tag{32}$$

where $V_{max}$ is the maximum detectable velocity and $P_{max}$ is the maximum measurable depth.

One of the used UDV systems had the following characteristics (for water) [27]:

| | |
|---|---|
| Basic frequency | 4 MHz |
| Maximum measurable range | 75 cm |
| Maximum velocity | 75 cm/s |
| Spatial resolution | 0.75 mm |
| Velocity resolution | 0.75 mm/s |
| Number of channels | 128 |

The ultrasonic Doppler velocimetry (UDV) has been successfully used in water, liquid mercury, Pb–Bi melts and some water solutions [27-29]. However, it has not been yet tested for liquids with temperatures higher than 200 ºC.

**Magnetic velocity probe**

The principle of a magnetic velocity probe is simple. When a conductor moves trough a magnetic field, it generates an induction current, which gives rise to a potential difference over this conductor. The conductor in this case of molten metals is a liquid metal and the magnetic field is caused by a permanent magnet. The potential which is measured perpendicular to both the axis of the magnetic field and the component of the velocity, in which we are interested, increases

linear with the magnitude of this velocity component. This will be explained in next paragraph.

**Mathematical Framework**

A technique based on Ohm's law can be used to calculate fluctuating velocity vectors in liquid aluminium. Ohm's law states [30]

$$\underline{j} = \sigma\left(\underline{E}_e + \underline{E}_{th} + \underline{u} \times \underline{B}\right), \tag{2.33}$$

with electrical current density $\underline{j}$, specific conductivity $\sigma$, electrostatic field $\underline{E}_e$, thermoelectric field $\underline{E}_{th}$, fluid velocity $\underline{u}$, and magnetic induction $\underline{B}$. Taking the divergence of Eq. (2.33) and expressing the electrical fields in terms of the gradient of the corresponding potentials, i.e. $\underline{E}_e = -\nabla\Phi$ and $\underline{E}_{th} = -\nabla\Psi$ leads to the Poisson equation for $\Phi$ [30]

$$\nabla \cdot \sigma\left(\nabla\Phi + \nabla\Psi - \underline{u} \times \underline{B}\right) = 0, \tag{2.34}$$

because the divergence of the current density is small for low-frequency fields such as considered here.

A sketch of the probe based on this principle is given in Fig. 2.21. The probe [30] consists of a permanent magnet with high coercive force fixed in a conducting tube with an outer diameter of 2.5 mm and of three thermocouples. The magnet itself has a diameter of 2 mm and contains two grooves and a central hole to accommodate the thermocouples.

Two grounded thermocouples (K-Type, Chromel-Alumel) with their tips reduced to 0.27 mm diameter are located at opposite sides of the magnet at points 1 and 2 in Fig. 2.21. These two thermocouples are threaded through small holes (0.3 mm diameter) into the stainless-steel sheath, so that their tips have direct contact with the liquid metal over a length of 0.1-0.2 mm. Because of the good thermal contact of grounded thermocouples, which means that the junction of the Alumel and Chromel wires is directly welded to the sheath of the thermocouple, a very short thermal response time of the probe can be achieved for temperature as well as velocity measurements. The Alumel and the Chromel wires of thermocouples Tc1 and Tc2 enable local electrical potential measurements to be made. At the tip of the probe one additional projecting thermocouple, point Tc3 in Fig. 2.21, is installed to measure the nearly undisturbed temperature of the flow. Similar probes, having four thermocouples at the edges of the magnet, to measure two velocity components have also been manufactured and tested. They require, however, further development and are not covered by the following discussion.
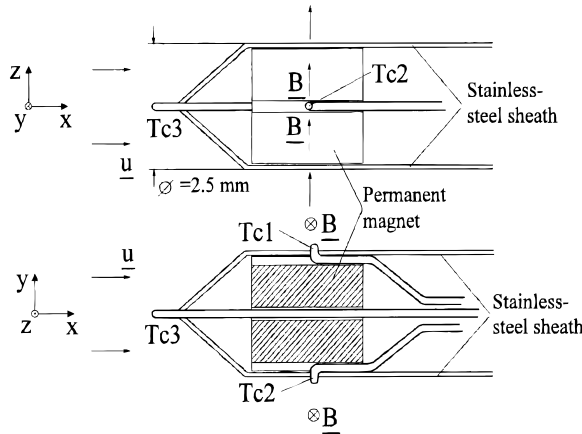
*Fig. 2.21. Sketch of magnetic velocity probe reproduced from Kapulla et al. [30].*

The solution of Eq.34 can be found by Green's function method as shown by Kapulla *et al.* [30]. The thermoelectric potential for a homogenous material can be expressed as

$$\Psi = \int_{T_0}^{T} S(T^*) \, \mathrm{d}\, T^* \, , \tag{2.35}$$

with Seebeck coefficient $S$ and temperature $T$. For the probe the following idealized equation for the potential difference between point 1 and 2 is given

$$\Phi_1 - \Phi_2 = K u_x - S_e (T_1 - T_2), \tag{2.36}$$

with the calibration factor $K$, the instantaneous x-component of the velocity $u_x$ averaged over the influence range of the magnetic field, an effective Seebeck coefficient $S_e$, which takes into account effects of the probe and fluid, and the temperature difference between points 1 and 2.
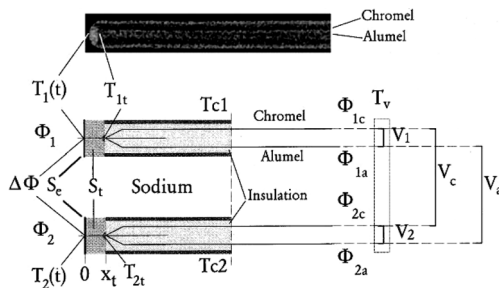


*Fig. 2.22. X-ray image of a thermocouple with the wires welded to the sheath in the upper part and electric schematic of the probe in the lower part. Reproduced from Kapulla et al. [30]*

Because of the finite dimension of the thermocouple, Fig. 2.22, a frequency-dependent damping and a frequency-dependent delay time between the surface temperature and the measured temperature occurs, see Fig. 2.23.

This delay can be compensated for by using a first-order, one dimensional, thermocouple model, which is described by the differential equation [30]

$$\tau \frac{dT_t}{dt} + T_t = T(t),$$  (2.37)

with the time constant $\tau$, the temperature at the thermocouple surface $T(t)$ and the measured temperature $T_t$. The frequency-dependent damping (fdd) for an applied temperature fluctuation with frequency $f = 2\pi\omega$ [30]

$$|F_t| = \frac{1}{\sqrt{1 + \omega\tau}}$$  (2.38)

and the frequency-dependent phase shift (fdps)

$$\tan\varphi = -\omega\tau$$  (2.39)

of the transfer function are shown in Fig. 2.23 for measured time constants $\tau = 4$ and 8 ms for thermocouples with tip diameters of 0.25 and 0.5 mm, respectively.
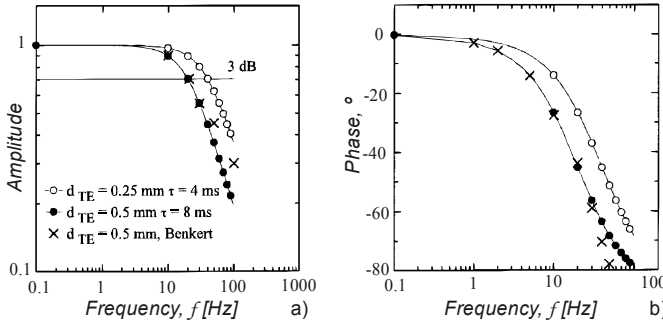


*Fig. 2.23. The frequency-dependent damping and phase shift as function of frequency for two different thermocouples calculated with the thermocouple model. The results are compared to a complex multilayer thermocouple model. The data is reproduced from Kapulla et al. [30].*

The equations for the measured time-dependent potential differences at the cold ends of the thermocouple wires can now be derived:

$$V_a = \Phi_{1a} - \Phi_{2a} = \underbrace{Ku_x}_{(1)} + \underbrace{(S_a - S_t)(T_{1t} - T_{2t}) + (S_t - S_e)(T_1 - T_2)}_{(2)} + V_{a0} + N_a,$$  (2.40)

$$V_c = \Phi_{1c} - \Phi_{2c} = Ku_x + (S_a - S_t)(T_{1t} - T_{2t}) + (S_t - S_e)(T_1 - T_2) + V_{c0} + N_c,$$  (2.41)

$$V_1 = \Phi_{1c} - \Phi_{1a} = \int_{T_v}^{T_{1t}} (S_c - S_a) \, dT + V_{10} + N_1,$$  (2.42)

$$V_2 = \Phi_{2c} - \Phi_{2a} = \int_{T_v}^{T_{2t}} (S_c - S_a) \, dT + V_{20} + N_2,$$  (2.43)

with probe sensitivity or calibration factor $K$, Seebeck coefficients $S_a$ for Alumel and $S_c$ for Chromel, effective Seebeck coefficient $S_e$ across the probe and $S_t$ effective Seebeck coefficient of the thermocouple tip.

In all these equations, extra terms $V_{i0}$ and $N_i$ have been added to account for offsets and noise, respectively. The former include thermoelectric material non-uniformities as well as deviations from standard properties and electronic offsets, whereas the latter contain time-dependent external electromagnetic perturbations and internal electronic noise of the measurement system. The equation for Tc3, which has the same form as Eqs. (2.42) and (2.43), has not been included because it is not needed for velocity measurements.

**Time averaged velocities**

If the time over which the velocity is averaged is long compared to the response time of the thermocouples, then for the mean temperature difference across the probe can be written

$$\overline{\Delta T} = \overline{T}_1 - \overline{T}_2 = \overline{T}_{1t} - \overline{T}_{2t}. \tag{2.44}$$

Taking the mean values of Eqs. (2.42) and (2.43) and linearising the difference of the integrals also yields the mean temperature difference across the probe

$$\overline{\Delta T} = \overline{T}_1 - \overline{T}_2 = \frac{\overline{V}_1 - \overline{V}_2 - \left(\overline{V}_{10} - \overline{V}_{20}\right)}{S_c - S_a}. \tag{2.45}$$

Inserting Eqs. (2.44) and (2.45) into Eqs. (2.40) and (2.41), taking the time average and collecting terms leads to the following equations for the mean-velocity determination:

$$K\overline{u}_x = \underbrace{\overline{V}_a}_{(1)} + \underbrace{S_g\left(\overline{V}_1 - \overline{V}_2\right)}_{(2)} - \underbrace{S_g\left(\overline{V}_{10} - \overline{V}_{20}\right)}_{(3)} - \underbrace{\overline{V}_{a0}}_{(4)}, \tag{2.46}$$

$$K\overline{u}_x = \overline{V}_c + \left(1 - S_g\right)\left(\overline{V}_1 - \overline{V}_2\right) - \left(1 - S_g\right)\left(\overline{V}_{10} - \overline{V}_{20}\right) - \overline{V}_{c0} \tag{2.47}$$

where

$$S_g = \frac{S_e - S_a}{S_c - S_a}. \tag{2.48}$$

Term (2) is the temperature compensation term. If there exist non-uniformities in the Chromel and Alumel conductors terms (3) and (4) are non zero. For a zero temperature gradient, $\overline{\Delta T} = 0$, terms (2) and (3) compensate each other because of Eq. (2.45). The calibration factor $K$, as well as the contributions of the offset values, $\overline{V}_{10}$, $\overline{V}_{20}$, $\overline{V}_{a0}$ and $\overline{V}_{c0}$ must be determined experimentally.

**Evaluation of fluctuating velocities**

For measurement of fluctuating quantities the phase shift and damping between the measured temperatures and the temperatures at the tip of the thermocouples must be known. A complete description of the procedure of measuring these velocities is given in Kapulla et al. [30].

**Non-linearity of the probe**

The magnetic Reynolds number $Re_m$ is defined by

$$Re_m = \mu \sigma L_0 U_0. \tag{2.49}$$

It represents the ratio of the induced field to the field of the magnet itself. For $Re_m \ll 1$ the influence of the induced magnetic field on the velocity field can be disregarded. Von Weissenfluh [31] shows for a spherical magnet with radius $R$ that at $5R$ from the surface of the sphere the magnetic field is weak enough not to disturb the flow. With $\mu = 4\pi \cdot 10^{-7}\,\mathrm{VsA^{-1}m^{-1}}$, $\sigma = 7.5 \cdot 10^6\,\Omega^{-1}\mathrm{m^{-1}}$, $U_0 = 1.0\,\mathrm{m\,s^{-1}}$ and $L_0$ $= 12R$ a magnetic Reynolds number of 0.057 is obtained.

The magnetic force in the fluid is given by

$$\underline{F} = \underline{j} \times \underline{B} \tag{2.50}$$

Ricou and Vives [32] showed that $j \cong 0$ in Eq.(2.50). These authors also measured the pressure profiles in a mercury flow for Reynolds numbers between 50 and 15000 for a magnetic probe and a non-magnetic cylinder with the same dimensions. The profiles are similar and thus it can be concluded that the boundary layer is virtually unchanged by the magnetic field.

**Calibration of the magnetic probe**

The calibration of the magnetic probe is done in a liquid metals flowing with known velocity. If the velocity is unknown, then the flow rate has to be known. The velocity profile has to be measured in that case. In Fig. 2.24 a calibration curve for different liquid metals is given. This figure is reproduced from Ricou and Vives [32]. From Eqs. (2.46) and (2.47) can been seen that in the case of a constant temperature in the calibration flow section only terms (1) and (4) at the RHS are non-zero. The results in Fig. 2.24 show the linearity of the probe.
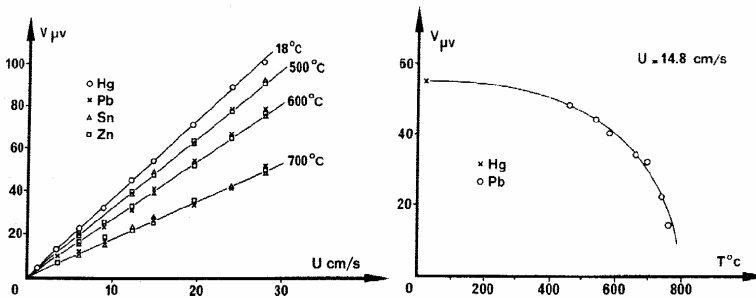


*Fig. 2.24. Calibration of a magnetic velocity probe. Figure reproduced from Ricou and Vives [32]. On the left the potential as function of velocity for different metals at constant temperatures is given. On the right the response of the probe as a function of temperature for a constant velocity is given.*

Because the potentials measured are in the microvolt range the date acquisition has to be done by a nano-voltmeter. Also disturbances from the mains frequency of 50 Hz have to be filtered out. In Kapulla *et al.* [30] data was sampled at 150 Hz. This potential data was amplified 10,000 times by a four-step amplifier having an input noise level of 20 nV. Then the data was filtered by a low-pass filter. RMS-velocities down to 1 mm/s, corresponding to 100 nV, are measured and the accuracy for steady state situations is about 6 mm/s.

### Techniques based on other principles

#### Melting probe

Argyropoulos *et al.* [33-35] developed an original probe based on the melting rate of a metal sphere immersed in molten metal flow. This technique uses metallic sphere of identical chemical composition with the liquid metal in which velocity measurements are to be performed. The sphere is attached to an assembly. A detailed schematic diagram of the sphere assembly that was used for measuring velocity in liquid aluminium is shown in Fig. 2.25.
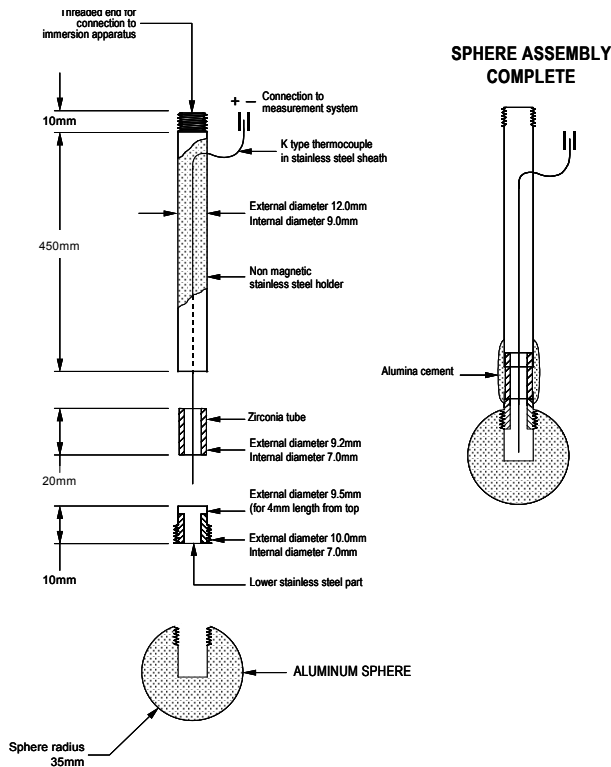


*Fig. 2.25. Sphere assembly for measuring velocity in liquid aluminium [33].*

This metallic sphere is immersed in liquid metal, and the sphere melting time at the specific immersion point is experimentally measured and is directly related to the metal velocity. Fluid velocities between 0.1 and 0.5 m/s were measured in liquid aluminium [34, 35].

The relationship between metal velocity and sphere melting time is determined by performing proper calibration experiments in the same liquid metal system, where the melting time of the sphere is correlated to the metal velocity. Two sets of calibration experiments were carried out. In the first set, the metallic sphere was stirred in a stagnant liquid metal with constant tangential velocity. In this case, the velocity on the sphere was imposed and controlled externally. A schematic cross section of the apparatus used for stirring spheres in aluminium bath is depicted in Fig. 2.26 *a*. In the second set of tests, the sphere assembly was held stationary in

the metal bath, which was moving past the sphere with known velocity. Fig. 2.26 *b* shows a schematic cross section of the apparatus used for this second set of tests. This apparatus is called annular channel unit (ACU) and is described in detail in reference [36]. Fig. 2.27 *a* and *b* present some typical results from the first and second set of calibration experiments.

The sphere melting technique was also applied for measuring velocity in liquid steel. It should be, however, noted that the melting probe is very sensitive to the fluctuation of molten metal temperature. At the present moment, this probe is suitable for measuring an average velocity without taking into account its direction, although some works in this direction are claimed to be on the way [33].
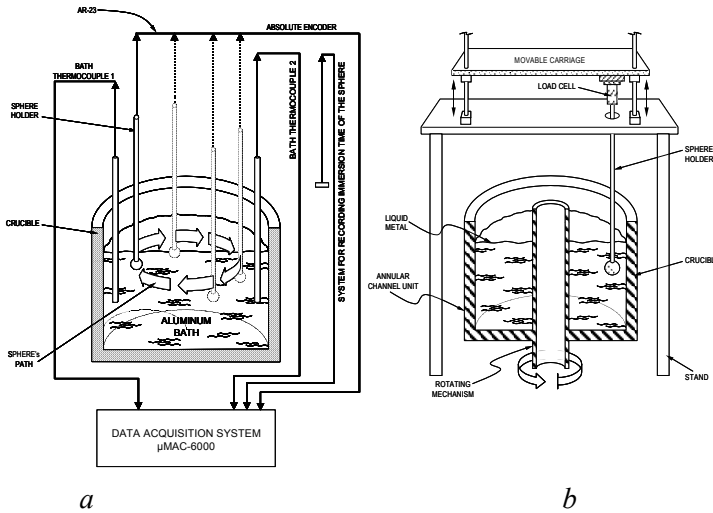


*Fig. 2.26. Schemes of the apparatus used for calibration (a) by stirring the probe in molten aluminium and (b) annular channel unit [36].*
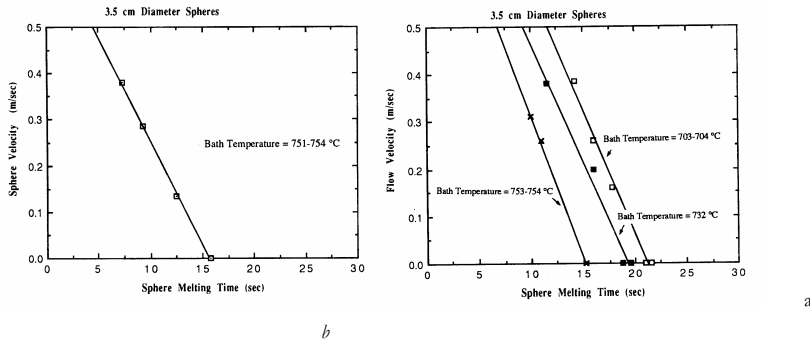


*Fig. 2.27. Typical results of calibration experiments in liquid aluminium for calibration setups shown in Fig.?? (a and b, respectively) [33]*

## Hot wire/film anemometers

There is a unique relationship between the heat transfer from a heated wire (or a heated film) and the velocity of a flow approaching this wire. Hot wire/film

anemometers rely on this relationship and work well when the heat transfer rate is controlled by forced convection.

Hot wire/film anemometers are mainly used in fluids or gases with laminar flow, uniform temperature distribution, and at temperatures below 100 ᵒC [23]. With respect to metals, this type of velocimeters was used for mercury and Wood's metal [16]. There are modifications of this technique to assess all three components of the instantaneous velocity in a turbulent air flow [37].

Stachowiak *et al.* [38] reported an exotic sensor in which Seebeck's and Peltier's thermoelectric effects are used in combination. This sensor allows one to accurately measure low air-stream velocities in the range from 0.05 to 0.1 m/s at temperatures up to 70 ᵒC.

These types of sensors cannot be used in real melts of aluminium alloys because of temperature limitations.

## Summary of some characteristics of the techniques for measuring fluid velocities

| Technique | T range | Intrusiveness | opaque liquids | Calibration | range, m/s | Comments |
|---|---|---|---|---|---|---|
| Hot wire/film | <100 ºC | □ | Yes | Yes | 0.05–0.1 | Not suitable for Al melts |
| Pitot tube | <100 ºC | + | Yes | Easy | High speeds | Not suitable for high temperatures and recirculating flows. |
| Propeller | Wide range, providing suitable materials | □ | Yes | Easy | Wide range | Difficult choice of materials. Measures instantaneous velocities. Experimental for liquid Al. Possible in water models. |
| Drag probes | Tested up to 350 ºC, possibly also higher temperatures | □ | Yes | Labo-rious | 0.03–0.25 0.1–1.5 only for limited depth. | Requires precise design and machining. Measures averaged velocities. May be suitable for liquid Al. |
| Karman vortex probe | Up to 1600 ºC | □ | Yes | Easy | 0.2–0.7 only sub-surface velocities. | Measures one-directional velocity. Suitable for liquid Al. |
| Particle imaging velocimetry | Not limited | - | No | No | Wide range | surface velocities mesure-ments in liquid Al. In-depth velocities with radioscopy. |
| Laser Doppler velocimetry | Not limited | - | No | Yes | Wide range | Suitable for water models. Not suitable for liquid Al/ |
| Ultrasound Doppler velocimetry | Tested up to 200 ºC | - | Yes | Yes | 0.01–0.75 | May be suitable for liquid Al. |
| Melting probe | Up to 1200 ºC | □ | Yes | Labo-rious | 0.1–0.5 (Average) | Sensitive to temperature,. Can be used for liquid Al. |
| Magnetic probe | Up to 720 ºC | □ | Yes | Labo-rious | 0.005–0.5 2 velocity components | Very weak output signal (expensive voltmeter). Can be used for liquid Al. |

# References

1.      Grandfield, J.F. and P.T. McGlade, *DC Casting of Aluminium: Process Behaviour and Technology.* Materials Forum, 1996. **20**: p. 29-51.

2.      Law, A.M. and W.D. Kelton, *Simulation modeling and analysis.* 1992, New York, NY: McGraw-Hill.

3.      van Haaften, W.M., *Constitutive behaviour and hot tearing during aluminium DC casting*, in *Materiaalkunde.* 2002, Delft University of Technology: Delft. p. 111.

4.      Suyitno, *Hot Tearing and Deformation in Direct-Chill Casting of Aluminium Alloys.* 2005, Delft University of Technology: Delft.

5.      Johnson, R.W., *The Handbook of Fluid Dynamics*, ed. R.W. Johnson. 1998: CRC Press and Springer.

6.      Poirier, D.R. and G.H. Geiger, *Transport Phenomena in Materials Processing.* 1994, Warrendale: TMS.

7.      Flow_Science, *Flow-3D.* 8.1 ed. 2002.

8.      Arnberg, L., L. Backerud, and G. Chai, *Solidification Characteristics of Aluminum Alloys.* Vol. 3. 1996: AFS.

9.      Venneker, B.C.H. and L. Katgerman, *Modelling issues in macrosegregation predictions in direct chill castings.* Journal of Light Metals, 2002. **2**(3): p. 149-159.

10.     Venneker, B.C.H., *A quest for the best discretisation scheme to prevent numerical diffusion and dispersion at high Peclet number flows.* 2001, Netherlands Institute for Metals Research: Delft, report no. p.01.4.023.

11.     van Leer, B., *Towards the Ultimate Conservative Difference Scheme. IV. A New Approach to Numerical Convection.* J. Comput. Phys., 1977. **23**: p. 276.

12.     Ranga Raju, K.G., P.D. Porey, and G.L. Asawa, *Displacement effect in Pitot tube measurements in shear flows.* J. Wind Eng. Industr. Aerodynamics, 1997. **66**: p. 95-105.

13.     Iguchi, M., H. Kawabata, and Z. Morita, *Velocity measurement of molten metal flow at very high temperatures.* High Temp. Mater. Proc., 2000. **19**: p. 187-196.

14.     Tazawa, K., et al., CAMP-ISIJ, 1996. **9**: p. 604.

15.     Svido, A.V., *Tensometric devices to measure the melt velocity.* Elektrotekhn. Promyshl., Ser. Elektrotermiya, Moscow: Informelektro, 1973. **11**: p. 18.

16.     Moore, D.J., *Magnetodynamics of the coreless induction furnace*, in *Trinity College.* 1982, University of Cambridge: Cambridge.

17.     Hsiao, T.-C., T. Lehner, and B. Kjellberg, *Fluid flow in ladles - experimental results.* Scand. J. Metall., 1980. **9**: p. 105-110.

18.    Ek-Kaddah, N. and J. Szekely, *The turbulent recirculating flow field in a coreless induction furnace, a comparison of theoretical predictions with measurements.* J. Fluid Mech., 1983. **133**: p. 1983.

19.    Lillicrap, D.C. *A Technique for Velocity Measurements in Coreless Induction Furnaces.* in *Proc. Metallurgical Applications of Magnetohydrodynamics.* 1982: The Metals Society: p. 46-56.

20.    Iguchi, M., et al., *Development and calibration of a Karman vortex probe for measurement of molten-steel velocities.* Metall. Mater. Trans. B, 1999. **30**: p. 53-59.

21.    Dring, A.L. and B.E. Jones, *Integrated on-line multisensing of fluid flow using a mechanical resonator.* Sensors and Actuators A-Physical, 2000. **85**(1-3): p. 275-279.

22.    Zhilin, V.G., et al. *Diagnostics of liquid metal flows using fibre-optic velocity sensor.* in *Liquid Metal Magnetohydrodynamics.* 1989: p. 373-379.

23.    Eckert, S., W. Witke, and G. Gerbeth, *A new mechanooptical technique to measure local velcocities in opaque fluids.* Flow Measurements and Instrumentation, 2000. **11**: p. 71-78.

24.    Xu, D., et al., *Mathematical and physical modeling of systems for metal delivery in the continuous casting of steel and DC casting of aluminium.* Applied Math. Modell., 1998. **22**: p. 883-893.

25.    Koster, J.N., T. Seidel, and R. Derebail, *A radioscopic technique to study convective fluid dynamics in opaque liquid metals.* J. Fluid Mech., 1997. **343**: p. 29-41.

26.    Guiraud, P., J. Costes, and J. Bertrand, *Local measurements of fluid and particle velocities in a stirred suspension.* Chem. Eng. J., 1997. **68**(2-3): p. 75-86.

27.    Takeda, Y., *Velocity profile measurement by ultrasonic Doppler method.* Exp. Therm. Fluid Sci., 1995. **10**: p. 444-453.

28.    Kikura, H., Y. Takeda, and T. Sawada, *Velocity profile measurements of magnetic fluid flow using ultrasonic Doppler method.* J. Magnetism and Magnetic Mater., 1999. **201**: p. 276-280.

29.    Bouillard, J., et al., *Liquid flow velocity measurements in stirred tanks by ultrasound Doppler velocimetry.* Chem. Eng. Sci., 2001. **56**: p. 747-754.

30.    Kapulla, R., et al., *Local velocity measurements in a thermally-stratified sodium mixing layer using a permanent-magnet probe.* Exp. Thermal Fluid Sci., 2000. **20**(3-4): p. 115-136.

31.    von Weissenfluh, T., *Probes for local velocity and temperature measurement in liquid metal flow.* , Int. J. Heat Mass Trans., 1985. **28**: p. 1563-1570.

32.    Ricou, R. and C. Vives, *Local velocity and mass transfer measurements in molten metals using an incorporated magnet probe.* Int. J. Heat Mass Trans., 1982. **25**: p. 1579-1588.

33.    Argyropoulos, S.A. *Measurement of velocity in high temperature metals and slags, Proc. Conf. Fundamentals of Metall. Processing.* in *The James M. Toguri Symp. at the 39th Annual Conf. of Metallurgists of CIM.* 2000. Ottawa, Ontario, Canada.

34.    Argyropoulos, S.A., A.C. Mikrovas, and D.A. Doutre, *Dimensionless correlations for forced convection in liquid metals: Part I. Single-phase flow.* Metall. Mater. Trans. B, 2001. **32**: p. 239-246.

35.    Argyropoulos, S.A., A.C. Mikrovas, and D.A. Doutre, *Dimensionless Correlations for forced convection in liquid metals: Part II. Two-phase flow.* Metall. Mater. Trans. B, 2001. **32**: p. 247-252.

36.    Argyropoulos, S.A., A.C. Mikrovas, and D.A. Doutre, *Velocity measurement in high temperature liquid metals using calibration results from the annular channel.* Canad. Metallurgical Quarterly, 1996. **35**: p. 85-91.

37.    Rajagopalan, T., T. Zhou, and R.A. Antonia, *Three-component turbulence measurements using a four-wire probe.* Flow Measurements and Instrumentation, 1998. **9**: p. 211-216.

38.    Stachowiak, H., et al., *A thermoelectric sensor for fluid flow measurement. Principles, calibration and solution for self temperature compensation.* Flow Measurements and Instrumentation, 1998. **9**: p. 135-141.

# Chapter 3

## Determination of thermal boundary conditions[1]

In this chapter the thermal boundary conditions that are necessary for a computer calculation of the temperature profile during DC Casting are determined. Two different cooling zones exist in DC Casting. The primary cooling is the part of the cooling that takes place in the mould cavity. Below the mould the cooling takes place by a water-jet that is directed onto the just formed shell of solidified aluminium. The amount of heat extracted during primary cooling is much lower than during secondary cooling. The heat flux is a function of the process conditions and the surface temperature of the solidified shell. Several boiling modes and convective phenomena determine the magnitude of the cooling. The complex heat transfer phenomena occurring during secondary cooling require a subdivision of this region in two sub-regions. One of them is the impingement region, where the cooling water hits the surface of the just solidified shell. The other one is the region where water flows down the hot-shell. Here the cooling is a mixture of forced convection and boiling. Because it is very difficult to quantify and to calculate the heat transfer for the different cooling mechanisms, measurements of the cooling of a hot metal are necessary to find the right quantitative relations. In the next paragraphs a description of a technique to determine the thermal boundary conditions in secondary cooling using a specially designed rig is given. The application in a simple DC Casting model is compared to a constant heat transfer coefficient in the different regions of cooling. The primary cooling is described at the end of this chapter.

---

[1] Part of this chapter have been published in:

Zuidema, J., Jr., I.J. Opstelten, and L. Katgerman, Boiling Curve Approach for Thermal Boundary Conditions in DC Casting, in Continuous Casting, K. Ehrke and W. Schneider, Editors. 2000, DGM/WIley-VCH, Weinheim, Germany. p. 138-142.

Zuidema, J., Jr., et al., Secondary cooling in DC casting: modeling and experimental results, in Light Metals 2001 (USA). 2001, Minerals, Metals and Materials Society/AIME. p. 873-878.

## 3.1  Description and analysis of secondary cooling

To simulate process conditions in the secondary cooling stage of DC Casting an apparatus (fig 3.1) was designed at Corus RD&T[1]. The block is electrically heated to a uniform temperature varying from 300 °C to 500 °C. Except for the measuring surface (the cooled surface) all sides of the block are thermally insulated. A water-jet is traversed along the slab from bottom to top and the thermal behaviour at a fixed vertical position is measured at different depths (3,8,13 and 18 mm) close to the surface. The ascending speed is varied, as well as the initial temperature and the water flow rate. The heat flux as a function of distance is obtained by inverse modelling of the thermal histories [2]. The inverse modelling was performed with CalcoMOS . The heat flux versus surface temperature data is obtained. With the help of boiling theory [3] a formulation was found that describes the thermal behaviour as a function of the distance along the slab. This relation was generalized by including the effect of water flow rate and ascending speed [4]. Not included in this approach was the description of air conduction and interaction of air conduction regions with the water-jet.

The formulation was extended further with a constant heat transfer coefficient from the surface of the slab to air and from air to the water-jet. The formulation was used in the Flow-3D commercial CFD code and validated against experiments.

## 3.2  Theory and thermo-physical data

### Formulation[1]

The heat flux equations found for the impingement region are given by

$$\frac{q}{A} = \alpha\, T - \beta \tag{3.1}$$

with $\alpha$ and $\beta$ listed in Table 3.1. T is the surface temperature of the block in °C. The heat flux for the down streaming water film is formulated by

$$\frac{q}{A} = \left(-1.67 \cdot 10^5 + c \cdot \overline{T}\right) Q_{water}^{\frac{1}{3}} \Delta T + 100 \left(\Delta T_x\right)^3 , \tag{3.2}$$

where

$$c = -4.01 \cdot 10^6 \cdot Q_{water}^{\;2} + 6.90 * 10^4 \cdot Q_{water} + 628 . \tag{3.3}$$

Here $Q_{water}$ is the water flow rate per unit width in m³/(m s), $\overline{T}$ is the average of the bulk fluid temperature and the surface temperature in K, $\Delta T$ is the temperature difference between the bulk fluid and the surface temperature in K and $\Delta T_x$ is the temperature difference between the surface temperature and the saturation temperature of the cooling water in K.

---

[1] In Fig. 3.2 on page 52 a schematic view of the different cooling regions is given.

TABLE 3.1. Parameters for equation 3.1.

| T [ºC] | $\alpha \left[10^4 \frac{m^2}{W\,°C}\right]$ | $\beta$ [$10^6$ ºC] |
|---|---|---|
| T < 120 | 2.73 | -1.27 |
| 120 ≤ T < 150 | 9.43 | -9.24 |
| T ≥ 150 | 1.23 | 3.06 |

Eq. 3.2 is based on a formulation derived by [5]. Eq. 3.3 is believed to be dependent on the speed of the water-jet, but this has not been verified yet.
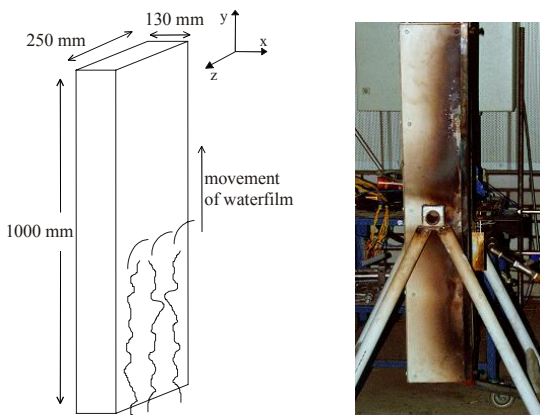


Fig. 3.1. Sketch and photograph of experimental set-up

For the heat transfer coefficient in the air region above the water-jet a fixed heat transfer coefficient of 50 W/m²K was used. The old-time values of the water temperature and the slab's surface temperature are used for calculating the heat transfer coefficient from equations 3.1 to 3.3.

**Thermo-physical properties**

In Table 3.3 the thermo-physical properties for AA1050 used in the computer simulations are given. In Table 3.2 the properties for the water-jet and air that were used are given. The down streaming region, the water impingement region and the air region are defined as conduction-only parts of the calculation.

TABLE 3.2. Thermo physical properties for air and water. (h with respect to the surface of the slab)

| | $\lambda$ (W/m K) | $\rho C_p$ (J/m³K) | h (W/m²K) |
|---|---|---|---|
| Air | 25e-3 | 1293 | 50 |
| Water | 2.0e3 | 2.7e6 | Eq 3.1 or 3.2 & 3.3 |

*TABLE 3.3. Properties of AA1050 (Fe 0.37 wt%, Si 0.05 wt%)*

| Temperature [ºC] | Conductivity [W/mK] | Specific Heat, $C_p$ [J/kgK] | Specific energy [J/kg] |
|---|---|---|---|
| - | 208 | 8.89E+02 | 2.43E+05 |
| 100 | 206 | 9.30E+02 | 3.34E+05 |
| 300 | 201 | 1.02E+03 | 5.29E+05 |
| 500 | 194 | 1.13E+03 | 7.43E+05 |
| 634.4 | 190 | 1.22E+03 | 9.01E+05 |
| 658.5 | 102 | 1.18E+03 | 1.33E+06 |
| 700 | 102 | 1.18E+03 | 1.38E+06 |

The thermal conductivity of water was chosen very high because the heat extraction is limited by the interfacial heat transfer coefficient and should not be limited by heat conduction instead. The heat transfer coefficient from water to air is chosen 150 W/m² K. This value describes the heat extraction in the air region better. The contact length between the air and water-jet region is 5 mm.

## 3.3  Description of Calculation

The software used for calculating the secondary cooling behaviour of DC Casting is Flow-3D. This is a finite volume based solver for thermal and fluid flow problems. It is Cartesian based and has an algorithm for dealing with boundaries that are not aligned with the grid [6]. In the calculations presented in this paper however, the grid was aligned with the boundaries, so this feature was not necessary for this work. It is of interest though for circular water-jets in three dimensional calculations. The energy equations are solved in an explicit scheme. The calculations are considered finished when the temperatures at locations of interest do not change anymore with time.

The geometry used for modelling is a 2-dimensional x-y section of the slab (fig 3.2). The y-coordinate is in vertical direction. The size of the impingement region is taken as 8 mm unless specified differently. The slab is moving with respect to the location of the impingement region of the water-jet with a speed v, which is equivalent to the water-jet moving up with this speed (in the experiment).

The non-uniform mesh is 46 cells in the x-direction and 225 cells in the y-direction. The smallest cell is 0.5 mm in the x-direction and 1 mm in the y-direction. This is in the impingement region. The cells increase from this region to a maximum cell size of 19.5 mm (in x) by 73.0 mm (in y) in the upper right corner of the geometry. More information on the mesh can be read from Table 3.4.

*TABLE 3.4. Description of the finite volume mesh used for the calculations.*

| x [mm] | no. of cells | y [mm] | no. of cells |
|---|---|---|---|
| x ≤ 13 | 26 | y ≤ 700 | 30 |
| 13 < x ≤ 23 | 10 | 700 < y ≤ 1000 | 40 |
| 23 < x ≤ 135 | 10 | 1000 < y ≤ 1100 | 100 |
| | | 1100 < y ≤ 1130 | 15 |
| | | 1130 < y ≤ 1200 | 20 |
| | | 1200 < y ≤ 2000 | 10 |

The calculation starts with a constant initial temperature of the slab and proceeds until steady state is reached. This is approximately after 200 seconds for the case of a descending speed of 6.64 mm/s and a water amount of 240 l/m/min and an initial slab temperature of 400 °C.

## 3.4  Results and Discussion

The figures in this section are all shown from a low x-location of 1.05 m to a high x-location of 1.12 m, where the impinging water-jet hits the surface around 1.1 m. The effects from air cooling far away from the water-jet and from the water convection-only cooling are not of particular interest here and therefore omitted.

To find the correct properties for modelling the air conduction region a trial and error approach was used. The heat transfer coefficient between water-jet and the air region was changed as well as the size and position of the water-jet. The results, with process conditions  Q=240 l/m/min, v=6.64 mm/s and $T_i$=400 °C, showing the difference in temperatures from the measurements and the Flow-3D calculations are shown in Fig. 3.3. The temperatures were recorded at 3 mm from the surface of the slab. In Fig. 3.4 the temperature profile of a part of the slab around impingement corresponding to this calculation is plotted. The maximum deviation between measured and calculated data is at the top and bottom of the impingement region. This is a reasonable place for the maximum deviation, because the heat flux change is not necessarily continuous from one region to another. If  only heat transfer from convection and nucleate boiling is chosen and not the impingement relations as given by Eq. 3.1 then the temperature profile is not predicted correctly (thick line in Fig. 3.3). The mean deviation calculated by

$$\overline{\Delta T} = \frac{1}{N}\sum_{i}^{N}\left|T_i - \overline{T}\right| \tag{3.4}$$

in the y-range from 1.05 m to 1.12 m is 0.88 °C for the case shown in Fig. 3. The difference is between -1.36 °C and 3.28 °C.
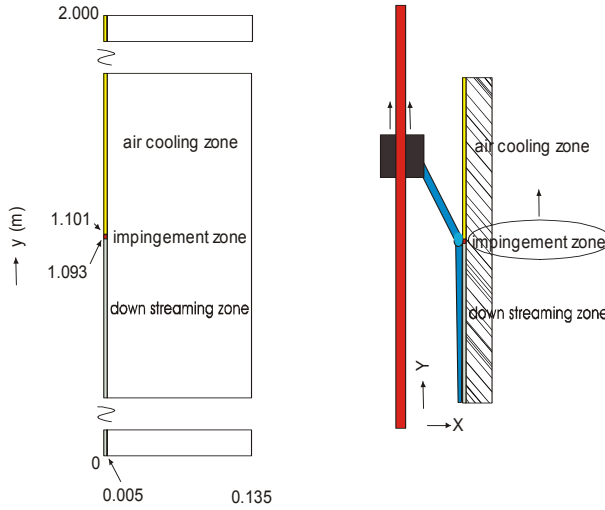
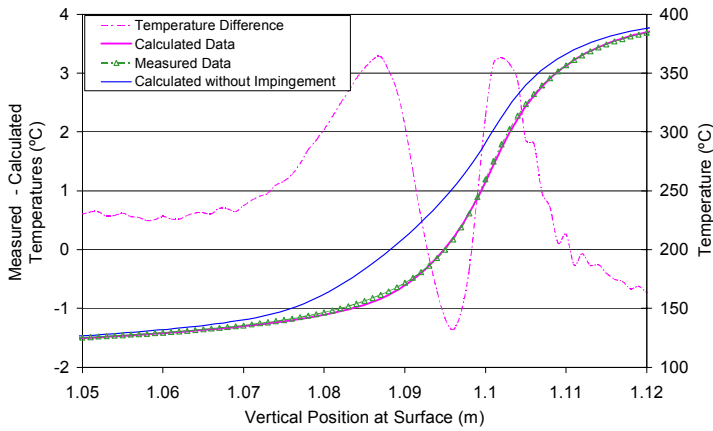Fig. 3.2. Description of geometry used for calculation.



Fig 3.3. Temperatures and temperature differences from experiment and calculation around impingement point. The measurements were taken 3 mm from the surface. This corresponds to cross-section A-A' in Fig. 3.4

To verify the validity of the method 9 more experiments under different processing conditions were compared to calculations. Table 3.5 shows the results. All calculated temperature curves follow the experimental curve qualitatively good. The results are largely improved compared to our previous reported results [4]. This is because the thermal conductivity of water was chosen very high as explained in the *thermo-physical properties* paragraph. The heat transfer coefficient from water to air was chosen 150 W/m² K. This approach described the heat extraction in the air region better and gave better overall results.

TABLE 3.5 Comparison of experiments $T_{exp}$-$T_{calc}$. The min column is the biggest negative difference and the column max is the biggest positive difference between $T_{exp}$ and $T_{calc}$

| process conditions | | | $\overline{\Delta T}$ | min | max |
|---|---|---|---|---|---|
| Q | V | $T_i$ [°C] | [°C] | [°C] | [°C] |
| [l/m/min] | [mm/s] | | | | |
| 240 | 6.64 | 400 | 0.88 | -1.36 | 3.28 |
| 240 | 3.32 | 400 | 6.08 | -4.88 | 23.44 |
| 240 | 1.66 | 400 | 5.88 | -6.53 | 12.89 |
| 240 | 6.64 | 500 | 4.83 | -9.19 | 8.52 |
| 240 | 6.64 | 300 | 2.88 | -0.03 | 19.97 |
| 500 | 6.64 | 400 | 2.86 | 0.62 | 16.30 |
| 500 | 6.64 | 500 | 2.25 | -9.59 | 9.49 |
| 500 | 3.32 | 500 | 1.93 | -4.24 | 9.17 |
| 120 | 1.66 | 400 | 10.13 | -8.66 | 18.29 |
| 120 | 3.32 | 400 | 7.45 | -3.08 | 33.41 |
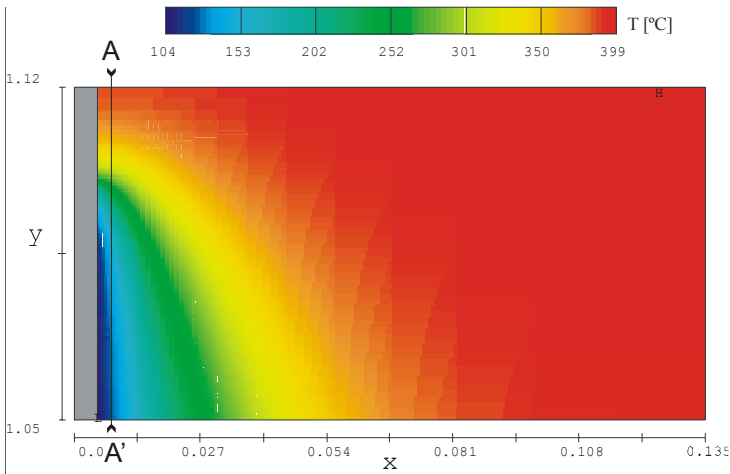


Fig 3.4. Temperature profile with cross-section AA' for which temperatures are given in Fig. 3.3.

## Sensitivity and uncertainties

The sensitivity of the location of the impingement point and its extent are shown schematically in Table 3.6 for the case with one of the greatest average differences in temperatures (second case from Table 3.5).

TABLE 3.6 Influence on position and size

| | $\frac{1}{n}\sum|T-\bar{T}|$ | min | max |
|---|---|---|---|
| original | 6.08 | -4.88 | 23.44 |
| shifted, resized | 1.56 | 2.39 | 12.76 |

The size of the impingement region was decreased from 8 mm to 6 mm and the bottom of the jet was kept at the same location. The mean absolute difference and the maximum deviations are within close range of the experiment considering the sensitivity of the measured temperatures to the x and y-location. If for example the temperature is measured at 3.5 mm instead of 3 mm from the surface, the temperature is 6 °C lower in the impingement region. This error can not easily been checked by moving the entire temperature curve up, because the curve also flattens out. If the thermocouple position is moved in the y-direction, the effect on the temperature curve is less pronounced.

Due to the nature of the water-jet, which impinges not exactly at one location on the surface, but can move up and down a bit, the total amount of heat extracted in the impingement region can differ from experiment to experiment. This irregular motion of contact zone of the water-jet is caused by the boiling behaviour at the surface of the aluminium. If the total amount of heat subtracted in the impingement region is too low, the temperature difference between the measured and calculated temperature curves will change to a higher value moving from above impingement to below as can be seen in Fig. 3.5. The maximum difference between the measured and the calculated temperatures in this figure is below the impingement region in the region of nucleate boiling and convection. This indicates that the maximum heat flux in this region is too high in the calculation. The temperatures discussed are all measured at 3 mm from the surface. The real surface temperatures that can be calculated have bigger uncertainties than the temperatures at 3 mm from the surface. The results from this research should be used within this context when calculating the surface temperature.

In Fig. 3.6  the surface temperatures of the case displayed in Fig. 3.5 are shown for the original and shifted and resized case. It can be seen from this figure that the maximum temperature difference between the original and resized and shifted case is 140 °C. This is at y=1.100 m, which is the location where the heat transfer has its maximum. Thus close to the water-jet the surface temperatures are not reliable. At 1 cm above the maximum temperature difference the temperature difference is 3.5 °C. At 2 mm below the maximum temperature difference the temperature difference has decreased to 2.5 °C.  Only in the water-jet the difference in the surface temperatures is big. At 3mm from the surface the difference between the original and shifted, resized calculation is also given in Fig. 3.6. The difference is more spread out here in y-direction and its peak is lower. The temperature difference is here decreased to 3.5 °C at 8 mm left of the maximum in temperature difference. These results indicate that good temperature results, which are not extremely sensitive to the exact location of the impingement region, can be obtained from approximately 1cm up and down the upper-impingement point.

When the temperature curves for all experiments summarized in Table 3.5 were examined, it was found that the temperature difference between the measured and the calculated temperature curves increases with decreasing height in the nucleate boiling and convection region for low traversing speeds. An

example, the case with Q=240 l/m/min and T=400 ºC and v=1.66 mm/s is shown in Fig. 3.7.

## 3.5  Application in DC Casting simulation

### Comparison between secondary cooling model and the use of constant heat transfer coefficients

To show how the secondary cooling model compares to the case where constant heat transfer coefficients are chosen for the different cooling regions, a simple 2D axis-symmetrical calculation was performed on a DC Casting of a 20 cm diameter billet (Fig. 3.8). The material was AA 1050 with properties as described in Table 3.3. The secondary cooling model (SCM) is compared to two cases with constant heat transfer coefficients (HTCx). The boundary conditions are given in Table 3.7. The temperature of the cooling medium is 318 K except for the mould section which is chosen to be 523 K.

*TABLE 3.7 Heat transfer coefficients for calculations. The heat transfer coefficient to air is taken very high. This value is not important, because a thin air layer was also modelled and this layer had a very low thermal conductivity.*

| case\region | hot-top | mould | air | impingement | downstreaming |
|---|---|---|---|---|---|
| SCM | 1 | 5000 | 2500 | Eq 3.1 | Eq. 3.2 & 3.3 |
| HTC1 | 1 | 5000 | 2500 | $4.80*10^4$ | $3.00*10^4$ |
| HTC2 | 1 | 5000 | 2500 | $4.80*10^4$ | $4.00*10^4$ |

In Fig. 3.10 the temperature close to the mould surface is given as a function of the z coordinate. The temperature difference between the secondary cooling model (SCM) and the two different constant heat transfer coefficients (HTCx) is also given in the same graph. Due to the strong dependence of the surface temperature on the heat transfer coefficient in the SCM, the HTCx models will start to deviate from the SCM in the impingement and downstreaming region. This has an effect of the heat flux from the billet surface to the water. The cumulative heat flux difference between the HTCx and SCM is given in Fig. 3.11. The heat flux difference is added up from the hot-top down to the downstreaming region. The results must be interpreted based on the definition that a positive heat flux is a heat flux going in to the domain. With this in mind it can be seen that HTC1 removes less heat than SCM and HTC2 removes more heat than SCM. It could easily be concluded, that because of this, the solidus and liquidus position of SCM must lie somewhere between the results from HTC1 and HTC2. In Fig. 3.12 it can be seen that this is not the case, because the heat transferred before solidification is bigger in the HTC calculations.
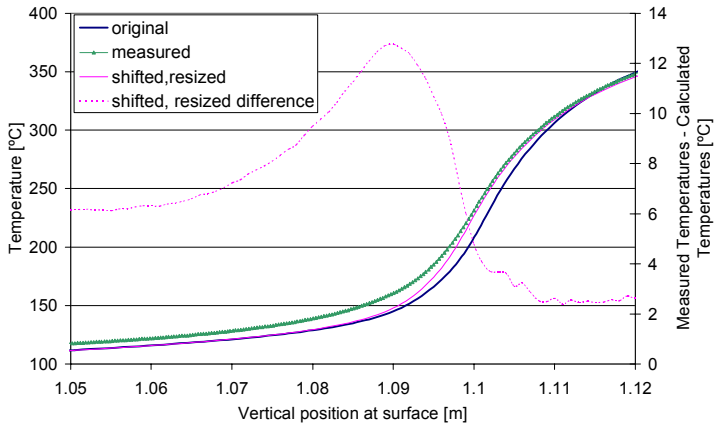
*Fig 3.5. The influence of shifting and resizing the impingement zone on the temperature profile.*
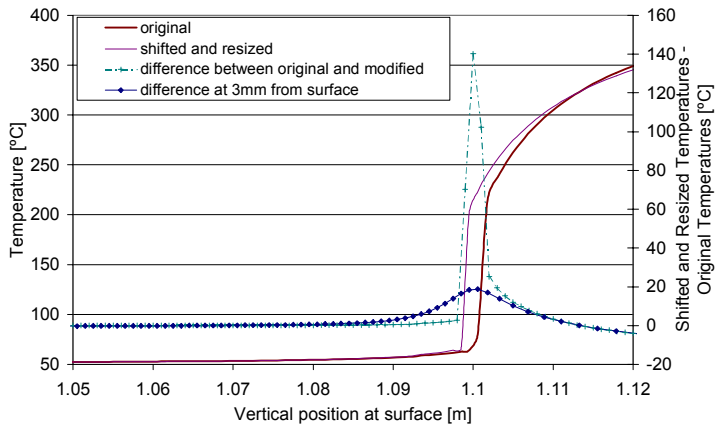


*Fig 3.6. Surface temperatures from the case displayed in  Fig. 3.5 and difference between them.*
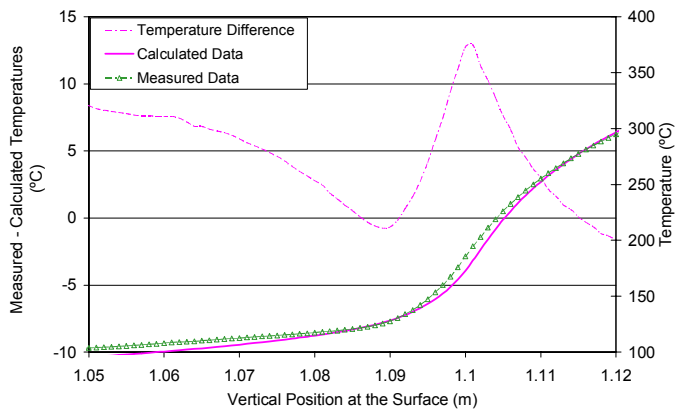


*Fig 3.7. Temperature difference as a function of y-coordinate in the convection and nucleate boiling regime indicating the heat flux below impingement is too high in the calculation.*
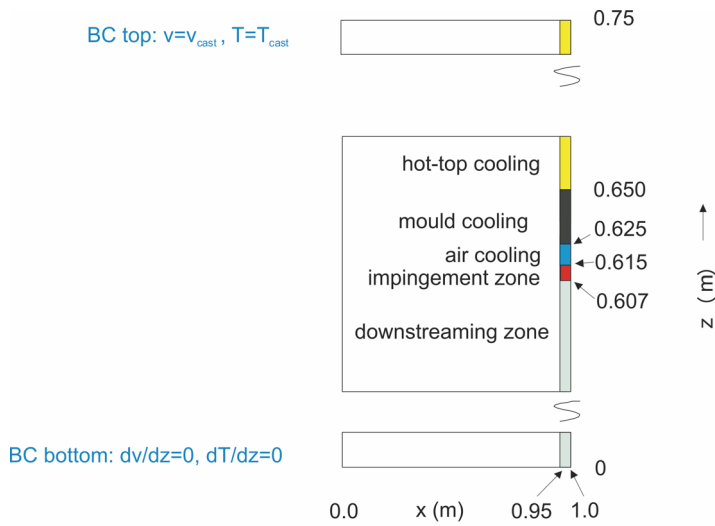
Fig 3.8. Description of cooling zones in calculation and in- and outflow boundary conditions.
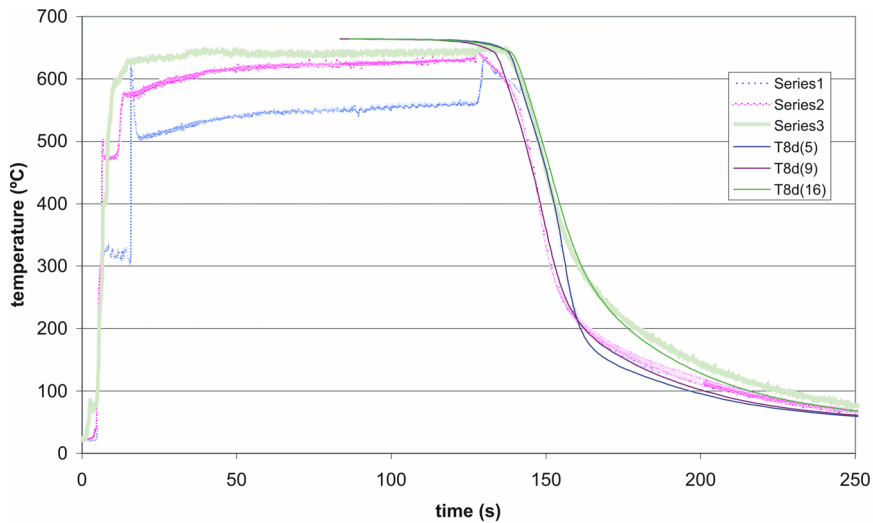


Fig 3.9. Measured data of temperature vs. time for different thermocouple positions compared with calculated temperatures using the SCM. Series 1,2 and 3 correspond to T8d(5), T8d(9) en T8d(16) respectively. The numbers in brackets represents the distance of the thermocouple from the surface in mm.
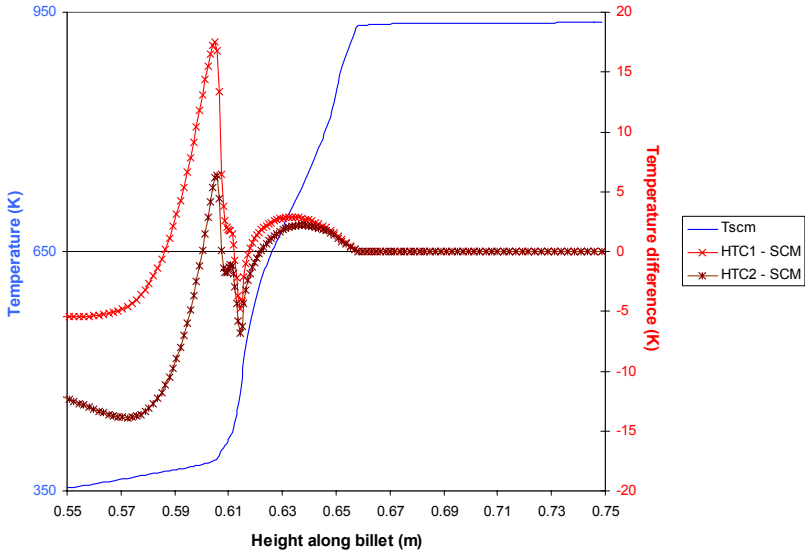
Fig 3.10.Temperatures at 2.5 mm from the billet surface for the secondary cooling model (SCM) and temperature difference between SCM and 2 cases with constant heat transfer coefficients (HTCx).
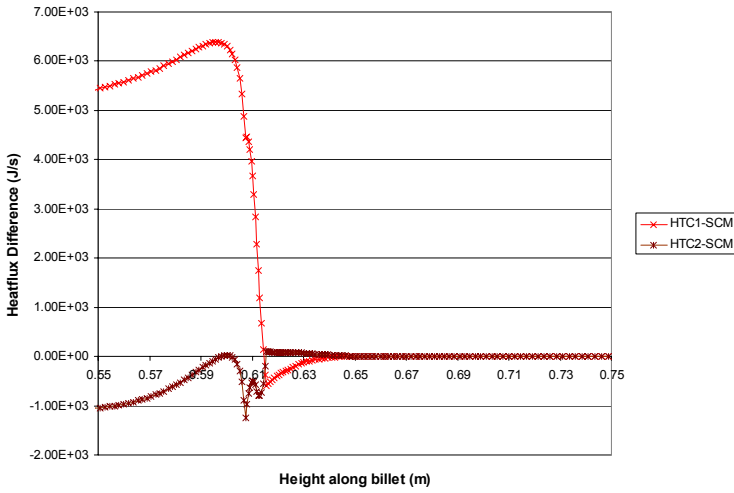


Fig 3.11.Heat flux difference between HTCx and SCM at 2.5 mm from the billet surface.
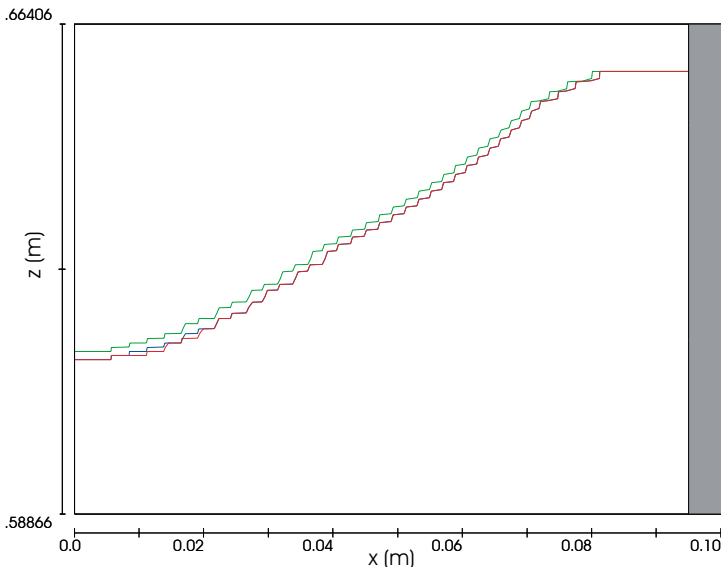
*Fig 3.12. Position of the solidus temperature for HTCx and SCM. HTC2 is the lowest line and SCM is the upper solidus line.*

## Comparison of SCM with DC Casting experiment results obtained in experimental DC Casting facility

In the previous paragraph it was shown that differences between the constant heat transfer coefficient and the secondary cooling model, although not big, exists. The effect on the temperatures close to the surface is bigger than the effect on the location and shape of the solidus, because of the integrating effect of total cooling further away from the chilled surface.

In this paragraph the SCM is compared to measured temperatures close to the surface during a experiment performed on a Al 4.5 wt% Cu alloy. The process parameters for the experiment are shown in Table 3.8. The position of the thermocouples used to measure the temperatures during the cooling down of the billet is shown in Fig. 3.13.
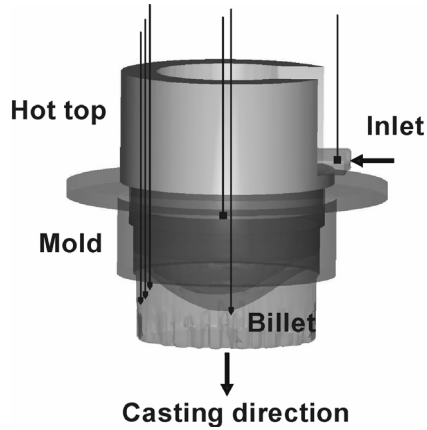
*Fig 3.13. Thermocouple set-up for measuring temperatures close to the chilled surface. On the left side of the figure, three thermocouples are shown, that were frozen in during solidification and moved downward with the casting velocity. Their positions were at 3, 9 and 16 mm from the surface.*

*TABLE 3.8  Process parameters for the DC Casting experiment*

| Process parameters (average) | Value |
|---|---|
| furnace temperature | 750 ℃ |
| launder temperature (close to mould) | 720 ℃ |
| casting speed | 2 mm/s |
| water cooling rate | 140 l/min |
| water temperature | 22 ℃ |

The thermo-physical data for the calculation are given in Table 3.9. The casting velocity was 2 mm/s. The inlet temperature was 664 ℃ . The calculation set-up was the same as that described in Fig. 3.8.

Table 3.9. Thermo-physical properties of Al−4.5wt% Cu[4]

| Property | Symbol | Units | Value |
|---|---|---|---|
| Liquid density | $\rho_l$ | kg/m³ | 2460 |
| Solid density | $\rho_s$ | kg/m³ | 2750 |
| Liquid specific heat | $C_{p,l}$ | J/kg K | 1054 |
| Solid specific heat | $C_{p,s}$ | J/kg K | 958 |
| Latent heat of fusion | L | kJ/kg | 390 |
| Liquid thermal conductivity | $k_l$ | W/m K | 95.0 |
| Solid thermal conductivity | $k_s$ | W/m K | 180 |
| Liquid diffusion coefficient | $D_l$ | m²/s | $5.0 \times 10^{-9}$ |
| Liquid viscosity | $\mu_l$ | Pa·s | 0.0013 |
| Liquid thermal expansion coefficient | $\beta_{T,l}$ | K⁻¹ | $1.17 \times 10^{-4}$ |
| Solid thermal expansion coefficient | $\beta_{T,s}$ | K⁻¹ | $2.25 \times 10^{-5}$ |
| Liquid solutal expansion coefficient | $\beta_{s,l}$ | | -0.73 |
| Solid solutal expansion coefficient | $\beta_{S,s}$ | | -0.87 |
| Melting point of aluminium | $T_{melt}$ | K | 933.5 |
| Eutectic temperature | $T_e$ | K | 821.2 |
| Maximum solid solubility | $f_{max}^{Cu}$ | | 0.0565 |
| Eutectic composition (by weight) | $f_e^{Cu}$ | | 0.33 |
| Equilibrium partition coefficient | $k_p$ | | 0.171 |

The results for temperatures at some positions close to the surface of the billet are given in Fig. 3.9. The calculated and measured temperatures are close to each other, but start to deviate at lower temperatures. The calculated temperature is decreasing faster than the measured temperature. This effect is more pronounced for the positions closer to the surface than for the positions more inwards into the billet. This suggests that the heat transfer rate is overestimated in the model at lower surface temperatures with respect to the experiment. This can be explained by the heating up of the downwards streaming water in the experiment, while in the model, this water has a fixed temperature. The most important is however that the model quite accurately predicts the cooling rate in the region were the material starts to solidify. Instead of aluminium alloy AA 1050, here a aluminium alloy with 4.5% copper was used. The model, which is based on physical relations, proves itself to be independent of the type of aluminium alloy in this particular case.

**The entrance effect**

In Fig. 3.14 the response from thermocouple 1 (the thermocouple at 3 mm from the surface) versus two simulations of the start-up is given. Inflow conditions for Case I were taken from video recordings of the casting experiment. The initial filling took place in the form of a small jet flowing in to the mould cavity. The size of this jet was estimated from the video recording as 10 mm wide and 7 mm high. For Case I we assumed that this inlet conditions remained valid even when the melt level in the launder of 35 mm was reached. For the calculation an obstacle was placed in the inlet with an opening of 10 mm wide × 7 mm high. Because the hot-top was already filled with liquid aluminium, the velocity as recorded from the experiment was not chosen as boundary condition. Instead a pressure boundary condition, with metallostatic distribution was chosen as inlet. The simulated casting time was 100 seconds. After 5 seconds the bottom-block was ramped up to a casting speed of 2 mm/s. This ramping up took place in 30 seconds. The inflow boundary condition for case II was also a pressure boundary condition with metallostatic correction. Instead of a confined jet entering the computational domain, now the inflow took place over the complete inlet of 11.5 cm wide and 3.5 cm high. This resulted in much slower speeds at the entrance.
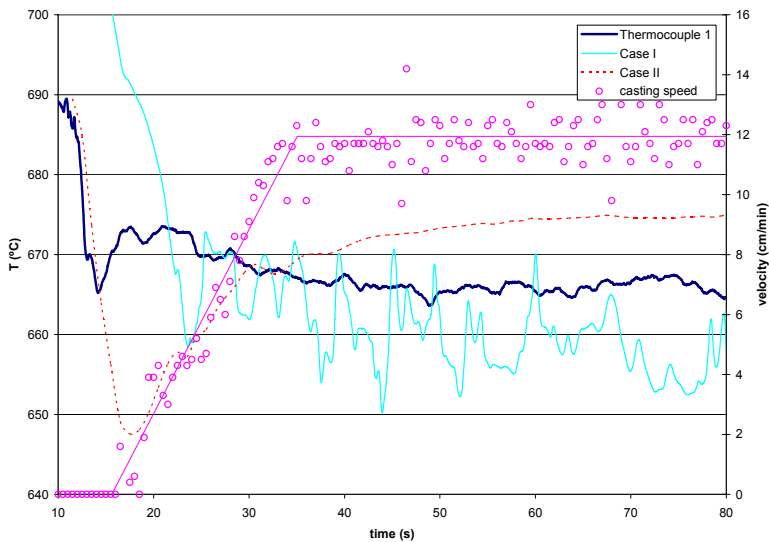


*Fig 3.14. Temperature of thermocouple 1. Experiment versus calculations Case I and II. On the right vertical axis the casting velocity is given.*

## 3.6  Conclusions

A modified approach to describe heat flow during DC Casting with the following features was chosen:

- treats the air conduction as a region with a constant heat transfer coefficient

- calculates the heat transfer from the air region towards the water-jet and thus eliminating the use of an advance cooling region

- is more fundamental in the way it assesses the interaction between the different heat transfer regions

The calculated results deviate for some cases slightly more from the experiments than the ones obtained with the previous approach [4] on a heated slab of AA1050. Further research is necessary to improve the model in such a way that all cases are in close agreement with the experiments.

Improvements to give the calculations more physical background are:

- include the effect of the traversing speed in the convection and nucleate boiling region

- include the effect of the water velocity in the heat transfer equations

If the uncertainty in temperature is lower then 4 °C, then reliable temperature results are obtained around 1 cm up and down the upper impingement point.

The cooling behaviour of the surface of direct chilled castings can be described by this formulation as has been shown for a real casting.

## References

1.    Opstelten, I.J. and J.M. Rabenberg, *Determination of the experimental boundary conditions during aluminum DC Casting from experimental data using inverse modeling.* Light Metals, 1999: ed. C.E. Eckert (TMS Publ., Warrendale, PA) pp. 449-457.

2.    Opstelten, I.J., *Report on database of heat transfer between cast metal and cooling water.* 1998, Corus RD&T.

3.    Granfield, J.F., A. Hoadley, and S. Instone, *Water cooling in direct chill casting: Part 1, boiling theory and control.* Light Metals, 1997: ed. R. Huglen (TMS Publ., Warrendale, PA), pp. 691-699.

4.    Zuidema, J., Jr., I.J. Opstelten, and L. Katgerman, *Boiling Curve Approach for Thermal Boundary Conditions in DC Casting.* Continuous Casting, eds. K. Ehrke, W. Schneider, DGM/Wiley-VCH, Weinheim, Germany ISBN 3-527-30283-2 (2000) pp. 138-142.

5.    Weckman, D.C. and P. Niessen, *A Numerical Simulation of the D.C. Continuous Casting Process Including Nucleate Boiling Heat Transfer.* Metall. Trans B, 1982. **13**(4): pp. 593-602.

6.    Flow-3D, *Flow-3D version 8.1.* 2002.

# Chapter 4

## Velocity measurements with a magnetic velocity probe

This Chapter deals with one experimental technique to measure velocities in liquids. A comparison of the different techniques was given in chapter 2, with their main advantages and disadvantages. Some measurement techniques are not suited for non-translucent media, but are nevertheless useful for measuring in water models of the real processes. Measured velocity profiles in DC Casting experiments have been recorded in the past[1]. These profiles were recorded with an induction velocity probe[1-4]. At that time, the 1980's amplifiers were not suited to measure in the range of nanovolts. Therefore the resolution required to validate DC Casting experiments could not been obtained. The velocity measured in a Perspex water model of a cyclone[5,6] will not be given in this chapter. More information on the experiments with this cyclone is given in chapter 6.

### 4.1 Introduction

The demand for quality of aluminium products is constantly increasing. To fulfil this demand research is carried out into fundamental aspects of the process. Computer modelling of mould filling and solidification is part of this research. For a complete validation of  DC Casting process models, there is usually lack of experimental data. Temperatures can easily be measured, but the measurement of velocities in liquid metals is very difficult.

A schematic view of the velocity profile during DC Casting is given in Fig. 4.1. Velocities of different magnitudes are present in the process. In the launder the aluminium is completely in the liquid state and moves with a constant, relatively high, velocity towards the mould. In the mould entrance a turbulent flow pattern may exist which disappears below the aluminium surface. In the region where the solidification takes place the velocity is of the order of some cm/s. In this region it is important to know both the direction as well as the magnitude of the velocity of the liquid aluminium close to the solidification front. The liquid velocity

determines the possible break-up of dendrites into the melt and the shape of the solidification front. The size of the mushy zone can also be affected by the direction of the moving liquid.
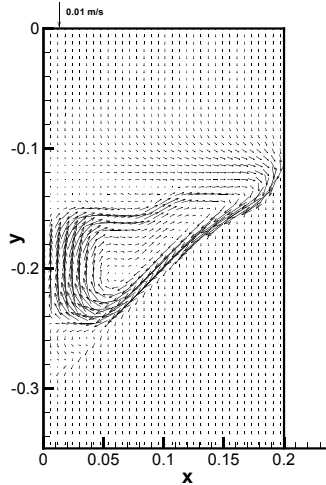


*Fig. 4.1. Calculated velocity in the liquid sump of DC Casting reproduced from Venneker [7].*

In Fig. 4.1 the computed velocity vector field from a 2 dimensional DC Casting calculation is given. The velocities calculated are not verified by experiments. Indirect measurement of macro segregation profiles after solidification can be compared to experiments and calculations in steady state cases. In the initial transient state of the DC Casting process indirect validation of numerical models is almost impossible and that is why velocity measurements are needed as a validation tool in the development of new process models.

In other fields of science and engineering numerous techniques exist for measuring velocities. In chapter 2 the different methods to measure the velocity in liquid metals are reviewed. Techniques based on mechanical response, tracing of particles and on magnetic induction are covered in this review.

## 4.2 Experiments using the magnetic velocity probe

Based on characteristics of the different methods to measure velocities (chapter 2), it was decided to build a magnetic velocity probe[4] for measurements of velocities in molten aluminium.

### Description of probe

The velocity probe that was used in the experiments is shown in Fig. 4.2. It is based on the probe of Kapulla et al. [4], but the magnetic field is perpendicular to the axis of the probe. This was done to be able to measure the horizontal velocity components in a rotating bath.
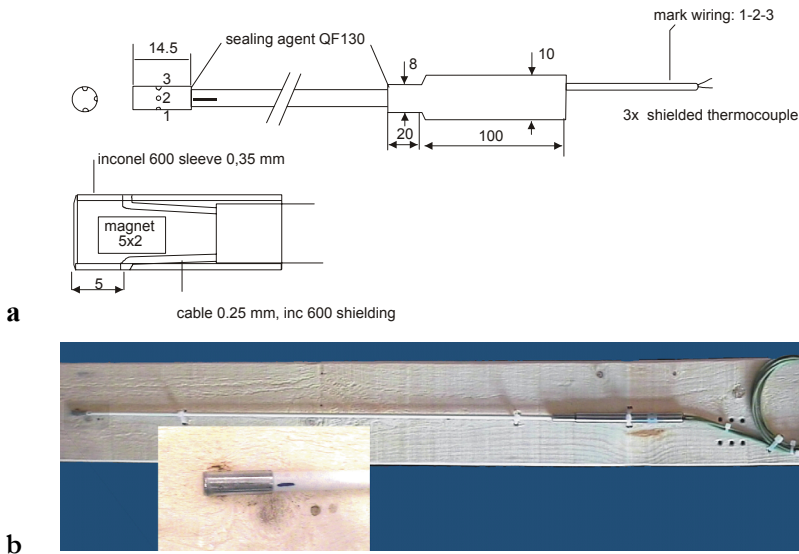
Fig. 4.2. Schematic view of velocity probe based on Kapulla et al. [46] (**a**) and photos of prototype (**b**)

The probe was constructed Thermo Electra[3], using standard K-type thermocouples, which were spot-welded to the inside of a small stainless steel cup. The wiring from the cup was shielded by an alumina tube. The inside of the cup was also filled with alumina (QF 130) to prevent short circuiting of the six wires. Before the probe was used, all electrical connections were tested.

## Set-up of experiments and calibration

Firstly the velocity probe was tested in saturated salt water in a Perspex water model. The test setup is shown in Fig. 4.3. Using a pump, different water flow rates were realised. The aim of the test was to show qualitatively the working of the probe. It appeared that the probe's signal/noise ratio was low, making it hard to separate this effect from the moving water effect.

---
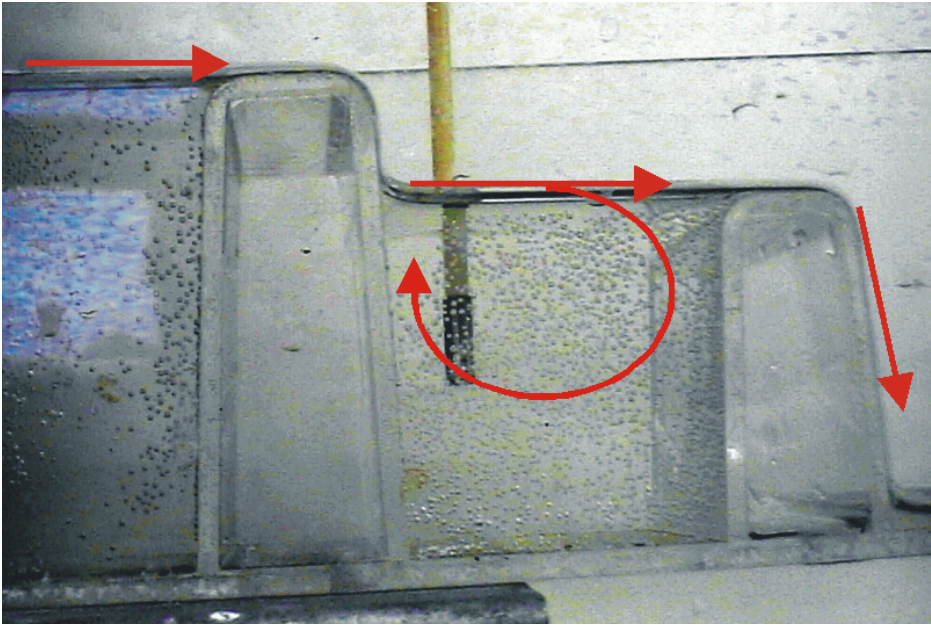
*Fig. 4.3. Test set-up for testing the velocity probe in salt water. The red arrows indicate the flow pattern observed visually.*

The limitations of the water testing facility made validation of the probe impossible. Testing of the probe was therefore moved to a liquid Sn bath instead of the water rig. Liquid metals have conductivities that are 6 to 7 orders of magnitude higher than salt water. The setup used for these experiments is shown in Fig. 4.4. A limitation of the setup was that only one signal could be measured by the nano-volt meter. The switching between the signals was done manually by a switchbox.
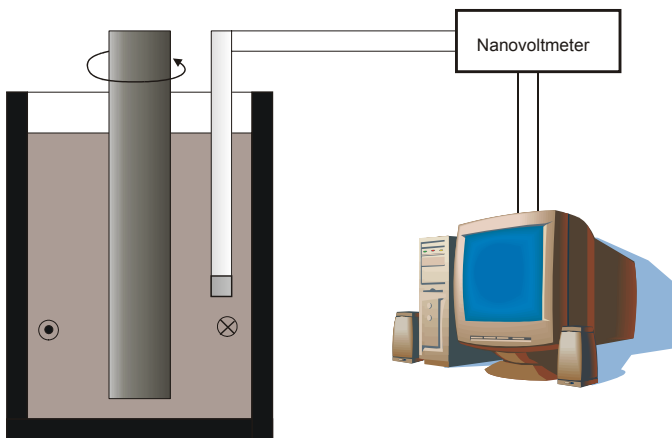


*Fig. 4.4. Setup for testing the velocity probe in molten metal. The stirrer can be rotated at different rotational velocities. Recorded signals are stored on a PC.*

Results obtained are shown in the graphs below. The temperature of the tin bath was maintained at 300 °C. In Fig. 4.5 the test conditions for the experiment that is analysed here are given. More experiments were performed, but those experiment gave more artefacts, due to external pickup by the wiring of the setup. In Fig. 4.6 it is shown that the temperature gradient over the probe was low during an experiment with different rotational velocities applied to the stirrer.
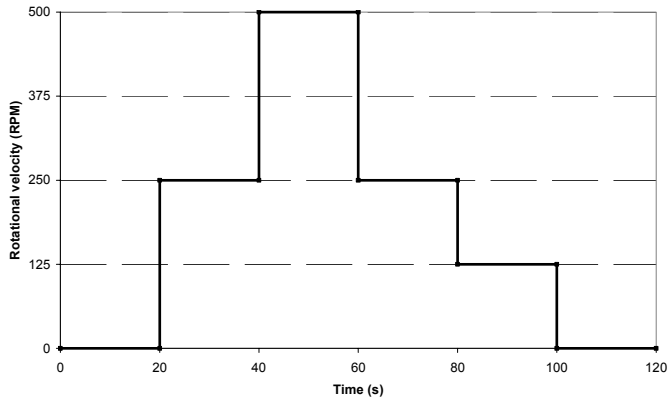


*Fig. 4.5. Applied set-point velocity profile. The rotational velocity of the stirrer is given in round per minute. .*
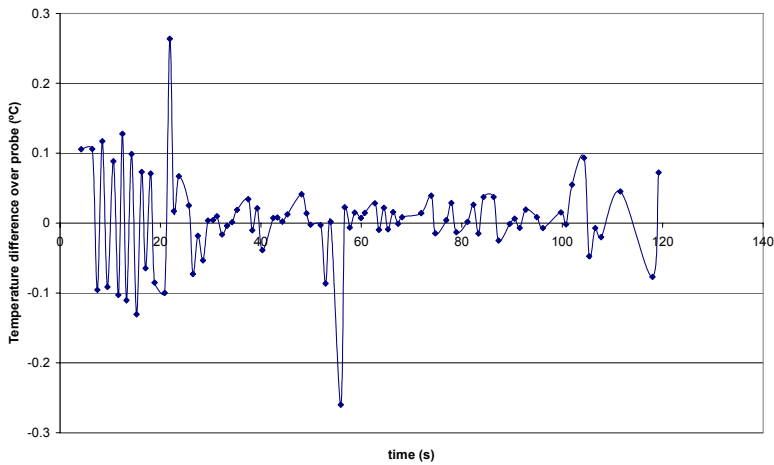


*Fig. 4.6. Temperature difference along velocity probe during experiment with different applied velocities.*
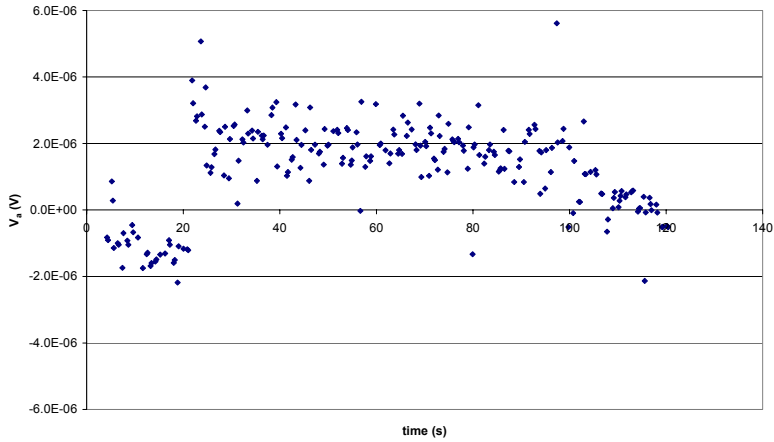
Fig. 4.7. Uncorrected $V_a$ signal. The offset is approximately -1 $\mu V$.
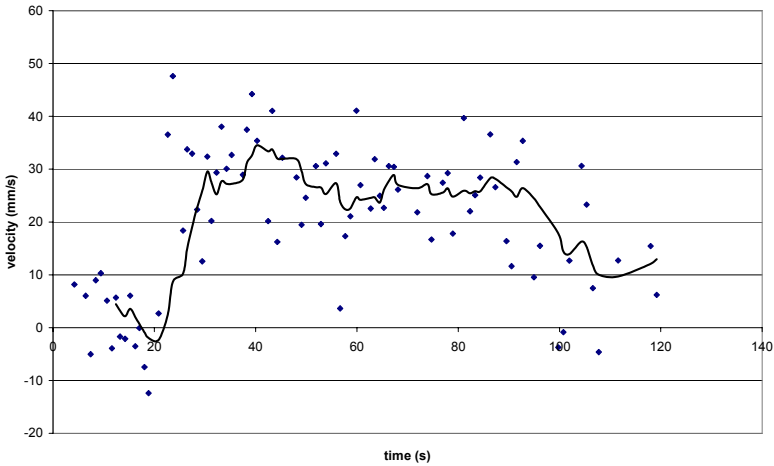


Fig. 4.8. Temperature corrected velocity measured during the experiment. The black line is a moving average over 8 data points.

The tin bath was also modelled in Flow-3D [8]. The physical data for tin were obtained from Smithell's metals reference book [9]. The 2D mesh was 60 by 60 cells in a horizontal plane perpendicular to the stirrer. This resulted in a cell size of 4 mm. This was more than sufficient to model the response of the velocity field at the position of the velocity probe. In Fig. 4.9 the response of the velocity at the location where the velocity probe was positioned is given for the applied test conditions as given in Fig. 4.5.
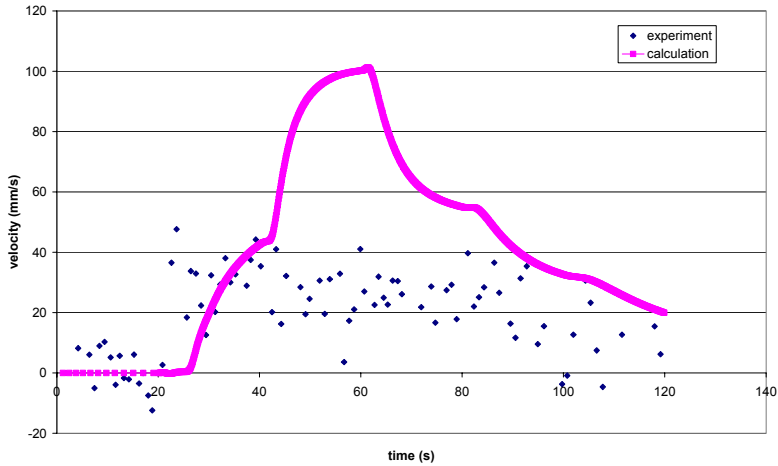
*Fig. 4.9. Modelled velocity at velocity probes position versus the measured and temperature corrected velocity.*

A vector field at time 36 s is given in Fig. 4.10. The velocity magnitude sharply decreases from the stirrer towards the non-moving sidewall of the container holding the liquid tin as can be seen in Fig. 4.11. There is a small disturbance of the velocity profile upstream of the probe. This was also observed by Ricou and Vives [3]. They also observed that this did not interfere with the velocity measurement of the probe.
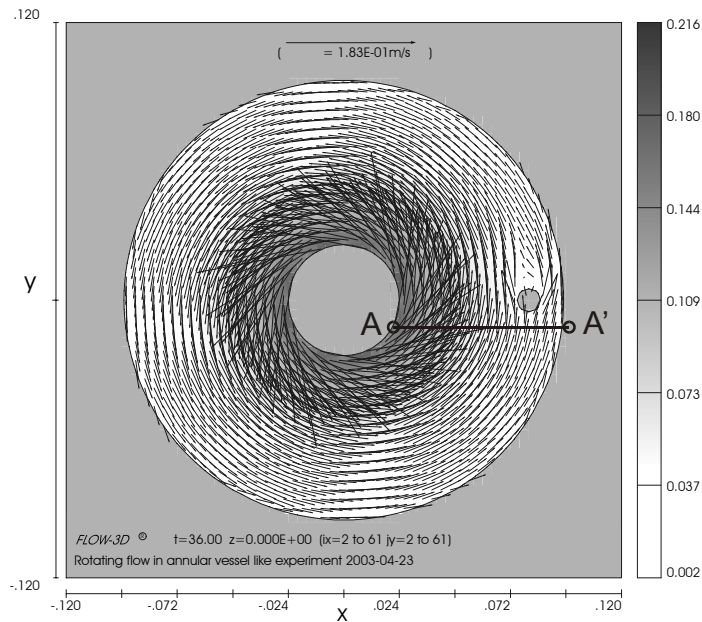


*Fig. 4.10. Calculated vector field for test conditions as specified in Fig. 4.5. The flow is splitting just before the velocity probe and recombining approximately 3 diameters after the probe.*
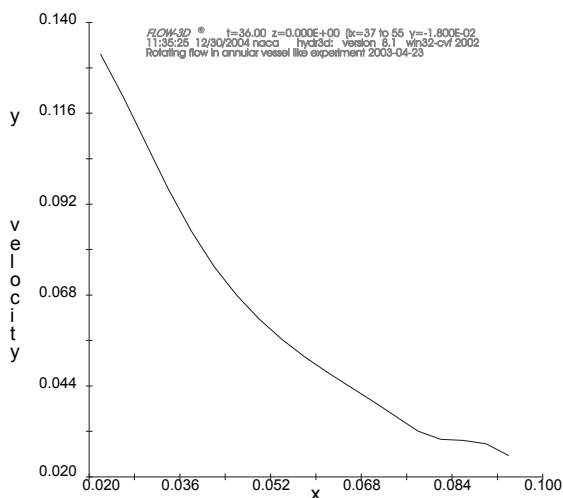
*Fig. 4.11. Velocity profile along line A-A'. There is a small disturbance in the velocity just before the probe at x=0.085. This is found experimentally [3].*

## 4.3  Discussion

It is not easy to establish a correlation between the applied velocity conditions and the measured velocity as is given in Fig. 4.8. The non-moving tin bath and the moving bath show a different signal however. It was not necessary to apply a temperature correction for the absolute temperature of the tin bath, because the temperature as function of time was almost constant. The temperature gradient over the probe was at maximum 0.2 °C. This gradient was corrected for with the aid of equations 2.44 to 2.48.

The temperature difference over the diameter of the probe, as shown in Fig. 4.6, is bigger when the tin bath is not moving. This is expected, because the stirrer mixes the fluid, diminishing existing temperature gradients. The temperature gradients are smallest in the second 250 RPM period and not in the 500 RPM period. The reason for this is not understood.

From the modelled experimental setup it followed that the velocity was not instantaneous measured by the velocity probe, because of the inertia of the tin bath. During the first 40 seconds the measured and calculated results were in close agreement with each other. After 40 seconds, when the frequency of the stirrer was changed from 250 to 500 RPM, the measured velocity signal did not follow the calculated profile anymore. The probe Reynolds number was within the valid range of $50 < Re < 15,000$ [3]. Boundary-layer transition of the flow around the cylinder was therefore not to be expected.

The probe sensitivity K could not be obtained directly by the described experiment. From the calculation of the velocity it followed that 80 $\mu$V/m.s was a reasonable value. For the thermoelectric correction coefficient $S_g$ a value of 0.35 was taken[4]. This was outside of the range of [0.31,0.21], but because the offset potentials $V_{10}$ and $V_{20}$ were not known, this was thought to be valid.

The offset voltage of $V_a$ due to material anisotropy was in the order of 1 µV. This offset was corrected together with the temperature gradient over the probe.

## 4.4  Conclusions

From the discussion the conclusion can be drawn, that it is possible to modify the probe of Kapulla et al [4] for the use in a molten metal bath. For the use of this probe in molten Aluminium DC Casting additional issues may have to solved:

- Corrosion or dissolution of the conducting parts of the probe. Aluminium is very reactive with respect to most metals;

- Magnetic shielding of the wiring from its surroundings. Like in the case of Sn, but due to added distance between the probe and the volt meter, this can be more pronounced;

- Separation of the velocity signal from the thermo-electric signal. In the Sn experiment the temperature gradients were kept very small. In DC Casting temperature gradients are very large;

- High temperature of aluminium with respect to the Curie temperature of magnets. The AlNiCo magnets applied have a Curie temperature that is high enough for liquid aluminium of 700 °C, but the magnetic field strength is already much weaker at this temperature. An alternative to a permanent magnet is an electro-magnet. This is not recommended due to the added complexity this will give to the (very small) probe.

These added difficulties will require further testing, using the experimental DC Casting facility. The probe built looks a suitable candidate for the measurements of vector fields of DC Casting experiments once the interference is under control and the above mentioned difficulties are tackled.

## References

1.    Weckman, D.C. and P. Niessen, *A Numerical Simulation of the D.C. Continuous Casting Process Including Nucleate Boiling Heat Transfer.* Metall. Trans B, 1982. **13**(4): p. 593-602.

2.    von Weissenfluh, T., *Probes for local velocity and temperature measurement in liquid metal flow.* , Int. J. Heat Mass Trans., 1985. **28**: p. 1563-1570.

3.    Ricou, R. and C. Vives, *Local velocity and mass transfer measurements in molten metals using an incorporated magnet probe.* Int. J. Heat Mass Trans., 1982. **25**: p. 1579-1588.

4.    Kapulla, R., et al., *Local velocity measurements in a thermally-stratified sodium mixing layer using a permanent-magnet probe.* Exp. Thermal Fluid Sci., 2000. **20**(3-4): p. 115-136.

5.      Zuidema, J., Jr. and L. Katgerman, *Upstream fluid flow effects in aluminium DC Casting*, in *Aluminum Alloys 2002: Their Physical and Mechanical Properties Pts 1-3*. 2002. p. 65-70.

6.      Zuidema, J., Jr. and L. Katgerman. *Cyclone Separation of Particles in Aluminium DC Casting*. in *Modelling of Casting, Welding and Advanced Solidification Processes X*. ,TMS, Destin, FL, May 2003, pp. 607-614.

7.      Venneker, B.C.H. and L. Katgerman, *Modelling issues in macrosegregation predictions in direct chill castings*. Journal of Light Metals, 2002. **2**(3): p. 149-159.

8.      Flow-3D, *Flow-3D version 8.1*. 2002.

9.      Smithells, C.J., *Metals reference book*. 1976, London: Butterworths.

# Chapter 5

## Case Studies on Mould Filling

### 5.1 Introduction

In recent years computational power has increased so much that three-dimensional transient engineering problems can be solved with numerical simulations of the processes involved. Modelling the start-up of direct chill (DC) casting is such a three-dimensional transient engineering problem that is tackled here. To help predict the maximum speed for production that runs a minimal risk of break-out is an important reason for performing simulations of the start-up of DC Casting.

The mathematical model used in the calculation of temperature profiles and stream profiles is described in chapter 2. Flow-3D [1] was used to calculate the resulting temperature and velocity fields during mould filling.

Different cases were investigated. Filling of a mould through a combo bag kind of distributor is the first case study, which will be covered in the next section.

Another case study was performed on the influence of the correct filling boundary conditions on the resulting cooling behaviour of a DC cast billet. Calculations were performed and experiments were used to tune the boundary conditions and to verify the outcome of the simulations.

### 5.2 Filling a rectangular mould through a distributor bag[1]

Filling a rectangular DC Casting mould combined with solidification is described in this paragraph. This problem is based on [2]. The filling will be described and the possible problems that can arise from the filling are discussed.

---

[1] Parts of the results published in Zuidema, J., Jr. and L. Katgerman. Modelling metal-entry in the DC cast process using Flow-3D. in Modelling of Casting, Welding and advanced Solidification Processes IX. 1999. Aachen: Shaker Verlag GmbH.

## Process Description

A drawing of the geometry used is given in Fig. 5.1. The mould is a hot top-type of 120 mm in height. The upper hot-top part of 75 mm is covered by a solid insulating material. The heat-transfer coefficient to the mould in the contact zone is set to 3000 W/m²K. The heat-transfer coefficient to air is set to 150 W/m²K. The molten aluminium enters the geometry through the hole in the distributor bag. The boundary condition used is a velocity boundary condition on top and solid walls on all other sides. The real experiment can be divided in the following stages:

- The bottom block (volume approximately 3.5 litre) is filled 25 seconds after the start of filling. the rate of filling is 0.15 litre/s.

- From there it takes another 5 seconds to fill to the position where the isolation begins. That position is 5 mm higher then the top of the bottom block.

- From 30 seconds to 95 seconds the filling rate is 0.24 litre/s. The bottom block is moving downward with 1 mm/s.

- From 95 seconds on the metal stream is reduced to 0.12 litre/s. The bottom block is moving downward with 1 mm/s.

For the calculations a different approach is taken.

Simple calculations starting from the permanent metal level 1 cm below the top of the mould were initially performed to test the moving obstacle algorithm.
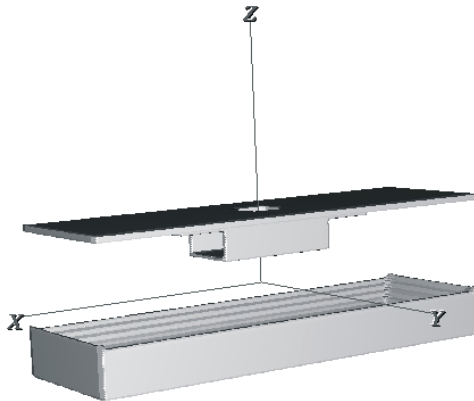


*Fig. 5.1. Geometry of a rectangular mould with a combo-bag, without vertical mould walls.*

## Turbulence Models Used

Filling through the combo-bag as given in Fig. 5.1 introduces turbulence in the fluid flow. This turbulence can be modelled by using two-equation closure models like k-ε or RNG. Another more fundamental way [4] to incorporate the turbulence is by using large eddy  simulation (LES). The time dependent fluid flow fluctuations can be captured in this way. The RNG model was validated with the LES model for the combo-bag test case. LES can be used when the length scale of the finite volumes used in the calculation is some orders of magnitude higher than the Kolmogorov length scale. The Kolmogorov length scale, time scale and velocity scale are defined by

$$\eta = \left(\frac{v^3}{\varepsilon}\right)^{\frac{1}{4}} \tag{5.1}$$

$$\tau = \left(\frac{v}{\varepsilon}\right)^{\frac{1}{2}} \tag{5.2}$$

$$\upsilon = \left(v\varepsilon\right)^{\frac{1}{4}} \tag{5.3}$$

## Computational Results

First calculations were started with a complete empty bottom block and a stagnation pressure boundary condition on top of the domain. Calculation of the first two seconds of mould filling was performed with the RNG turbulence model and without a turbulence model. The turbulent dissipation according to the RNG model was lower then 1 m²/s³. With a maximum turbulent dissipation of 1 m²/s³ the Kolmogorov length scale according to Eq. 5.1 is approximately 2E-5 m.

The start-up of the casting was performed on a finite volume mesh of dimensions of the order of 100 times the Kolmogorov length-scale. The time step size and velocity were of the order of the Kolmogorov scales. The thermal conductivity of AA 1050 was taken constant in the liquid as well as in the solid state. The thermal boundary conditions used are independent of temperature. Regions with different heat transfer coefficients are defined. The heat transfer coefficient (h) was 3000 W/m²K for the mould walls and the bottom block. The insulating material had a h of 150 W/m²K. The h from aluminium to air(void) also was set to 150 W/m²K.

Because of the number of finite volumes and the time size requirements the calculation took 5 days for every second of filling (Pentium II at 350 MHz). The free surface of aluminium coloured  by temperature is given in Fig. 5.2.

A result showing the filled mould is given in Fig. 5.3. The protrusion on the bottom is caused by metal-entry effect. The indentations on the corners of the slab are caused by differences in thermal conductivity of the insulated part of the mould and the direct contact zone with the metal mould. The mould was filled to 1 cm below the hot-top at the start of the calculation. The initial temperature was 700 ºC.

The liquidus and solidus in a vertical cross section are given in Fig. 5.4.
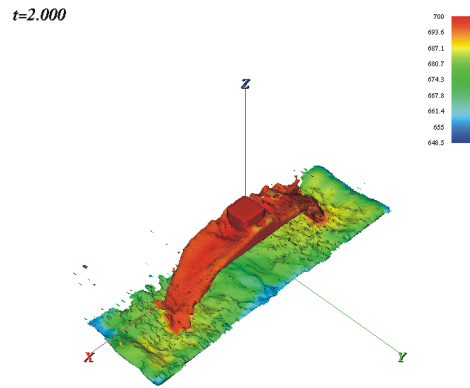
*Fig. 5.2. Result of filling DC Casting mould 2 seconds after start of metal entry. The colours represent the aluminium temperatures.*
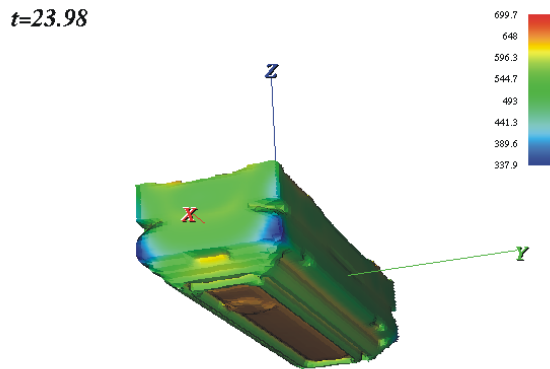


*Fig. 5.3. Bowl shaped form after 24 seconds starting with a filled mould with a uniform liquid temperature of 700 °C.*
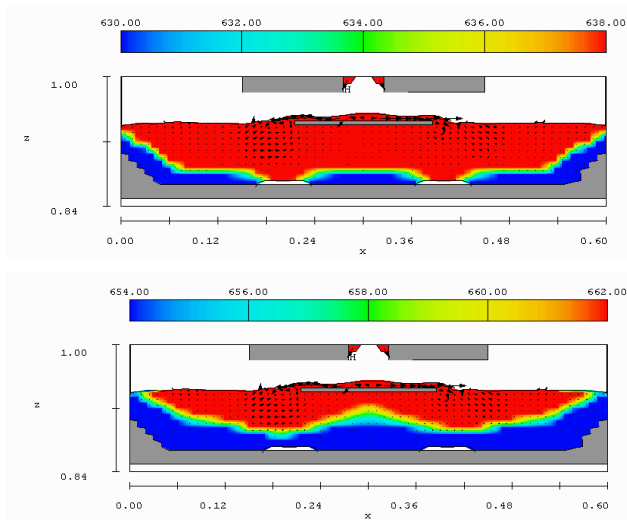
*Fig. 5.4. Result of mould filling showing  the solidus (top) and liquidus (bottom).*

## 5.3  Filling a cylindrical hot-top

The test-case described in this paragraph is a numerical simulation for a laboratory scale DC Casting unit. The casting station used is described in the 'Validation of model by Experiments' section. Start-up calculations were compared to video sequences of the experiments qualitatively. Quantitative temperature results were obtained from thermocouples inside the mould cavity. The process is described in the next section. Computational results and experimental results are given in subsequent sections and the paragraph ends with a discussion of the results.

### Process Description

Photographs of the casting station that was used to model the start-up of DC Casting is given in Fig. 5.5. The furnace used to melt aluminium is a resistance furnace. The furnace is tilted to pour the metal into the launder. The launder transports the liquid aluminium to the hot-top. Aluminium is delivered from a side opening into the hot-top. The mould is a hot top-type of 115 mm in height. The upper hot-top part of 90 mm is covered by a solid insulating material. The heat-transfer coefficient to the mould in the contact zone is set to 3000 W/m²K. The heat-transfer coefficient to air is set to 150 W/m²K. The aluminium alloy that was used to model the process was binary aluminium copper alloy with 4.5 wt% copper. The thermo-physical properties that were used to model the process are given in Table 5.1. In this table the phase diagram parameters are also given.

Table 5.1:  Thermophysical properties and phase diagram parameters[5,6].

| Properties and parameters | Symbol | Data |
|---|---|---|
| Nominal Cu-concentration | | 4.5 |
| Liquid density | $\rho_l$ | 2480 |
| Solid density | $\rho_s$ | 2790 |
| Liquid specific heat | $c_{pl}$ | 1054 |
| Solid specific heat | $c_{ps}$ | $f(T)$ |
| Latent heat of fusion | $L$ | 3.90E+05 |
| Liquid thermal conductivity | $k_l$ | 83 |
| Solid thermal conductivity | $k_s$ | $f(T)$ |
| Liquid diffusion coefficient | $D_l$ | 5.00E-09 |
| Liquid viscosity | $\mu_l$ | 0.0013 |
| Thermal expansion coefficient | $\beta_T$ | 1.17E-04 |
| Solutal expansion coefficient | $\beta_C$ | -7.30E-03 |
| Melting point of Al | $T_m$ | 933.5 |
| Partition coefficient | $k_p$ | 0.171 |
| Permeability constant | $K_0$ | 1.50E+10 |

The dendrite diameter was taken 100 μm. From this and the Kozeny-Carman relationship we find a permeability coefficient $\kappa_0 = 6.67 \times 10^{-11} \, m^2$. The coherency fraction of solid is taken as 0.15 for the simulations. The percolation limit is 0.90.

The liquidus and solidus can be calculated from Table 5.1. This results in $T_l =$ 918 K and $T_s =$ 844 K.

When the mould is filled the bottom-block is ramped up to a fixed casting speed. Cooling below the mould is described by the secondary cooling model that is described in chapter 3. The macrosegregation is modelled with a one phase model as described in chapter 2. All this models together make it possible to describe many features of the DC Casting process. Calculated temperature history and macrosegregation profiles can be verified against experimental results.
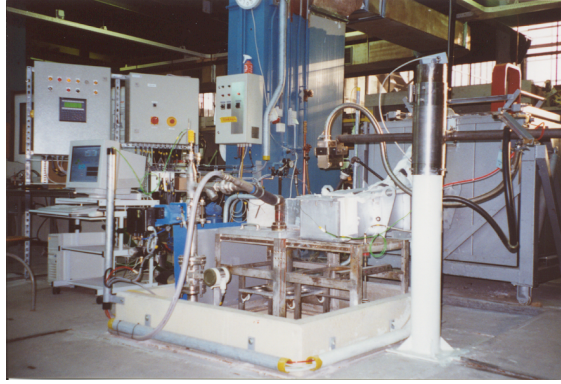
*Fig. 5.5. DC Casting station used for the validation experiments.*

## Description of model and experiment

The global casting conditions were as given in Table 5.2. Two simulation cases were derived from the observations made during the experiment. The inlet width and height for case I were taken from video recordings of the aluminium entering the hot-top. Case II used a constant pressure boundary condition over the complete launder width instead. In 'Experimental results' information that is specific to the experiments only is given. More calculation specific casting conditions are given in the next paragraph on simulation details.

Table 5.2. Casting conditions for Casting experiments, Case I and Case II

| $T_{inlet}$ (K) | 993 (to be established) |
|---|---|
| $v_{cast}$ (mm/s) | $2 \pm 0.2$ |
| melt level (mm) | $35 \pm 2$ |
| $T_{oven}$ (K) | $1001 \pm 1$ |

From the tilting furnace, the aluminium flows down the launder to the mould. It cools down to $T_{inlet}$ at the hot-top inlet. During the mould filling, the aluminium enters the mould in a thin jet. When the mould is filled the melt is kept at a constant level, controlled by a computer. This level is measured with a laser close to the hot-top opening. The water flow rate and the casting speed are also controlled with a computer. The controlling software is written in LabVIEW ™. The cooling water is pumped up from the basin through the hollow mould on to the surface of the billet. During the longer castings (more than 1.5 meter of casting length) the water temperature is rising more than 5 °C. Casting trials with tap water were therefore performed to avoid this water heating.

### Computational domain and boundary conditions

The geometry used is given in Fig. 5.6. The computational domain is discretized into 72 × 42 × 70 grids with control volume cross-sections of

approximately 3 × 4 × 3 mm in the liquid, sump and part of the solid. Further down, the vertical cell size grows gradually to about 6 mm at the bottom of the computational domain. The vertical size of the domain is 25 cm from the melt level downwards.
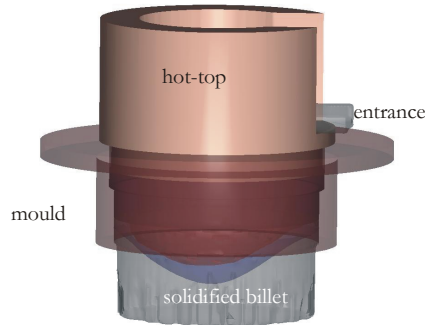


*Fig. 5.6. Hot-top geometry used in the calculations. The liquidus (red) and the solidus (blue) planes are given for a case II situation.*

The inflow boundary condition is a metallostatic pressure boundary. On the outflow a continuative condition is specified. This is an outflow condition with no gradients in the axial direction.

The hot-top is 9 cm high from the mould to the entrance level. The hot-top has a zero heat transfer coefficient with the aluminium. The mould is 25 mm high. It has a constant heat transfer coefficient of 3000 W/m²K. From the bottom of the mould to the impinging water-jet is 6 mm. This region is a air cooled region with a heat transfer coefficient of 500 W/m²K The water-cooling region is described in Chapter 3. It consists of two regions. The first is the impingement region were the water-jets hit the surface of the solidified shell. This region is 8 mm long. Downstream of this impingement region is the down-streaming region. The water cooling flow rate was taken 240 l/m min for the simulations. The simulation starts with the mould closed with a 3 cm layer of solidified aluminium alloy below it. The temperature of this layer is 700 K. The rest of the mould and hot-top are filled with the liquid aluminium alloy. The initial temperature of the liquid is 993 K, which is 75 K higher than the liquidus temperature.

**Details for Case I**

Inflow conditions for case I were taken from video recordings of the casting experiment. The initial filling took place in the form of a small jet flowing in to the mould cavity. The size of this jet was estimated from the video recording as 10 mm wide and 7 mm high. For case I we assumed that this inlet conditions remained valid even when the melt level of 35 mm was reached. For the calculation we placed an obstacle in the inlet with an aperture of 10 × 7 mm. Because the hot-top was already filled with liquid aluminium, the velocity as recorded from the experiment was not chosen as boundary condition. Instead a pressure boundary condition, with metallostatic distribution was chosen as inlet.

Calculations with and without turbulence model were carried out. The simulated casting time was 100 seconds. After 5 seconds the bottom-block was ramped up to a casting speed of 2 mm/s. This ramping up took place in 30 seconds.

Fig. 5.7 shows aluminium entering the mould in the form of a jet. Three different times are overlaid on each other.
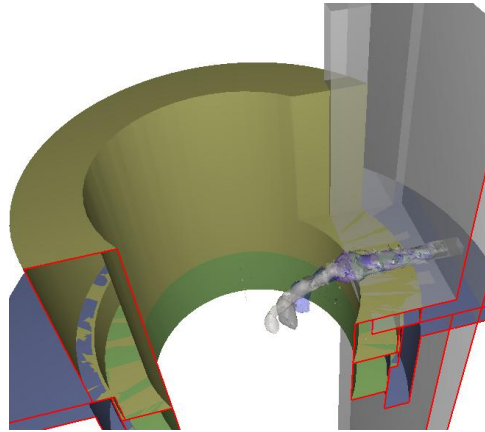


*Fig. 5.7. Computational results of the first stages of the mould filling.*

**Details for Case II**

The inflow boundary condition for case II was also a pressure boundary condition with metallostatic correction. Instead of a confined jet entering the computational domain, now the inflow took place over the complete inlet of 11.5 cm wide and 3.5 cm high. This resulted in much slower speeds at the entrance. Case II was also calculated with and without turbulence.

**Experimental results**

Not all measurements could be obtained by one experiment. The mould and hot-top would have had too many thermocouples inside for reliable undisturbed fluid flow. Three casting trials were used to collect all data needed. Casting trial 1 (Exp1) was used to obtain temperatures in fixed positions in the hot-top. For this trial 7 thermocouples were placed at different depths in the hot-top (Fig. 5.8). Casting trial 2 (Exp2) was used to obtain temperatures close to the chilled surface of the billet as a function of time. These data-sets were converted to temperature versus distance from impingement. Casting trial 3 (Exp3) was used to film the mould filling process.

Results from Exp1 are given in Fig. 5.9. In this figure only thermocouple 1 is given. The other thermocouples give similar response. The difference between the thermocouples is at maximum 5 °C except for the first 25 seconds of the casting. The bottom block was ramped up to casting speed 15 seconds after the start of mould filling. The melt level oscillated between 25 and 45 mm during the first 50 seconds of casting. After that melt level oscillations were damped and the melt level remained between 33 and 37 mm. The temperature of the cooling water rose from 18 °C to 18.5 °C in the first 100 seconds of casting. The water flow rate was

68 l/min during the first 20 seconds of casting and was then increased to 130 ± 10 l/min.

Results from Exp2 are given in chapter 3 on determination of the thermal boundary conditions in the secondary cooling zone. In Fig. 5.9 is a temperature plot of the thermocouples versus time. The casting parameters for Exp2 are globally the same as for Exp1. Temperature measurements of Exp1 are much more sensitive to the melt level, casting speed and entrance profile than those measurements from Exp2. Un important casting parameter for Exp2 is the water-flow rate. The water-flow rate is given in Fig. 5.10.
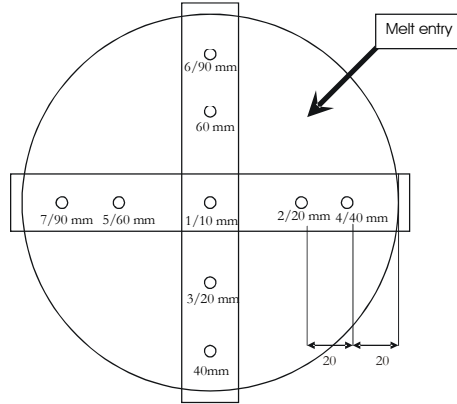


*Fig. 5.8. Thermocouple locations for exp2. The thermocouple number is given together with the height above to the bottom of the hot-top.*
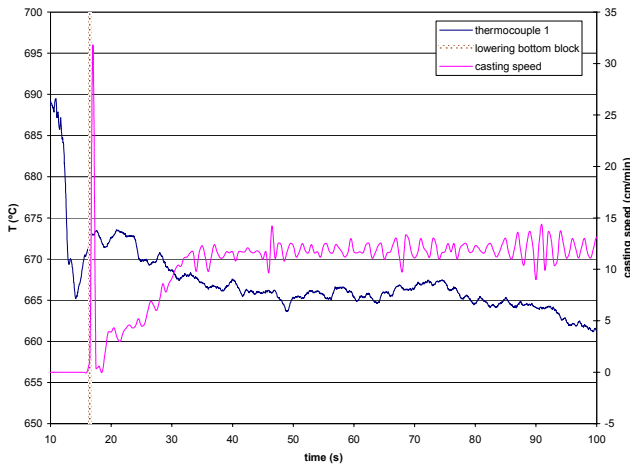


*Fig. 5.9. Temperature from thermocouple 1 and casting speed as function of time. The bottom block starts to move downwards from the time indicated by the vertical line.*
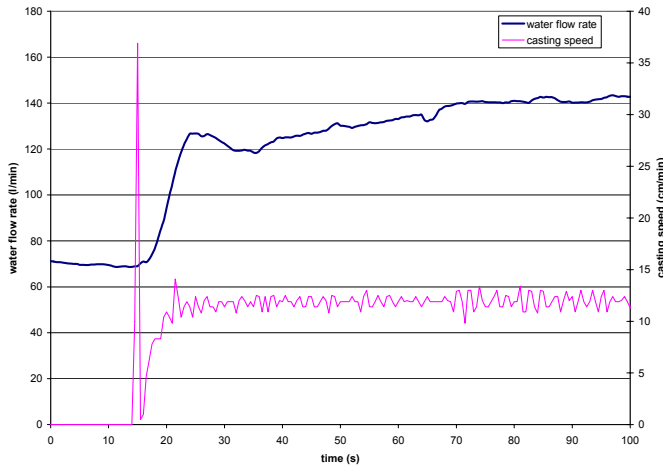
*Fig. 5.10. Water flow rate and casting speed during the first 100 seconds for Exp2.*

**Validation of model by Experiments**

To validate the computational results, experiments were performed on a DC Casting station. The filling stage was recorded with a video camera and thermocouples were inserted through the hot-top into the mould. Temperatures as function of time at different distances from the chilled billet surface could be measured in this way. Thermocouples, placed in other parts of the mould were used for registration of the filling process.

The inflow geometry and velocity were derived from video recordings during Exp3. In Fig. 5.11 two time frames from this recording are shown. The frame on the left is the time that the liquid aluminium just reached the mould. A stream of molten aluminium enters the hot-top. The initial contact with the bottom block is in the centre. From the thermocouples in the mould the first contact with molten aluminium can be measured and the subsequent temperature as function of time. Thermocouple measurement results close to the surface are given in Chapter 3. The frame on the right is just before the complete filling of the mould.



*Fig. 5.11. Inflow of liquid aluminium into the mould during the start-up of Exp3.*

**Numerical results**

A figure showing the temperature of thermocouple 1 as function of time for case I and II is given in Fig. 5.12. In this figure also the experimentally measured temperature is given. The times from the calculations and experiment are synchronised on start-up time of the bottom block movement. The sample rate for the thermocouples was about 30 per second. For the calculations data was recorded at a 1 second interval.
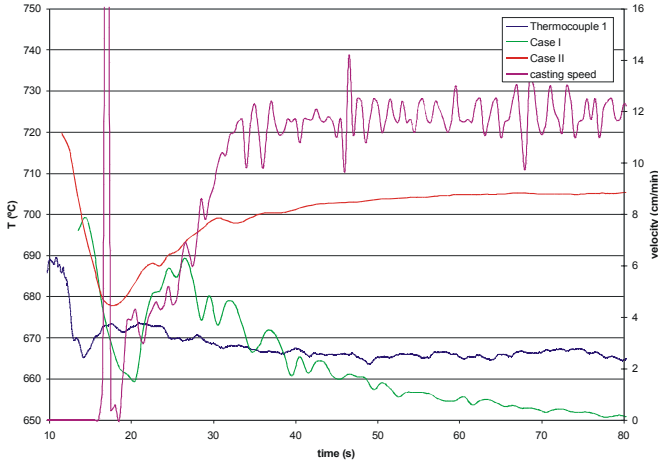


*Fig. 5.12. Calculated and measured temperature responses for thermocouple 1 and casting velocity for Exp2.*

The movement of the bottom block, or the casting velocity, is also given in Fig. 5.12. The shape of the solidus and liquidus for Case II is given in Fig. 5.13. The shape of the liquidus is not symmetrical with respect to the centreline. This is due to the entrance effect.
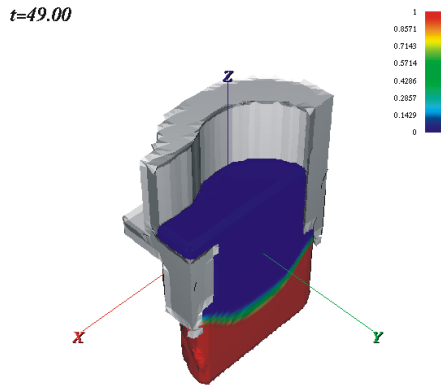


*Fig. 5.13. Filling of the DC Casting pit in hall V. The calculation started with a filling over the complete with of the mould (case II). The casting velocity is 2 mm/s.*

## 5.4  Conclusion

Calculating the filling behaviour of a rectangular mould through a combo-bag was successfully performed. Results clearly show the influence a combo-bag has on the filling of a rectangular mould. By using the RNG turbulence model, turbulence could be taken into account. This proved to be a good approximation to describe "real" turbulence.

The influence of the filling on the evolution of the cooling of a billet was calculated and verified by experiments. As was shown in Fig. 5.12, the real inlet geometry changed during the filling of the mould from a confined jet geometry to a filling from the whole width of the launder. This was as expected, but what is also shown is that case II is not completely reached, not even after the mould is completely filled. From the result it seems better to assume a Case I filling conditions for start-up simulations. Steady state was not reached in case I and II during the first 80 seconds, while the experiment showed approximately steady state behaviour from 40 seconds on as could be seen from the thermocouple readings stabilising.

For both calculated geometries it is still not possible to incorporate "real" turbulence because of both computer power and computer memory limitations. This is not expected to change in the coming ten years [4].

## References

1.    Flow-3D, *Flow-3D version 8.1*. 2002.

2.    Mortensen, D., *A mathematical model of the heat and fluid flows in direct- chill casting of aluminum sheet ingots and billets.* Metall. Mater. Trans. B, 1999. **30**(1): p. 119-133.

3.    Zuidema, J., Jr. and L. Katgerman, *Modelling metal-entry in the DC cast process using Flow-3D.*, in *Modelling of Casting, Welding and advanced Solidification Processes IX*, P.R. Sahm, P.N. Hansen, and J.G. Conley, Editors. 1999, Shaker Verlag GmbH: Aachen. p. 789-796.

4.    Johnson, R.W., *The Handbook of Fluid Dynamics*, ed. R.W. Johnson. 1998: CRC Press and Springer.

5.    Brandes, E.A. and G.B. Brook, *Smithell's Metals Reference Book.* 7 ed. 1992, Oxford: Butterworths.

6.    Vreeman, C.J. and F.P. Incropera, *The effect of free-floating dendrites and convection on macrosegregation in direct chill cast aluminum alloys Part II: predictions for Al-Cu and Al-Mg alloys.* International Journal of Heat and Mass Transfer, 2000. **43**(5): p. 687-704.

# Chapter 6

## Upstream Fluid Flow Particle Removal

The occurrence of oxides in the form of films and inclusions can give major problems during aluminium casting and processing. Inclusions and films move together with the main flow in the metal distribution system and can cause problems in further downstream processing when trapped in the solidifying aluminium. Oxides are generated by furnace handling operations and by surface disturbances in the metal flow from the holding furnaces to the DC distribution system and to the DC mould. The level of oxides and inclusions in standard DC Casting practices is controlled with the use of in-line filter boxes and degassing units. However, during the transfer from these metal treatment systems to the casting station pick up of inclusions and oxides can occur. This can be either caused by the varying efficiency of the metal treatment systems and/or uncontrolled fluctuations in the metal flow.

The first method is placing obstacles in the aluminium flow. The fluid flow is therefore modified by placing baffles in the launder. The location of these baffles is an important parameter in modifying the fluid flow behaviour. Both the controlled filling of the mould as well as entrapment of inclusions can be achieved.

The second method is modifying the flow pattern in such a way that separation of fluid from the particles occurs. This is done by employing a cyclone.

Results of numerical simulations of fluid flow with discrete particles of different size distribution are given. The finite volume method is used to solve the momentum and energy equations. The inclusions are modelled as mass particles. The forces that act on these particles are drag forces, buoyancy and inertia forces. The size distribution of particles is taken from experimental practice.

### 6.1 Theory

Separation of particles from a liquid flow can be realised by making use of the density difference between the liquid and the particles. Particles in liquid

aluminium have generally a higher density than liquid aluminium itself. Buoyancy will force the particles to the bottom of the liquid pool.

Application of Newton's second law on the forces acting on a spherical particle gives[1-3]:

$$\frac{\pi}{6}d_p^{\ 3}\rho_p\frac{\mathrm{d}\mathbf{V}_p}{\mathrm{d}t}=\frac{\pi}{6}d_p^{\ 3}(\rho_p-\rho)\mathbf{g}+\frac{1}{2}C_D\frac{\pi}{4}d_p^{\ 2}\rho(\mathbf{V}-\mathbf{V}_p)|\mathbf{V}-\mathbf{V}_p|$$
$$+\sum F_{inertia}+\sum F_{lift}+\sum F_e \tag{6.1}$$

In this equation $d_p$ is the diameter of the particle, $V_p$ is the velocity of the particle, V is the velocity of the liquid aluminium, $\rho_p$ is the density of the particle, $\rho$ is the density of the liquid aluminium, and $C_D$ is the drag coefficient which is given by[4]

$$C_D=\frac{24}{\mathrm{Re}_D}+\frac{6}{1+\sqrt{\mathrm{Re}_D}}+0.4 \tag{6.2}$$

The first term on the right hand side of Eq. 6.1 is the gravitational force. The second term is the force due to drag around the particle. The drag coefficient CD is a function of the particle Reynolds number which is defined in this case as

$$\mathrm{Re}_D=\frac{d_p\mathbf{V}}{\nu} \tag{6.3}$$

where $\nu$ is the kinematic viscosity.

$F_{intertia}$ are the inertia forces. Depending on the shape of a particle, more or less liquid aluminium is attached to it. A particle moving in a fluid is also subject to a transient viscous drag force during the development of the velocity field around the particle which is called the Basset force[1]. It is only necessary to include this "added mass" effect and the Basset force when large gradients in velocity exist. $F_{lift}$ are the lift forces that are working on the particle. An example of lift forces that can be important are the lift forces associated with shear stress gradients [5]. Fe are external forces like electromagnetic forces.

The lift force is important when the viscosity gets more important. This is the case for small particles. Those particles are subject to small particle Reynolds numbers. Suppose a particle is moving with respect to the surrounding liquid aluminium with a velocity $v_r$ in a velocity gradient $\kappa$. According to [1] the lift force or Saffman force is given by

$$F_{lift}=1.615d^2v_r\left(\mu_L\rho_L\kappa\right)^{0.5} \tag{6.4}$$

In this equation $d$ is the particle diameter, $\mu_L$ is the viscosity and $\rho_L$ is the density of the liquid. For a particle of density $\rho_S$ equal to $3.0 * 10^3$ kg/m³ in a gradient $\kappa$ of 1 /s moving in liquid aluminium with a relative velocity $v_r$ of 1 mm/s the Saffman force is 5.3 $10^{-12}$. This is approximately 2 orders of magnitude smaller than the drag force as calculated by Eq. 6.2, which is $5.7 * 10^{-10}$N. Because the values used in this example are of the same order as expected in the fluid flow modifiers that will be covered in this chapter, it is therefore reasonable to exclude the Saffman force from the calculations. In appendix B, calculations were performed to check the Saffman force equation by calculation of the force on a sphere in a velocity gradient in a square duct.

Because the remaining two forces on the right hand side of Eq. 6.1 do not play an important role compared to the two leftmost, these forces were also neglected in the computer model.

The inclusions are taken as spherical solids that have a higher density than liquid aluminium. The number of inclusions is assumed to be small, and therefore influence on the macroscopic flow pattern has not been taken into account. Collisions are also not considered in this approach.

The location of the flow modifiers is given in fig. 6.1.
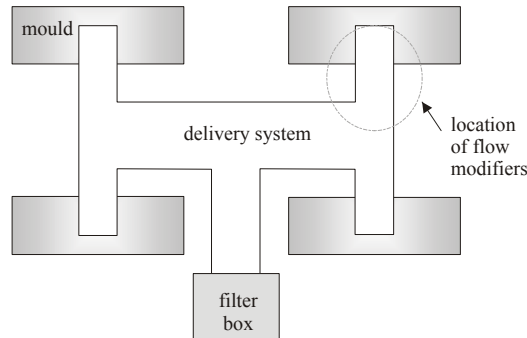


*Fig. 6.1: Schematic representation of the metal distribution system for DC Casting*

In the next paragraphs the above described method will be applied to the case of separation via weirs and dams and via an inline cyclone. The particle movement will be solved together with the momentum equations as were described in chapter 2. Flow-3D [6] was used to do the calculations. The Van Leer[7] scheme was used to discretisize the momentum equations.

## 6.2  Case1: Obstacles in the Launder

Placing dams and baffles in the launder seems an elegant and easy solution to filter out particles. In wake regions particles can disperse out of the liquid aluminium and accumulate. When the number of particles in the flow is not too high this method can be applied to the semi-continuous DC Casting process. For the case described in this paragraph the density of the particles is taken as 3000 kg/m³. Particles mainly composed of $Al_2O_3$ can have this apparent density when submerged in a flow of liquid aluminium.

In fig. 6.2 a result of a 2D calculation of the flow pattern together with the particle concentration is given as an example. In this idealized case, there was no oxides pickup from the introduced turbulence around the baffles.

To investigate the influence of particle size and velocity in the launder different calculations were performed. Spherical particles were introduced at a rate of 50 /s. The particles were randomly distributed in the boundary volumes on the left side of the computational domain. Solidification was turned off for these calculations, because solidification is not to be expected in the launder.

The locations of the obstacles were kept constant during these calculations. Calculations were performed on two different launder velocities. A velocity to create a 19 cm diameter billet at 2 mm/s was tested first. The calculation was 2 dimensional. The width of the launder was chosen to be 10 cm for this case, which is a typical value for these kind of launders. The velocity was increased to almost twice as large for the second series of calculations.
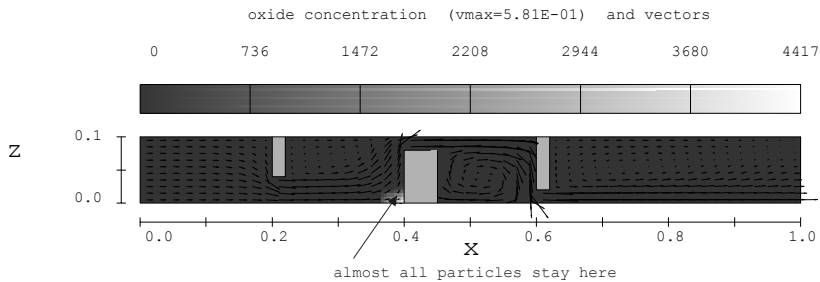


*Fig. 6.2: Velocity vectors of the liquid aluminium together with the oxide concentration. The z-direction is the vertical direction. The particle size was 200 μm in diameter.*

## 6.3  Case2: Cyclone

The idea of using a cyclone in refining a stream of molten aluminium originated from the fact, that a very long distance is needed to let the denser particles precipitate on the bottom of a separation system. A cyclone offers a very long route for the liquid in a small casing. A liquid entering a cyclone swirls

downward on the periphery of the cyclone and is then forced upwards through the core to the outlet.

The cyclone, that was envisaged to be used in the removal of particles from the distribution system upstream of the mould, was combination of a hydro cyclone and a high efficiency cyclone [4]. Hydro cyclones normally operate at very high Reynolds numbers and therefore have a fairly large pressure drop over the cyclone. High efficiency cyclones are designed to be used for gas/solid separation, but have a much lower pressure drop when used with liquids at low Reynolds numbers. After some rather simple fluid dynamics calculations based on these basic shapes, a geometry was found that looked promising for removing particles from a stream of liquid aluminium.

The geometry that was used for the numerical calculations was also used as a basis for the water model. A drawing and a photograph of the water model of the cyclone is given in fig. 6.3. The cyclone operates when it is completely filled with aluminium. This can be arranged in the water model by submerging the cyclone in a water tank.

Because the water model testing was not planned until after the calculations were nearly finished, there was no possibility to do the complete set of calculations for water as a medium and hollow glass spheres as particles. Only one calculation based on water with hollow glass spheres was performed to verify the hypothesis' made on similarity that are made in section 6.5.
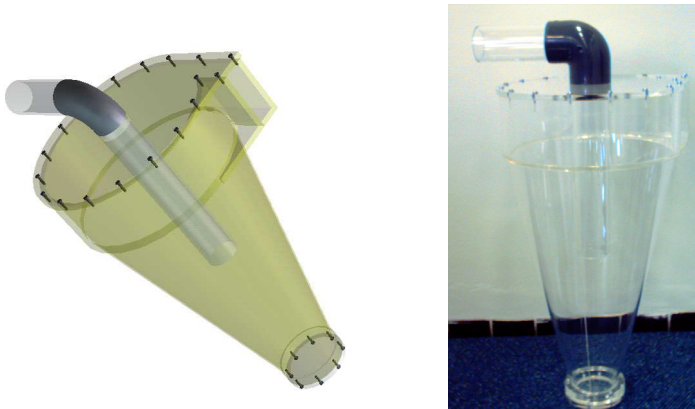


*Fig. 6.3:  Pictures of the cyclone. On the left a schematic picture is given, on the right a photo.*

## 6.4  Results

### Separation Efficiency

The effectiveness of a particle removal system is given as:

$$R = \frac{\dot{N}_{in} - \dot{N}_{out}}{\dot{N}_{in}}$$

<div align="right">(6.5)</div>

where $N_{in}$ is the number of particles entering the system at its inlet per unit of

time and $N_{out}$ is the number of particles leaving the system at its outlet per unit of time. The maximum efficiency is therefore 1, when all entering particles get trapped inside the system, and 0 when all entering particles leave the system. The efficiency is measured from the slope in the "number of particles in the system" versus time graph.

## Calculations with Obstacles

The first calculation that was performed on the launder with the baffles, was a calculation with particles of 200 μm diameter introduced at a rate of 50 /s at the entrance (left side) of the launder. This size is not realistic in practice, but is practical for initial calculations. As can be seen in fig. 6.2, most particles got trapped in the wake region of the first obstacle in the flow. From the numerical results it followed that 4417 out of 5000 particles that entered the flow domain in 100 seconds stuck at the first baffle. This calculation was of an idealised situation. Laminar flow conditions were assumed for this calculation. The Reynolds number for flow through a duct of the size of the launder at the 10 mm/s fluid velocity was just below 1800, so turbulence is not expected to develop in the launder. This is not completely right because turbulence could develop at the baffle locations, where a strong directional change is forced on the flow. Therefore the influence of turbulence was investigated. Also the particle size of 200 μm diameter is easy to filter out. Calculations that were based on smaller sizes 10 − 150 μm gave a different result that can bee seen in Fig. 6.4. When a k − ε model for turbulence was employed in the calculation this resulted in a slightly higher efficiency.
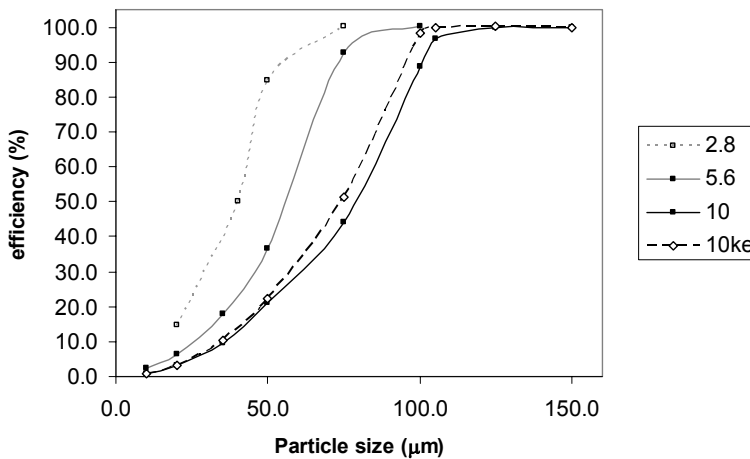


*Fig. 6.4: Efficiency versus particle size for two different flow velocities in the launder. The legend captions give the launder velocity in mm/s. The difference between laminar (10) and turbulent via the k-ε model (10ke) is shown.*

**Calculations with a Cyclone**

Modelling the particle trajectories in a complex geometry is an application where the particle model can be fully used. The fluid-particle interaction model is solved at the end of the momentum equation iterations. In fig. 6.5 the geometry of the cyclone is given translated to a special 3D graphical format (STL) as it was used by Flow-3D to filter spherical particles out of a liquid aluminium stream. The same alloy, Al 4.5 wt% Cu, as used for the case in chapter 5 was also used for the simulation of the fluid flow in the cyclone. The enthalpy and the concentration equations were not solved. To study the effectiveness of the cyclone in filtering out spherical particles, the inlet velocity was fixed to a constant value of 10 mm/s. This value was chosen to have a typical mass flow rate to cast a 20 cm diameter billet at 1 mm/s.
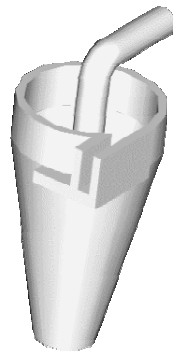
*Fig. 6.5: STL file of In-line cyclone unit for filtering small particles out of the melt as used by Flow-3D.*

In fig. 6.6 the efficiency $R$ is given as function of the size of the particles that enter the cyclone. Small particles predominantly leave the cyclone and enter the launder, whereas most large particles are trapped inside the cyclone.     The efficiency was derived from figures as shown in fig. 6.7. The slope of the curve after steady state has been reached is compared to the rate of particles entering the cyclone. That rate was chosen 1/s for the calculations. This rate does of course not correspond to real numbers of particles, but is high enough for the calculations, which covered about 1000 to 4000 seconds of casting.  In fig. 6.7 it can be seen that the slope in not constant when steady state is reached. Small fluctuations remain.
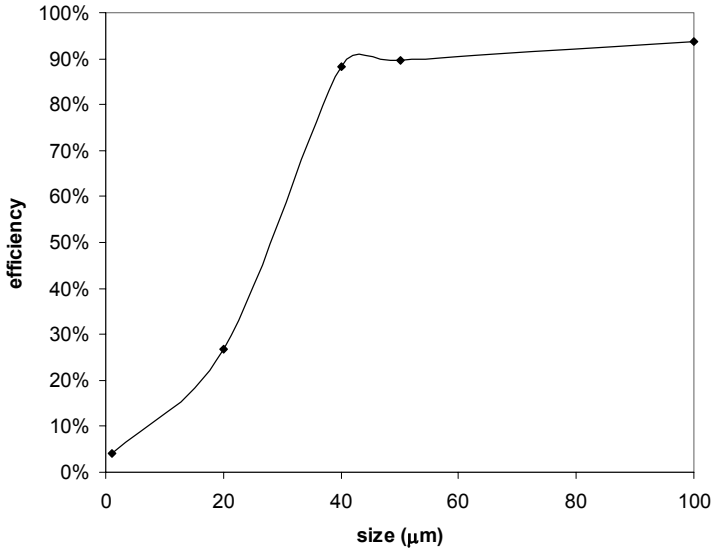
*Fig. 6.6: Efficiency R of the cyclone as a function of the particle size diameter. The velocity at the entrance of the cyclone was 10 mm/s.*

In fig. 6.8 the cyclone is shown with particles after 2000 seconds of operation. This figure is given to show the loci where particles will end up when they get trapped in the cyclone. The cyclone shown here was a cyclone with a particle trap below its bottom. When particles get inside this trap they are not easily removed from it again. The efficiency, as shown in fig. 6.6, was calculated without this trap. In that case the particles stay in a ring on the bottom of the cyclone. The efficiency with the trap was estimated for particles with a diameter of 20 μm, and resulted in an efficiency of 0.5, which is higher than the 0.3 that resulted from the cyclone without particle trap. Because of computer power limitations, only some calculations with a trap were performed. The intention of this research was to prove the viability of the concept and not to find the "best" cyclone.

To be able to better understand the differences between the results of the water model experiments and the calculations for a liquid aluminium alloy, a calculation based on the conditions for the water model was performed and compared to a liquid aluminium alloy calculation using the same volume flow rate. The result for the number of particles as function of time for both cases is given in Fig. 6.9.
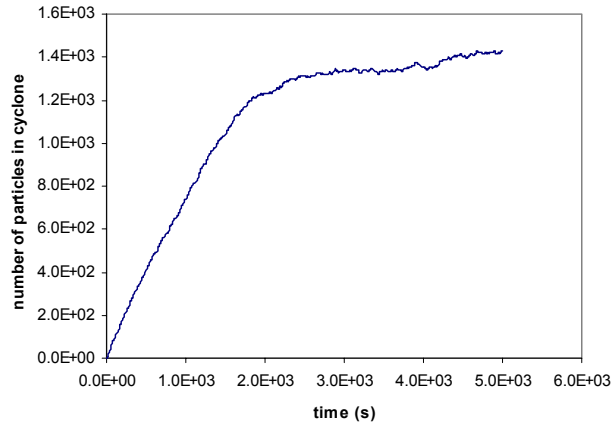
*Fig. 6.7: Particle concentration in the cyclone versus time for particles with a diameter of 1 μm.*
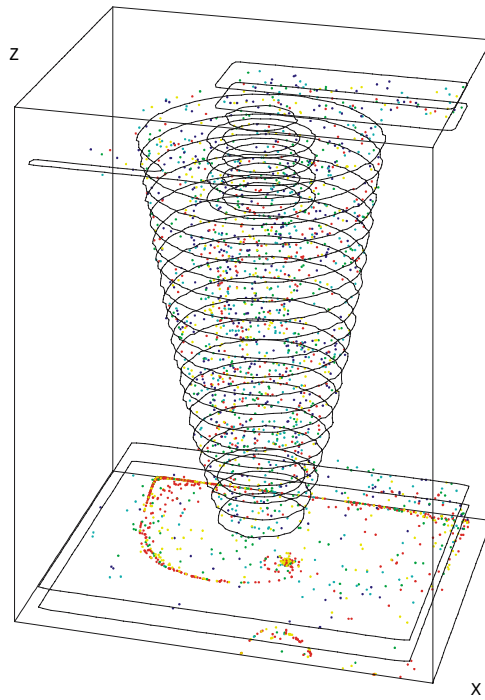


*Fig. 6.8: Particles tracks inside the cyclone. A number of particles is trapped below the cyclone.*
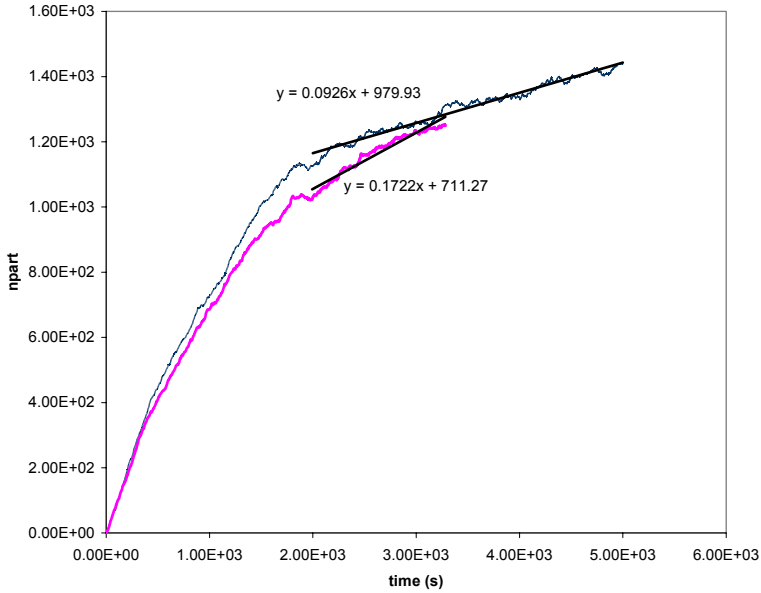
*Fig. 6.9: Comparison between water and aluminium 4.5% copper alloy in particle filtering. The thin line that has the lowest end slope is for the Al 4.5%Cu case.*

## Water Model Results of Cyclone

The water model as described in paragraph 6.3   is tested under conditions that enable comparison to the numerical results. In Fig. 6.10 two photos are given that show the lower part of the cyclone in operation. The light dots are hollow glass spheres. The time shift between the two photos is 1/25th of a second. A digital DV camera was used to record the movement of particles in the cyclone. The resolution of the frames was 768 by 576 pixels. With this resolution it was necessary for the expected velocities to zoom in to parts of interest in the cyclone.
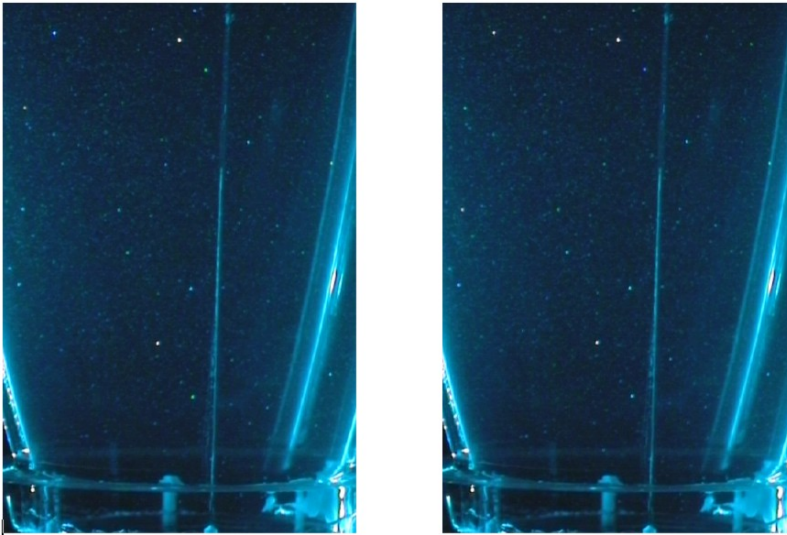
*Fig. 6.10: Two photos showing the lower part of the cyclone during a experiment. The right photo is taken 1/25th of a second later than the left photo.*

When a correlation between the two photos is performed a vector field can be constructed that shows the velocity of the particles in the cyclone. One such a vector plot is shown in Fig. 6.11. By carefully examining a sequence of vector fields the correct interrogation area can be defined.

For different flow velocities an average vector field in different parts of the cyclone can be plotted. This is shown in Fig. 6.11 for a flow rate of 1.4 l/min. For 5.2 l/min the results are shown in Fig. 6.12.
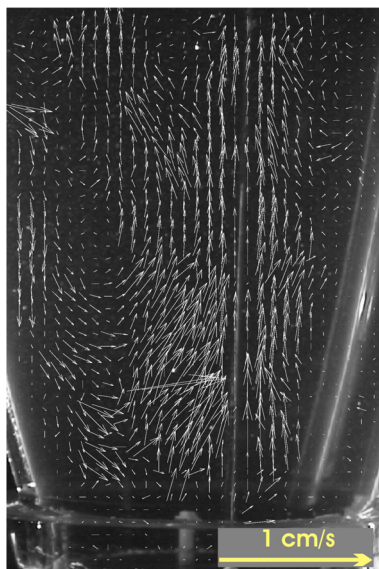


*Fig. 6.11: Vector plot taken from a cross correlation of Fig. 6.10. The water flow rate is 1.4 l/min*
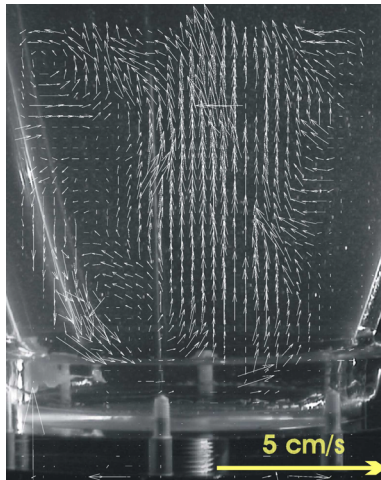
*Fig. 6.12: Vector field in the bottom section of the cyclone for a water flow rate of 5.2 l/min*

## 6.5  Discussion

In this paragraph first the numerical results are analysed. After that the water model results will be discussed.

### Obstacles

The placement of dams and weirs in the launder to modify the flow behaviour of the molten aluminium has been proven to work under ideal conditions. The obstacles introduce areas with very low velocities. It was observed that in those areas particles denser than the surrounding aluminium got sufficient time to sink to the bottom. The drawback of this method is that small fluctuations in the flow behaviour may reintroduce the sunken particles back in the flow. The flow velocities that were necessary to filter out the particles of 20 μm needed to be smaller than 3 mm/s to reach an efficiency of 15%.

### Cyclone

A first observation that can be made regarding the similarity between the calculations based on fluid aluminium and the experiments using water as the fluid medium, is that to compare both situations, it is necessary to have the same Reynolds number around the particles (see Eq. 6.1 to 6.3) . Because the Reynolds number for the liquid aluminium alloy is approximately twice as large as the Reynolds number for a similar water flow rate, this multiplier of 2 is applied to the water experiments to make comparison possible. An opposing effect is that the density difference between the water and the hollow glass spheres is probably slightly smaller than the difference between the aluminium alloy and the $Al_2O_3$ particles. Because this difference causes an decrease of less than 10% in the friction term of Eq. 6.1, it is ignored for the comparison.

**Numerical Results**

The results show that the numerical model predicts the collection of a percentage of the particles that enter the cyclone in the bottom part of it. The bigger particles are more easily captured than the smaller ones. The reason that not all particles are filtered out is caused by turbulence in the cyclone. This turbulence forces particles from the outside downwards rotating layer to the core of the cyclone. In this core the aluminium is flowing upwards taking the oxides with it. The drag is of more influence on the smaller particles because of their bigger area/volume ratio. The particles are assumed to be spherical. Non spherical particles can stick together more easily because of their bigger area to volume ratio. Also the drag on these particles can be higher. This can decrease the efficiency of the cyclone. Turbulence can also be beneficial for the efficiency of the cyclone. Because turbulence causes small fluctuations in the aluminium velocity, it increases the change of collisions between particles and thus increases the mean particle size.

Inertia forces and lift forces were not taken into account. The justification for this was that no big velocity gradients exist in the cyclone. This is the case in laminar fluid flow. The particles never cross the boundary between the downwards circling velocity and the upwards moving core section of the cyclone. When turbulence gets stronger, the change exist that particles are moved through this boundary with the turbulent fluctuating part of the fluid motion. Lift forces associated with shear stress gradients can also become important in such situations.

When the cyclone is compared to obstacles in the launder, it can be seen that the efficiency of the cyclone is better for the smaller particles ($d_p < 50\ \mu m$), whereas the efficiency of the obstacles in the flow is higher for the bigger particles.

**Water model results**

Qualitative examination of the flow pattern observed from the video footage of the experiment, showed close resemblance to the numerically calculated flow patterns. The efficiency was not measured. For particles of 10 $\mu m$ diameter, using the same flow rate of 1.4 l/min as for the calculation , it was observed that some particles settled on the bottom of the cyclone in a circle. This calculation also showed this behaviour at an estimated efficiency of lower than 5 percent. For the higher flow rate of 5.2 l/min all particles were removed from the cyclone. When these results are compared with fig. 6.6 it is seen that the estimated efficiency of less than 5% in the experiment is lower than the 10-15% that was predicted by the numerical simulation.

## 6.6  Conclusions

Removal of particles from a stream of fluid aluminium was investigated with the aid of both computer modelling and experiments. Computer modelling showed the potential of increasing the time between the furnace and the mould. The effect from this increase in flow pattern was first shown for the case of dams and weirs in the launder. This proved to work under idealised conditions.  The concept of a cyclone was deduced from these calculations. The cyclone was partly optimised by trial and error using a simplified numerical description. This "optimised" cyclone was evaluated in more detail. Both numerical calculations and experiments in a water basin were employed to study the effectiveness of this cyclone. The outcome of the experiments showed close correlation with numerical results.

## Recommendations

The "hydro" cyclone concept that was described in this chapter has been proven viable based on a limited set of experiments and calculations. More elaborate water testing is recommended to assess the efficiency of the cyclone for different shaped particles. The influence of density differences between the fluid medium and the particles should be evaluated using numerical calculations and experimental validation based on a limited number of experiments using the water model.

Once the cyclone has been evaluated using above techniques and proven viable for the intended purpose, hot experiments using liquid aluminium should be undertaken as a final check on the results obtained by the calculations and water experiments.

Since the flow modifiers in the launder gave higher efficiency than the cyclone at particles bigger than 50 μm, a combination of flow modifiers in the launder and a cyclone just before the mould looks worth investigating. The combination of both methods could be a good way to filter out both the smaller and the bigger particles.

## *Nomenclature*

| | | |
|---|---|---|
| d | diameter | [m] |
| $\rho$ | density | [kg/m³] |
| V | velocity | [m/s] |
| t | time | [s] |
| g | gravitation constant | [m/s²] |
| $C_D$ | drag coefficient | |
| F | force | [N] |
| $\nu$ | kinematic viscosity | [m²/s] |
| *N* | particle flux | [/s] |

subscripts

p    particle

dimensionless numbers

Re    Reynolds

## *References*

1. Clift, R., J.R. Grace, and M.E. Weber, *Bubbles, Drops, and Particles*. 1978, NY: Academic Press.

2. Poirier, D.R. and G.H. Geiger, *Transport Phenomena in Materials Processing*. 1994, Warrendale: TMS.

3. Szekely, J., *Fluid Flow Phenomena in Metals Processing*. 1979, NY: Academic Press.

4. Johnson, R.W., *The Handbook of Fluid Dynamics*, ed. R.W. Johnson. 1998: CRC Press and Springer.

5. Saffman, P.G., J. Fluid Mech., 1965. **22**: p. 385-400.

6. Flow-3D, *Flow-3D version 8.1*. 2002.

7. van Leer, B., *Towards the Ultimate Conservative Difference Scheme. IV. A New Approach to Numerical Convection*. J. Comput. Phys., 1977. **23**: p. 276.

# Appendix A

## Patent describing cyclone to purify a stream of molten aluminium

This appendix contains an abstract of the patent that was derived from the calculations and measurements that were described in chapter 6.

**Patent Number(s):**
WO2004001078-A1; NL1020919-C2; AU2003248155-A1

**Title:**
Molten metal purifying method e.g. for aluminum, involves generating spiral flow within chamber to purify molten metal introduced into chamber, and discharging purified metal vertically through outlet placed above inlet

**Inventor Name(s):**
ZUIDEMA J

**Patent Assignee Name(s) and Code(s):**
NETHERLANDS INST METALS RES (NEME-Non-standard)

**Derwent Primary Accession Number:**
2004-062802 [47]

**Abstract:**
NOVELTY - Molten metal stream having high melting point is purified by pouring the molten metal into a chamber (12) through an inlet (13) and generating a spiral flow in the chamber. The purified metal is vertically discharged using a central flow within the spiral, through an outlet (14) placed above the inlet. The removed impurities are collected at a space (17) at bottom of the chamber.

USE - For purifying molten metal e.g. aluminum or aluminum alloy.

ADVANTAGE - The molten metal can be purified efficiently by performing spiral flow of molten metal in the chamber.

DETAILED DESCRIPTION - INDEPENDENT CLAIMS are also included for:

(a) molten metal purifying device; and

(b) casting installation.

DESCRIPTION OF DRAWING(S) - The figure shows the schematic view of molten metal purifying device.

chamber (12)
inlet (13)
outlet (14)
collection space (17)
outlet sleeve (20)

**Drawing:**
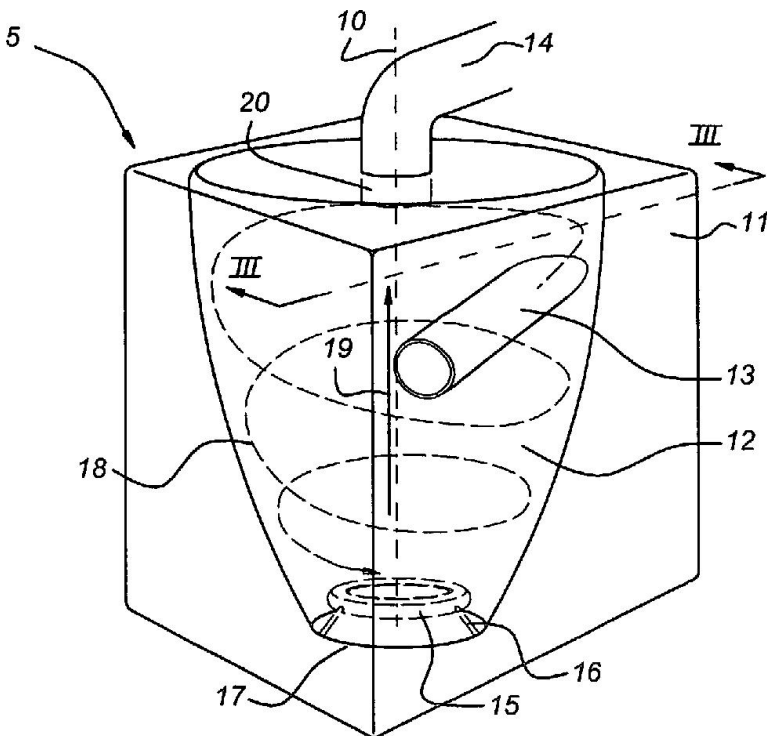


**International Patent Classification:**
C22B-009/02; C22B-021/06

**Derwent Class:**

M25 (Production and refining of metals other than iron)

**Derwent Manual Code(s):**

M25-G01

| Patent Number | Publ. Date | Main IPC | Week | Page Count | Language |
|---|---|---|---|---|---|
| WO2004001078-A1 | 31 Dec 2003 | C22B-009/02 | 200406 | Pages: 12 | English |
| NL1020919-C2 | 06 Jan 2004 | | 200419 | | |
| AU2003248155-A1 | 06 Jan 2004 | | 200447 | | |

**Application Details and Date:**

| | | |
|---|---|---|
| NL1020919-C2 | NL1020919 | 21 Jun 2002 |
| AU2003248155-A1 | AU248155 | 23 Jun 2003 |
| WO2004001078-A1 | WONL00459 | 23 Jun 2003 |

**Further Application Details:**

| | | | |
|---|---|---|---|
| AU2003248155-A1 | Based on | Patent | WO2004001078 |

**Priority Application Information and Date:**

NL1020919      21 Jun 2002

**Designated                                                                                 States**

WO2004001078-A1

(National): AE; AG; AL; AM; AT; AU; AZ; BA; BB; BG; BR; BY; BZ; CA; CH; CN; CO; CR; CU; CZ; DE; DK; DM; DZ; EC; EE; ES; FI; GB; GD; GE; GH; GM; HR; HU; ID; IL; IN; IS; JP; KE; KG; KP; KR; KZ; LC; LK; LR; LS; LT; LU; LV; MA; MD; MG; MK; MN; MW; MX; MZ; NI; NO; NZ; OM; PG; PH; PL; PT; RO; RU; SC; SD; SE; SG; SK; SL; TJ; TM; TN; TR; TT; TZ; UA; UG; US; UZ; VC; VN; YU; ZA; ZM; ZW

WO2004001078-A1

(Regional): AT; BE; BG; CH; CY; CZ; DE; DK; EA; EE; ES; FI; FR; GB; GH; GM; GR; HU; IE; IT; KE; LS; LU; MC; MW; MZ; NL; OA; PT; RO; SD; SE; SI; SK; SL; SZ; TR; TZ; UG; ZM; ZW

# Appendix B

## Saffman force on single particle in shear flow

The Saffman lift force on a particle was derived in the 1960's [64]. In Flow-3D a fluid flow simulation was done to calculate the Saffman force on a spherical particle of 40 μm diameter in a vertical velocity gradient. The simulation was done in 3D with no velocity gradient in the y direction. This enabled to check if the force working in the y-direction was zero. Below is a picture of the situation that was modelled in a x-z plane through the sphere.
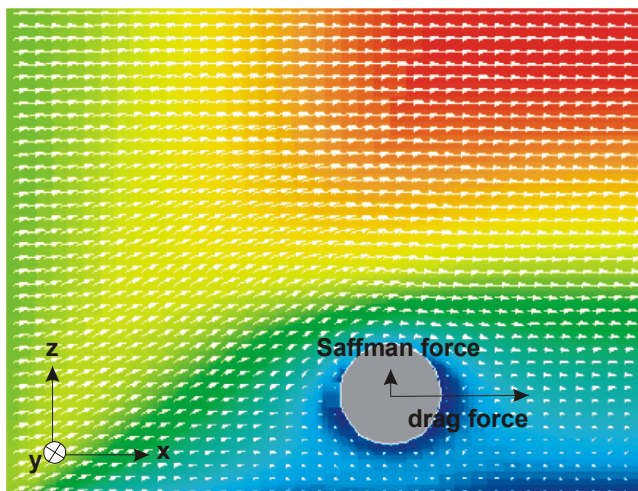


*Fig. B1: Picture showing the x-z plane through the sphere. The undisturbed velocity gradient is parabolic with zero velocity at the lower z and maximum velocity at the top of the domain. The Saffman force and the drag force are given schematically.*
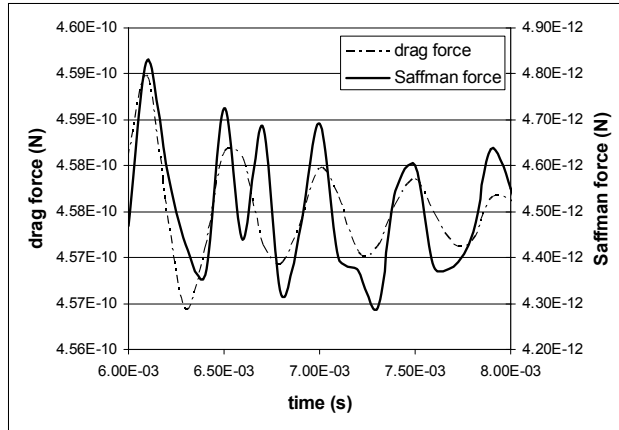
*Fig. B2: Steady state force on spherical particle in shear gradient as calculated by Flow-3D*

The Saffman lift force and the drag force on the particle is given Fig. B2 in steady state situation. The small fluctuations are numerical fluctuations. The drag force on the particle is 2 orders of magnitude bigger than the Saffman lift force. This result is consisted with the mathematical approach that was taken in chapter 6. Results from this simulation and the analytical calculation in chapter 6 permit the neglecting of the Saffman force in the simulations of the fluid flow modifiers in that chapter.

# Appendix C

## Flow-3D scripts and code

In this appendix the Flow-3D scripts that were used to get to the results for the different chapters are given. The custom Fortran code that was written to calculate secondary water cooling heat fluxes is described after that. The code that was used to count particles is given at the end. This code is included in the newest version of Flow-3D.

### C.1  Script for mould filling

```
Hal5 25 feb 2003 coh=0.3 per=0.9 jet
starten vanaf een lege mould
bottom block steel + aluminium rim

$xput
  remark='units are SI',
  twfin=100.,
  itb=1,
  gz=-9.8,
  imobs=1,
  delt=1e-3,
  ifenrg=3, ifrho=1, ihtc=2,
  isolid=1,
  iorder=3,
  sprtdt=.1,
  hflv1=150.,hflv2=1e9,hflv3=1e9,
  remark=' void 1=lucht 2:water 3: water',
  dtmin=1e-6,
  hpltdt=0.1,
  imphtc=2,
  dum1=4e-3, remark='Qw=4e-3 m^2/s',
  slddt=50.,
```

```
  ifpk=1,
  apltdt=1.,
  ifvis=0,
  ishrnk=1,
  ipdis=1,
  imp=2,
  dtmax=5e-3,
  epsadj=1.,
  impvis=1,
  tedit(1)=16.5, tedit(2)=40., tedit(3)=100., tpltd(1)=16.5,
  tpltd(2)=23.5, tpltd(3)=20.,
$end

$limits
  itflmx=250,
  itmax=1000,
$end

$props
  rhof=2460., rhofs=2750.0, thexf1=1.17e-4, cv1=1054.,
  cvs1=958., pofl1=0.0, thc1=90., thcs1=180.,
  tstar=918.19, clht1=3.90e5, tl1=918.19, tniyam=-1.0,
  tsdrg=7920.0, fscr=.95, fsco=0.3, muc00=0.0,
  muc0=1.0, muc2=0.0, muc3=0.0, mutmp2=0.0,
  mutmp3=1.0,  teut=821.2, ceut=0.000,
  cexf1=-0.0073, cstar=4.5, dratio=-1., units='si',
  mu1=0.000013,
  ts1=843.95, tmelt=933.5, pcoef=0.171,pcav=-4e4,
  cangle=135., sigma=0.84,
$end

$scalar
  nsc=1, iseg=1,isclr(1)=3,
$end

$bcdata
  wb=3, wt=2,
  wl=2, wr=9, wf=1, wbk=1,
  tbc(1)=298., tbc(6)=298., tbc(3)=298., tbc(5)=298.,
  tbc(4)=298., hwall1(1)=1., hwall1(6)=1., hwall1(3)=1.,
  hwall1(5)=1., hwall1(4)=1.,
$end

$mesh
  nxcelt=75,   px(1)=90e-3,px(2)=330.e-3,
  nycelt=65,   py(1)=90e-3,py(2)=184.9e-3,
  nzcelt=110,
```

```
  pz(1)=1600e-3,pz(2)=1914e-3,
  py(3)=215.1e-3, py(4)=310e-3,
  pz(3)=2043e-3,
  pz(4)=2078e-3, nzcell(1)=50,
  nzcell(3)=7, sizez(4)=5e-3, sizez(3)=5e-3,
  sizez(2)=2e-3,
$end
$bcdata
  wr=6, fbc(2)=1., flhtr=2.05, ipbctp(2)=0,
        sclbc(2,1)=4.5,
  tbc(2)=973.,
  wl=9,
  ubct(1,2)=-0.28, ubct(2,2)=-0.29, ubct(3,2)=0., ubct(4,2)=-0.084590,
  timbct(1)=0.,timbct(2)=16.5, timbct(3)=16.6, timbct(4)=34.,
  wf=2, wbk=2, wb=2, wt=2,
  tbc(3)=973., tbc(4)=973., tbc(5)=973., tbc(6)=973.,
$end


$mesh
  nxcelt=20,
  px(2)=0.40,
  px(1)=0.33,
  sizex(1)=3.2e-3,
  nycelt=34,
  py(2)=0.255,
  py(1)=0.145,
  nzcelt=2,
  pz(2)=2.050,
  pz(1)=2.043,
$end



$obs
  remark='1:hot-top 2:ring 3:mold 4:goot+inlet 5:lucht',
  remark='6:waterjet 7:downstream 8:geest',
  nobs=10,IAVRCK=2,avrck=-5.,
  igen(1)=3,igen(2)=3,igen(3)=3,igen(4)=3,
  iob(7)=7,ioh(7)=1,iob(5)=5,iob(6)=6,ioh(5)=1,ioh(6)=1,
  igen(8)=0,zl(8)=1550e-3,ifob(8)=4,
  hobs1(1)=500e-3,hobs1(2)=500e-3,hobs1(3)=3000.,hobs1(4)=500e-3,
  kobs(1)=1.,kobs(2)=1.,kobs(3)=45.,kobs(4)=1.,
  rcobs(1)=1e6,rcobs(2)=1e6,rcobs(3)=3.6e6,rcobs(4)=1e6,
  rcobs(5)=1293.,kobs(5)=25e-3,hobs1(5)=500.,
  rcobs(6)=2e12,kobs(6)=2000.,hobs1(6)=1e10,
  htcob(5,6)=150.,hobv2(5)=150.,
  twobs(1,1)=298.,twobs(1,2)=298.,twobs(1,3)=298.,twobs(1,4)=993.,
  twobs(1,5)=318.,twobs(1,6)=318.,
```

```
    wtobs(1,8)=0.,wtobs(2,8)=-2e-3,
          tobs(1)=16.5,tobs(2)=34.,
    zh(7)=1914e-3, ral(7)=96.35e-3, rah(7)=106.35e-3,
    trnx(7)=200e-3, trny(7)=200e-3,
    ioh(6)=1, zl(6)=1914e-3, zh(6)=1922e-3, ral(6)=96.35e-3,
    rah(6)=106.35e-3, trnx(6)=200e-3, trny(6)=200e-3,
    ioh(5)=1, zl(5)=1922e-3, zh(5)=1928e-3, ral(5)=96.35e-3,
    rah(5)=106.35e-3,
    trnx(5)=200e-3, trny(5)=200e-3,
    twobs(1,7)=318., kobs(7)=2000., rcobs(7)=2e12, hobs1(7)=1e9,
    fstl(4)='stl\obstacle4.stl',
    iob(9)=9, ioh(9)=1, igen(9)=3, fstl(9)='stl\bottomblock-r-kleiner.stl',
    twobs(1,9)=318., kobs(9)=45., rcobs(9)=3.8e6, hobs1(9)=1500.,
        imo(9)=-1,wtobs(1,9)=0.,wtobs(2,9)=-2e-3,
    iob(10)=10, ioh(10)=1, igen(10)=3, fstl(10)='stl\bottomblock-r-kleiner.stl',
    twobs(1,10)=318., kobs(10)=45., rcobs(10)=3.8e6, hobs1(10)=1500.,
        imo(10)=1,wtobs(1,10)=0.,wtobs(2,10)=-2e-3,
$end


$fl
  nfls=1,fzl(1)=1878e-3,frah(1)=100e-3,fzh(1)=1930e-3,
  ftrnx(1)=200e-3,ftrny(1)=200e-3,fral(1)=80e-3,
$end


$bf
  nbafs=1,
  bxl(1)=2.74559E-01,bcz(1)=-1.,bcc(1)=2043e-3,
$end


$temp
  tempi=973., tvoid=298.,
  ntmp=2,treg(1)=318.,treg(2)=973.,
  tzh(1)=1928e-3,tzl(2)=2043e-3,
  tral(1)=0.08, trah(1)=0.1, ttrnx(1)=0.2, ttrny(1)=0.2,
$end


$motn
$end


$grafic
  anmtyp(1)='vel',
  anmtyp(2)='tn',
  anmtyp(3)='sclr1',
      WINTL(1)='thermocouple 1',npmov(1)=0,
      XLOC(1)=0.2, YLOC(1)=0.2, ZLOC(1)=1.963,
      WINTL(2)='thermocouple 2',npmov(2)=0,
      XLOC(2)=0.2424, YLOC(2)=0.1576, ZLOC(2)=1.973,
```

```
        WINTL(3)='thermocouple 3',npmov(3)=0,
        XLOC(3)=0.1576, YLOC(3)=0.1576, ZLOC(3)=1.973,
$end

$parts
 $end
   Documentation: general comments, background, expectations, etc.
   sclbc(2,1)=4.5,
```

## C.2  Script for steady state processing with secondary cooling

```
 DC Casting sec. cooling model at 200 l/min cyl 12 cm/min (sc1)
 12 cm/min T in mould 660 C

$xput
   remark='units are SI',
   twfin=200.,
   itb=1,
   gz=-9.8, ifenrg=3, ifrho=1, ishrnk=1,
   ihtc=2, ifvis=0,
   ipdis=1,
   omega=1.,
   iorder=3,
   dum1=5.34E-03,remark='200 l/min',
   imphtc=1,
   iadix=1,iadiz=1,epsadj=1.,
   trest=200., deltr=1e-2, itrst=1, isolid=1,
   iscrst=1,
   epshtc=1e-3,
$end

$limits
   itmax=1000,
$end

$props
   rhof=2550.,
   rhofs=2700., thexf1=1.27e-4, cv1=1175.000000, cvs1=1050.,
   pofl1=0.000000, thc1=95., thcs1=180.000000,
   clht1=396e3,
   tsdrg=7920., mu1=0.001300,
   units='si',
   dratio=0., remark=' dratio in gui was on -1?',
   ts1=933.5, tl1=933.5,
$end

$scalar
$end
```

```
$bcdata
  wr=2, wb=6, wt=6, wbc(6)=-2e-3,
  wbc(5)=-2e-3, tbc(6)=937., tbc(2)=318., hwall1(2)=1e8,
  rwall(5)=0., sclbc(6,1)=4.5,
  wl=1, wf=1, wbk=1, tbc(4)=318.,
  hwall1(4)=1e8,
$end

$mesh
  icyl=1,
  nxcelt=60,   px(2)=9.5e-2,
  nycelt=1,
  nzcelt=180,   pz(2)=0.51,
  px(1)=0.0, pz(1)=0.0,
  pz(3)=0.61,
  px(3)=0.1,
  sizex(2)=0.5e-3,
  pz(4)=0.75, sizez(3)=0.5e-3,
  nzcell(1)=25, sizez(2)=2e-3,
  py(2)=0.01, py(1)=0.0,
$end

$obs
  avrck=-3.1,
  nobs=6, iob(1)=1, ioh(1)=1,
   zl(1)=0.65, zh(1)=0.75, kobs(1)=1.,
  rcobs(1)=1e6, hobs1(1)=1.,
  iob(2)=2, iob(3)=3, ioh(2)=1, ioh(3)=1,
  zl(2)=0.625, zh(2)=0.65, zh(3)=0.625, ral(2)=0.095,
  ral(1)=0.095, ral(3)=0.095, rah(2)=0.1, rah(1)=0.2,
  rah(3)=0.1, twobs(1,1)=318., twobs(1,2)=523., twobs(1,3)=318.,
  kobs(2)=80., kobs(3)=100., rcobs(2)=1e10, rcobs(3)=1.293e10,
  hobs1(2)=5000., hobs1(3)=2500.,
  iob(4)=4,ioh(4)=1,zh(4)=0.615,
  zl(3)=0.615, zl(4)=0.607, ral(4)=0.095, rah(4)=0.1,
  kobs(4)=2e3, rcobs(4)=1e10, hobs1(4)=1e10,
  iob(5)=5,ioh(5)=1,zh(5)=0.607,ral(5)=0.095,rah(5)=0.1,
  kobs(5)=2e3, rcobs(5)=1e10, hobs1(5)=1e9,
  iob(6)=6, ioh(6)=1,ifob(6)=4, wtobs(1,6)=-2e-3,
  zh(6)=1.,
  twobs(1,4)=318., twobs(1,5)=318.,
  htcob(3,4)=150.,
$end

$fl
  nfls=1, fioh(1)=1, frah(1)=0.0955, preg(1)=0.,
```

```
   wreg(1)=-2e-3,
$end

$bf
$end

$temp
   tempi=820.,
$end

$motn
$end

$grafic
$end

$parts
$end
```
   Documentation: general comments, background, expectations, etc.


## C.3  Script for cyclone calculations

```
 Cyclone 2 blz 4 schrift vin=5e-3 RNG
 Gemaakt van stl files
 restart van 1600s


$xput
   remark='units are ...',
   twfin=6000.,
   itb=0,
   gz=-9.8, ifenrg=0, ifvis=4,
   delt=1e-4,
    iorder=3,
   icav=0,
   ipdis=1,
     isolid=0,
   dtmin=1e-9,
   epsadj=1.,
   tedit(1)=6000,
   hpltdt=10.,
   trest=2500., deltr=1e-1,
   ihonly=1, ifvelp=1,
   apltdt=50,
   pltdt=6000,
$end
```

```
$limits
$end

$props
  rhof=2460.,
  rhofs=2750., cv1=1054., cvs1=958., pofl1=0.000000,
  thc1=95., thcs1=180., tstar=918.19, clht1=390e3,
  tl1=918.19, tniyam=-1.000000, tsdrg=1.000000, fscr=1.000000,
  fsco=0.000000, mu1=0.001300, muc00=0.000000, muc0=1.000000,
  muc2=0.000000, muc3=0.000000, mutmp2=0.000000, mutmp3=1.000000,
   teut=821.2, ceut=0.33, cexf1=-0.73,
  cstar=4.5e-2, dratio=-1.000000, units='si',
  pcav=-1e4,
$end

$scalar
$end

$bcdata
  wl=6, wr=8,
  wbk=1, ubct(1,1)=0., ubct(2,1)=1e-2, timbct(1)=5e-1,
  timbct(2)=5.,
  tkebc(1)=1.25e-5,
$end

$mesh
  nxcelt=60,   px(2)=.24,
  nycelt=50,
  nzcelt=100,   pz(2)=1.24,
  px(1)=-.2, py(1)=-0.18, py(2)=0.18, pz(1)=0.5,
$end

$obs
  avrck=-3.,
  nobs=1, iob(1)=1, iob(2)=1, ioh(1)=1,
  ioh(2)=1,       igen(1)=3,       fstl(1)='i:\calc\icaa8\filters\cyclone2\cyclone.stl',
trnx(1)=-1.001,
  trny(1)=-1.001,
  trnx(2)=-1.001, trny(2)=-1.001,
  igen(2)=3, fstl(2)='i:\calc\icaa8\filters\cyclone2\pijpje08.stl',
  trnz(1)=-0.001, trnz(2)=-0.001,
$end

$fl
   fioh(1)=1,  ifdis(1)=-1,
  ffstl(1)='E:\icaa8\filters\cyclone2\liq.stl',
  ffstl(3)='E:\icaa8\filters\cyclone2\liq2.stl',
```

```
  fioh(2)=1,
  fioh(3)=1, ifdis(3)=-1,
$end

$bf
$end

$temp
$end

$motn
$end

$grafic
  anmtyp(1)='part',
$end

$parts
  ipflag=1, ippkt=1,
   nsspec(1)=2, rate(1)=1., spmin(1)=19.99e-6,
  spmax(1)=20.01e-6,
  prho=3000.,
  xppl(1)=-0.19, xppr(1)=-0.18, yppf(1)=-0.14, yppbk(1)=-0.13,
  zppb(1)=1.01, zppt(1)=1.09,
$end
  Documentation: general comments, background, expectations, etc.
```

## C.4  Fortran code for secondary cooling

```fortran
      subroutine qeval(twin,tfin,fin,sa,hi1,hi2,scale,
     1                 htcobs,htcfl,hasrct)
c
c            evaluate wall heat flux and heat transfer
c                 coefficients
c                                         11/01
c
c    ****************************************************************
c    **                       notice                             **
c    **  this subprogram contains flow science, inc. proprietary **
c    **        trade secret and confidential information.        **
c    **                                                          **
c    **              unauthorized use prohibited                 **
c    **          copyright 1985-2000 flow science, inc.          **
c    ****************************************************************
c
c
      use arrays_module
c
      use meshcb_module
c
      include '../comdeck/precis.f'
      include '../comdeck/params.f'
      include '../comdeck/dparam.f'
      include '../comdeck/acctrm.f'
```

```
      include '../comdeck/cntrl.f'
      include '../comdeck/const.f'
      include '../comdeck/index.f'
      include '../comdeck/phiou.f'
      include '../comdeck/state.f'
      include '../comdeck/dumn.f'
c
      real*8 nulam,nuturb,nunat
c
      include '../comdeck/func.f'
c
c
c   var   dis   description
c  twin    i    wall temperature
c  tfin    i    fluid temperature
c   fin    i    fluid fraction
c    sa    i    wall surface area
c  vbar    -    fluid velocity
c  hi1     i    input heat transfer coefficient, to fluid #1
c  hi2     i    input heat transfer coefficient, to fluid #2
c  scale   i    length scale for correlations
c htcobs   i    conduction heat transfer coefficient between obstacle
c               surface and tw node in obstacle
c  htcfl   i    conduction heat transfer coefficient between obstacle
c               surface and tn node in obstacle
c hasrct   o    area-heat transfer coefficient product

      include '../comdeck/ijk.f'
      include '../comdeck/mijk.f'
      include '../comdeck/pijk.f'


c
      hasrct=zero
      if(nmat.eq.1 .and. fin.lt.emf) return
      h1=hi1
      h2=hi2
c       custom code for secondary water cooling
      if(h1.gt.9.9d9) then
c       impingement region
        if(tfin.lt.393.) then
          h1=(2.73d4*(tfin-273.)-1273088.915)/(tfin-twin)
        endif
        if(tfin.ge.393.and.tfin.lt.423.) then
          h1=(94252.48352*(tfin-273.)-9240434.453)/(tfin-twin)
        endif
        if(tfin.ge.423.) then
          h1=(12259.18138*(tfin-273.)+3058560.867)/(tfin-twin)
        endif
      endif
      if(h1.gt.9d8) then
        c=-4.01d6*dum1**2.+6.9d4*dum1+628.
        h1=max(1500.,min(4d6/(tfin-twin),max(((-
1.67d5+c*(tfin+318.)/2.)
     2  *dum1**0.3333*(tfin-318.)+100*(tfin-363.)**3)/(tfin-twin),
     3  ((-1.67d5+c*(tfin+318.)/2.)*dum1**0.3333*(tfin-318.))
     4  /(tfin-twin))))
      endif
c       end of custom code

      if(nmat.eq.1) h2=zero
      if(scale.lt.ztest) then
```

```
c         treat h's as contact resistances
          if(h1.gt.zero) then
            denom=htcobs+htcfl+htcobs*htcfl/h1
            h1=htcobs*htcfl/denom
          endif
          hbar=h1
          if (nf(imjk).ge.1.and.nf(imjk).le.6) fnl=fn(imjk)
          if (nf(ipjk).ge.1.and.nf(ipjk).le.6) fnr=fn(ipjk)
          if (nf(ijmk).ge.1.and.nf(ijmk).le.6) fnf=fn(ijmk)
          if (nf(ijpk).ge.1.and.nf(ijpk).le.6) fnbk=fn(ijpk)
          if (nf(ijkm).ge.1.and.nf(ijkm).le.6) fnb=fn(ijkm)
          if (nf(ijkp).ge.1.and.nf(ijkp).le.6) fnt=fn(ijkp)
          fnmax=max(fnl,fnr,fnf,fnbk,fnb,fnt)
          if (nf(imjk).ge.8.and.vf(imjk).gt.0) hbar=fnmax*h1
          if (nf(ipjk).ge.8.and.vf(ipjk).gt.0) hbar=fnmax*h1
          if (nf(ijmk).ge.8.and.vf(ijmk).gt.0) hbar=fnmax*h1
          if (nf(ijpk).ge.8.and.vf(ijpk).gt.0) hbar=fnmax*h1
          if (nf(ijkm).ge.8.and.vf(ijkm).gt.0) hbar=fnmax*h1
          if (nf(ijkp).ge.8.and.vf(ijkp).gt.0) hbar=fnmax*h1
          goto 510
          if(nmat.eq.2. and. h2.gt.zero) then
            denom=htcobs+htcfl+htcobs*htcfl/h2
            h2=htcobs*htcfl/denom
            hbar=(one-fin)*h2+fin*h1
          endif
          goto 510
        endif
c
c         treat nonzero h's as given heat transfer rates
c
c         minimum htc based on fluid and obstacle conduction
c
        denom=htcfl+htcobs
        hcond=htcfl*htcobs/denom
        if(nmat.eq.1) hcond=hcond*fin
        if(h1.gt.zero .and. (nmat.eq.1 .or. h2.gt.zero)) goto 500
        if(ihonly.ge.2) then
          hbar=hcond
          go to 510
        endif
        dtabs=fabs(twin-tfin)
        include '../comdeck/mijk.f'
        vbar=fsqrt(u(ijk)*u(ijk)+u(imjk)*u(imjk)+
     1          v(ijk)*v(ijk)+v(ijmk)*v(ijmk)+
     2          w(ijk)*w(ijk)+w(ijkm)*w(ijkm))
       vbar=0.7071067812*vbar
            tfilm=0.5*(tfin+twin)
            if(iaccf.eq.0) go to 100
                include '../comdeck/pijk.f'
                include '../comdeck/oijk.f'
                call accxcl(u,v,w,leneax,icorx)
                call accycl(u,v,w,leneax,icory)
                call acczcl(u,v,leneax,icorz)
  100     continue
          grav=fsqrt( (gx-accx)**2 +
     1                (gy-accy)**2 +
     2                (gz-accz)**2 )
c
c                      use correlations to evaluate htcs
c
c                             fluid #1
```

```
c
          if(h1.gt.0.0 .or. fin.le.0.0) go to 200
              if(fliq(ijk).lt.omfscr) go to 200
              den1=rho1cl(p(ijk),tn(ijk))
              ren1=den1*vbar*scale/mu1
              sqre=fsqrt(ren1)
              rep8=ren1**0.8
              prp33=prn1**0.333333
c
              nulam=0.664*prp33*sqre
              nuturb=prp33*(0.036*rep8-836.0)
c
              nunat=0.0
              if(grav.lt.ztest .or. ihonly.eq.1) go to 190
                  den1f=rho1cl(p(ijk),tfilm)
                  beta1=-dr1dt(p(ijk),tfilm)/den1f
                  grsh1=grav*beta1*dtabs*scale**3*(den1f/mu1)**2
                  grpr=fabs(grsh1*prn1)
                  if(grpr.le.1.0e+9) nunat=0.57*grpr**0.25
                  if(grpr.gt.1.0e+9) nunat=0.14*grpr**0.333333
c
  190         continue
              h1=fmax3(nulam,nuturb,nunat)*thc1/scale
c
c                         fluid #2
c
              denom=h1+htcobs
              h1=htcobs*h1/denom
  200     continue
          if(nmat.eq.1 .or. h2.gt.0.0 .or. fin.ge.1.0) go to 500
              den2=rho2cl(p(ijk),tn(ijk))
              ren2=den2*vbar*scale/mu2
              sqre=fsqrt(ren2)
              rep8=ren2**0.8
              prp33=prn2**0.333333
              nulam=0.664*prp33*sqre
              nuturb=prp33*(0.036*rep8-836.0)
c
              nunat=0.0
              if(grav.lt.ztest .or. ihonly.eq.1) go to 290
                  den2f=rho2cl(p(ijk),tfilm)
                  beta2=-dr2dt(p(ijk),tfilm)/den2f
                  grsh2=grav*beta2*dtabs*scale**3*(den2f/mu2)**2
                  grpr=fabs(grsh2*prn2)
                  if(grpr.le.1.0e+9) nunat=0.57*grpr**0.25
                  if(grpr.gt.1.0e+9) nunat=0.14*grpr**0.333333
  290         continue
              h2=fmax3(nulam,nuturb,nunat)*thc2/scale
              denom=h2+htcobs
              h2=htcobs*h2/denom
  500 continue
      hbar=(1.0-fin/vf(ijk))*h2+fin/vf(ijk)*h1
      hbar=fmax2(hbar,hcond)
  510 continue
      hasrct=sa*hbar
      return
      end
```

## C.5  Fortran code for particle counting

```fortran
      subroutine qsadd
c
c     this subroutine is called when nsc>0.  the call is near the
c     end of the cycle, after the pressure/velocity update and fluid
c     advection and diffusion,
c     but before new cells are initialized, nf's are set,
c     and the chemistry routine is called.
c
c     ****************************************************************
c     **                    notice                   **
c     **  this subprogram contains flow science, inc. proprietary  **
c     **       trade secret and confidential information.       **
c     **                                              **
c     **              unauthorized use prohibited           **
c     **          copyright 1985-2002 flow science, inc.        **
c     ****************************************************************
c
      use mblock_module
c
      use arrays_module
c
      use arrayp_module
c
      use meshcb_module
c
      use voids_module
c
#ifdef SINGLE
      include '../comdeck/precis4.f'
#else
      include '../comdeck/precis.f'
#endif
c
      include '../comdeck/params.f'
      include '../comdeck/phiou.f'
      include '../comdeck/cntrl.f'
      include '../comdeck/const.f'
      include '../comdeck/diag.f'
      include '../comdeck/edit.f'
      include '../comdeck/grfdat.f'
      include '../comdeck/state.f'
      include '../comdeck/acctrm.f'
      include '../comdeck/pardat.f'
      include '../comdeck/scala.f'
      include '../comdeck/dumn.f'
```

```
c          scalar species sources and sinks
c
c     (not currently implemented)
c
c     variable        description
c     --------        ------------------------------
c     ijk             current cell index
c     ipjk             cell to right
c     imjk             cell to left
c     ijpk             cell to back
c     ijmk             cell to front
c     ijkp             cell to top
c     ijkm             cell to bottom
c     i               current x index
c     j               current y index
c     k               current z index
c
c     t               time
c     delt            time step size
c
c     nbl             current mesh block number
c
c     x(i)            mesh coordinate at right of cell ijk
c     xi(i)           cell ijk center
c     y(j)            mesh coordinate at back of cell ijk
c     yj(j)           cell ijk center
c     z(k)            mesh coordinate at top of cell ijk
c     zk(k)            cell ijk center
c     delx(i)          cell size in x direction
c     dely(j)          cell size in y direction
c     delz(k)           cell size in z direction
c     rri(i)          correction factor for cylindrical coordinates
c                     i.e., delta y at x(i) is dely(j)/rri(i)
c
c     vf(ijk)         open volume fraction in cell
c     afr(ijk)        open area fraction at right face
c     afb(ijk)         open area fraction at back face
c     aft(ijk)        open area fraction at top face
c
c     u(ijk)          x velocity at right face
c     v(ijk)          y velocity at back face
c     w(ijk)           z velocity at top face
c     fn(ijk)         fluid fraction in cell at beginning of cycle
c     p(ijk)          pressure in cell
c     tn(ijk)         temperature in cell
c     rhoe(ijk)        density*specific energy in cell
c     arint(ijk)      free surface area in cell
```

```
c      rho(ijk)      density in cell (only for variable density)
c
c      nf(ijk)       free surface indicator in cell
c         =0         interior fluid cell
c         =1         surface cell - fluid at left
c         =2         surface cell - fluid at right
c         =3         surface cell - fluid at front
c         =4         surface cell - fluid at back
c         =5         surface cell - fluid at bottom
c         =6         surface cell - fluid at top
c         =7         surface cell - cavitating cell
c         >=8          void cell -- void id number
c
c      nsc           number of scalars
c      sclr(ijk,ns)  concentration of scalar ns at cell ijk
c                    after advection and diffusion
c                    (update this variable to change scalar
c                    concentration)
c      sclrn(ijk,ns) concentration of scalar ns at cell ijk
c                    at beginning of time step
c
c
c      skip over if no scalars exist and this subroutine is used for
c         scalar sources
       if(nsc.eq.0) return
c
c ---  loop over real cells (set boundary cells in subroutine bc)
       do 100 k=kprb,kprt
       do 100 j=jprf,jprbk
       do 100 i=iprl,iprr
c -----  calculate current cell index
        include '../comdeck/ijk.f'
c ------  skip calculation for completely blocked cells
        if(vf(ijk).lt.em6) goto 100
c --------  calculate "neighbor indices"
         include '../comdeck/mijk.f'
         include '../comdeck/pijk.f'
c ----------  skip empty (void) cells
          if(fn(ijk).lt.emf .and. nmat.eq.1) go to 100
c
c              ... enter changes here ...
c
c
 100   continue
c
c   user's code here ...
c
```

```
c ------ Count particles in grid cells
c where sclr(ijk,1)=count in cell ijk
c * * * first initialize scalar array #1 to zero
      if(nsc.lt.1) goto 2000
            do 500 k=kprb,kprt
            do 500 j=jprf,jprbk
            do 500 i=iprl,iprr
      include '../comdeck/ijk.f'
      sclr(ijk,1)=zero
 500  continue
c * * * loop over particles to make the count
      do 1000 k1=1,itnps
c * * * skip particles that do not belong to this mesh block.
c If(ipmbl(k1).ne.nbe) goto 1000
            i=int(xp(k1))
            j=int(yp(k1))
            k=int(zp(k1))
      include '../comdeck/ijk.f'
      sclr(ijk,1)=sclr(ijk,1)+one

 1000 continue

 2000 continue

    return
    end
```

# Summary

Modelling of Flow Phenomena during DC Casting – Jan Zuidema

The production of aluminium ingots, by semi-continuous casting, is a complex process. DC Casting stands for direct chill casting. During this process liquid aluminium transforms to solid aluminium while cooling down. This is not an instantaneous transformation, but occurs in temperature interval. In the casting process the latent heat is moved away by convection and conduction. A number of problems may occur during solidification, because the solidification rate is rather high. The difference in density between liquid and solid aluminium is 7% and because of that solidification porosities may form during solidification when transport of liquid metal is insufficient. If besides this also high enough thermal stresses are present, cracks may be induced from these pores. The cracks, that originate during the solidification of the metal are called hot cracks. This in contradiction with cold cracks. These are formed due to high stress levels in the already solidified aluminium.

What happens from the moment that the casting process is started? This is one of the questions that is treated in this thesis. To be able to describe the DC Casting process, it is necessary to have a good model that describes the phenomena at hand adequately and that also enables to do predictions on process changes. The model, that is used , is based on the differential equations that describe the heat- and fluid dynamics transport. In chapter 2 a description of the model is given. Numerical methods for solving these equations are also given there. Without validation, a model is of little use. Model validation can be performed using various methods during DC Casting experiments. Temperature recordings enable to follow the evolution of the temperature during the casting- and solidification process in some important positions. Because part of the heat transport in the DC Casting process is convection driven, it is also important to find information on the flow pattern and velocities in the liquid aluminium. Various methods to evaluate velocities in liquid metals are described in chapter 2. Based on their use for measuring the molten aluminium velocity during DC Casting, a ranking of the methods is made.

Good boundary conditions are essential for reliable predictions of the behaviour of aluminium during the mould filling and subsequent solidification. In chapter 3 the determination of the most important boundary conditions is described. Those boundary conditions determine the amount of heat transport in that area of the system, where the heat transfer to the surroundings is the largest. Through sophisticated experiments the heat transfer from a plate of aluminium to

(boiling) water could be predicted. This heat transfer model enables the prediction of temperatures close to the surface of the solidifying aluminium. By instrumentation of the experimental casting facility with thermocouples, the temperature close to the surface of the ingot could be measured as function of time. Calculations using the casting- and solidification model with the constant heat transfer coefficients, and calculations with the new model for water cooling were performed. This showed, that in the first centimetres from the surface of the ingot the new model gives a better description of the experiment. Further away from the surface towards the centre of the billet, the constant heat transfer coefficient model is just as good as the new model.

The best method to measure liquid metal velocities during DC Casting is a method that is based on magnetic induction. The sensor to measure velocities is based on a ferro magnet, surrounded by a conduction tube with spot-welded thermocouples. Between two opposing thermocouples an inductive voltage is measured, which is proportional with the velocity of the surrounding medium. To test this method, a prototype of this sensor was constructed. In chapter 4 this sensor is described. The sensor was firstly tested in a water setup. Because the electrical conductivity of the water was several orders of magnitude less than that of liquid metals, this gave an unsatisfactory result. It was decided to perform fluid flow experiments in liquid tin. From these experiments results were obtained which gave a velocity dependent signal for the probe output. Unfortunately, electro-magnetical shielding from the surroundings was not good enough. This prevented to quantitatively test the sensor.

In chapter 5 the start-up phase of the casting is covered. In the first part of this chapter, a calculation described in the literature was repeated, using the casting- and solidification model. This showed that, due to lack of published data, more validation was necessary to fully validate the model. With the aid of the experimental casting facility, a number of casting experiments were conducted. The experiments were recorded with a video camera and the temperature during casting was recorded by thermocouples at a number of locations in the ingot. The experiments served as the basis for a number of calculations with the casting- and solidification model. A conclusion, that could be drawn from the combination of the results of the casting experiments and the calculations , was that the description of the inlet of the mould in the model as an jet of aluminium was a good description of reality during the first tenths of seconds of the process. From the moment that the aluminium melt level is overflowing the inlet level, the jet description is not accurate anymore and should be replaced with a filling over the complete width of the mould.

During casting, unwanted inclusions are filtered from the liquid aluminium by degassers and filters, before the casting table is reached. In order to comply with the increasing demands for the quality of cast products, an additional method to filter out particles from the launder system was evaluated. This is the subject of chapter 6. Manipulation of the flow pattern enables to create wakes, where particles can settle. Two dimensional calculations of the flow pattern in the mould with special flow modifiers, show that this settling is possible in theory. However, it is more likely, that transient velocity fluctuations prevent the settling of particles.

To create a better method for settling of unwanted inclusions, a cyclone was designed, which enables the separation of particles 20 micrometers in diameter from a stream of liquid aluminium. The cyclone was used in a series of calculations with the fluid-flow and solidification model. The outcome of these calculations has resulted in a patent for this type of cyclone. Validation measurements using a water model of the cyclone have confirmed the working of the cyclone in separation of denser particles out of a slow flowing medium. The velocity of the particles was therefore tracked using a laser and camera set-up. The laser exposed a two-dimensional area of the water model. By auto-correlation of two subsequent images, it was possible to extract the particulate rate in this area. Velocity patterns indicated, that particles had a tendency of settling down in the lower part of the cyclone. Because there was no possibility to count all particles going in and out of the system, no quantitative comparison with the model was possible.

# Samenvatting

Modelleren van Transport Verschijnselen tijdens DC Casting – Jan Zuidema

De productie van aluminium gietblokken, via een semi-continue gietmethode, is een complex proces. De gietmethode heet DC Casting, wat staat voor "direct chill" gieten. Dit is te vertalen als direct-afschrik-gieten in het Nederlands, maar de Engelse term wordt altijd gebruikt. Tijdens dit proces transformeert vloeibaar aluminium door koeling tot vast aluminium. Deze transformatie treedt niet instantaan op, maar vindt plaats over een temperatuur traject (stoltraject). De stollingswarmte wordt tijdens het gietproces door stroming en geleiding afgevoerd.. Omdat de afkoelsnelheid bij het gietproces relatief hoog is, kunnen zich een aantal problemen voordoen tijdens het stollen. Het verschil in dichtheid tussen vloeibaar en vast aluminium bedraagt 7%, waardoor tijdens de stolling porositeiten kunnen ontstaan als er onvoldoende toevoer van vloeibaar metaal is. Als daarnaast voldoend hoge thermische spanningen aanwezig zijn, kunnen uit deze porositeiten scheuren ontstaan. Deze scheuren die het gevolg zijn van verschijnselen tijdens het stollen, worden warmscheuren genoemd. Dit in tegenstelling tot koudscheuren. Deze worden gevormd door te hoog opgelopen thermische spanningen in het al gestolde aluminium.

Wat gebeurt er vanaf het moment dat met de gieting wordt begonnen? Dit is één van de vragen die in dit proefschrift worden behandeld. Om het proces van DC Casting goed te kunnen beschrijven is een model nodig dat de verschijnselen op adequate wijze beschrijft en waarmee ook voorspellingen kunnen worden gedaan. Het model, dat is gekozen, is gebaseerd op differentiaalvergelijkingen, die het warmtetransport en de vloeistofdynamica beschrijven. In hoofdstuk 2 wordt een opsomming van het model gegeven. Ook de implementatie van numerieke methoden wordt in dit hoofdstuk aangegeven. Zonder validatie heeft een model geen waarde. Validatie tijdens een gietproces kan op verscheidene manieren plaatsvinden. Door middel van temperatuursensoren kan op strategische plaatsen de temperatuur gemeten worden tijdens het giet- en stolproces. Omdat tijdens het gietproces een deel van het warmtetransport door stroming gebeurt, is het belangrijk informatie te vergaren over de snelheid in het vloeibare aluminium. Diverse methoden om snelheden te bepalen worden in hoofdstuk 2 beschreven en aan een selectiecriterium onderworpen.

Om met het giet- en stollingsmodel betrouwbare voorspellingen over het gedrag van aluminium tijdens de vormvulling en het stolproces te verkrijgen, is van belang goede randvoorwaarden te definiëren. Hoofdstuk 3 beschrijft het

bepalen van de belangrijkste randvoorwaarden voor het model. Deze randvoorwaarden bepalen het warmtetransport dat plaatsvindt in het gebied met de grootste warmteoverdracht naar de omgeving. Door geavanceerde experimenten was het mogelijk de warmteoverdracht van een plaat aluminium naar (kokend) water te voorspellen. Met deze benadering blijkt het mogelijk te zijn nauwkeurig de temperatuur dicht bij de wand van het stollende aluminium te kunnen beschrijven. Door de experimentele gietinstallatie met thermokoppels te instrumenteren kan de temperatuur dicht bij het stolfront worden gevolgd als functie van tijd. Berekeningen met het giet- en stolmodel via constante warmteoverdrachts-coëfficiënten en met het nieuwe model voor waterkoeling gaven aan dat in het eerste tiental millimeters van de wand van de gieting het nieuwe model een betere beschrijving geeft. Verder van de wand af zijn de constante warmteoverdrachts-modellen net zo goed als het nieuwe model.

De meest geschikte methode om snelheden te meten uit hoofdstuk 2 is een methode die berust op inductie. Deze snelheidssensor bestaat uit een ferromagneet, waaromheen een geleidende huls is aangebracht met een aantal thermokoppels. Tussen deze thermokoppels ontstaat een inductieve spanning, die proportioneel is met de snelheid van het omringende medium. Om daadwerkelijk metingen in vloeibaar metaal uit te kunnen voeren is op basis van dit principe een meetsensor vervaardigd, die in hoofdstuk 4 wordt beschreven. Deze meetsensor is eerst getest in een waterbak. Daar de geleiding van zout water erg laag is ten opzichte van vloeibaar metaal, gaf dit geen bevredigend resultaat. Besloten is toen om de experimenten voort te zetten in vloeibaar tin. Dit gaf een snelheidsafhankelijk resultaat. Een teleurstelling was echter, dat door onvoldoende afscherming niet met zekerheid kon worden vastgesteld hoe de sensor kwantitatief werkte.

In hoofdstuk 5 wordt gekeken naar de startfase van de gieting. Eerst is een in de literatuur beschreven experiment en berekening nagebootst met behulp van het giet- en stolmodel. Dit gaf aan dat het model verder gevalideerd moest worden, omdat niet alle noodzakelijke parameters gecontroleerd konden worden op basis van de publicatie. Met hulp van de experimentele gietinstallatie werden daarom een aantal gietingen uitgevoerd, die met hulp van een video camera zijn gefilmd en waarvan de temperatuur op een aantal plaatsen in de gietvorm zijn gevolgd. De experimenten dienden als basis voor een aantal berekeningen met het giet- en stolmodel. Een conclusie, die volgde uit berekeningen in combinatie met de metingen was, dat de beschrijving van de instroomopening in het model met een straal aluminium voldeed voor het eerste tiental seconden van de gieting. Vanaf het moment dat de instroomopening overstegen werd door het aluminium niveau in de gietvorm, was een vulling over de gehele breedte van de aanvoergoot beter.

In de praktijk worden via filters en ontgassers ongewenste insluitsels uit het vloeibare aluminium verwijderd, voordat de gietvorm wordt bereikt. Om te kunnen blijven voldoen aan de extreem kritische kwaliteitseisen van gegoten producten voor sommige toepassingen, is gekeken naar een additionele filtermethode voor het vloeibare aluminium, voordat het de gietvorm bereikt. Dit is gedaan in hoofdstuk 6. Door modificatie van het stromingspatroon lijkt het

mogelijk deeltjes te laten bezinken in gebieden met lage stroomsnelheden. Tweedimensionale berekeningen laten zien dat dit in principe mogelijk is. Het lijkt echter waarschijnlijk dat optredende snelheidsfluctuaties dit bezinkgedrag kunnen verstoren. Om een betere methode van bezinken te creëren is een cycloon ontworpen die deeltjes met een diameter groter dan 20 micrometer uit een langzaam stromende aluminiumstroom weet te scheiden. Op basis van dit ontwerp zijn berekeningen met het stromings en stolmodel gedaan. De resultaten hebben geresulteerd in een octrooi. Latere validatiemetingen met behulp van een watermodel van de cycloon bevestigen het scheidingsgedrag kwalitatief. De snelheid van de deeltjes in het watermodel werd daarvoor met behulp van een camera gevolgd. Een tweedimensionaal vlak in het watermodel werd belicht met een laser. Door twee beelden kort na elkaar met elkaar te correleren was de snelheid in dit vlak vast te stellen. Snelheidspatronen gaven aan of deeltjes neiging hadden te bezinken in bepaalde gebieden van de cycloon. Doordat het niet mogelijk was de deeltjes te tellen, kon geen kwantitatieve vergelijking met het numerieke model worden gemaakt.

# List of Publications

## Journal

1. Eskine, D; Zuidema, J; Katgerman, L, Linear solidification contraction of binary and commercial aluminium alloys, International Journal of Cast Metals Research (UK). Vol. 14, no. 4, pp. 217-224. 2001

2. Zuidema, J Jr; Katgerman, L, Upstream fluid flow effects in aluminium DC casting, Materials Science Forum (Switzerland). Vol. 396-402, Part 1, pp. 65-70. 2002

3. Eskin, D G; Zuidema, J; Savran, V I; Katgerman, L, Structure formation and macrosegregation under different process conditions during DC casting, Materials Science and Engineering A. Vol. 384, no. 1-2, pp. 232-244. 25 Oct. 2004

## Conference Proceedings

1. Zuidema, J., Jr. and L. Katgerman, Modelling metal-entry in the DC cast process using Flow-3D., in Modelling of Casting, Welding and advanced Solidification Processes IX, P.R. Sahm, P.N. Hansen, and J.G. Conley, Editors. 1999, Shaker Verlag GmbH: Aachen. p. 789-796.

2. Zuidema, J., Jr., I.J. Opstelten, and L. Katgerman, Boiling Curve Approach for Thermal Boundary Conditions in DC Casting, in Continuous Casting, K. Ehrke and W. Schneider, Editors. 2000, DGM/WIley-VCH, Weinheim, Germany. p. 138-142..

3. Zuidema, J; Katgerman, L; Opstelten, I J; Rabenberg, J M, Secondary cooling in DC casting: modeling and experimental results, Light Metals 2001 as held at the 130th TMS Annual Meeting; New Orleans, LA; USA; 11-15 Feb. 2001. pp. 873-878. 2001

4. Katgerman, L; Eskin, D G; Venneker, B C H; Zuidema, J; Suyitno, Experimental description and process simulation of direct chill (DC) casting of aluminum alloys, Eighth Australasian Conference on Aluminum Cast House Technology; 2003

5. Katgerman, L.; Eskin, D.G.; Venneker, B.C.H.; Zuidema, J.; Suyitno, Experimental description and process simulation of direct chill (DC) casting of aluminum alloys, Eighth Australasian Conference on Aluminum Cast House Technology; Brisbane; Australia; 14-17 Sept. 2003. pp. 243-257. 2003

6. Zuidema, J; Katgerman, L, Cyclone separation of particles in aluminium DC casting, Modeling of Casting, Welding and Advanced Solidification Processes - X; Destin, FL; USA; 25-30 May 2003. pp. 607-614. 2003

7. Katgerman, L; Venneker, B; Zuidema, J, Modelling of fluid flow phenomena during dc casting of aluminium alloys, Light Metals 2003 as held at the 132nd TMS Annual Meeting; San Diego, CA; USA; 2-6 Mar. 2003. pp. 815-820. 2003

8. Eskin, D G; Zuidema Jr, J; Savran, V I; Katgerman, L, Effect of Process Parameters on Structure Formation during Direct-Chill Casting of an Al-Cu Alloy, Materials Forum. Vol. 28, pp. 487-493. 2004

9. Katgerman, Laurens; Zuidema Jr, Jan, UPSTREAM FLUID FLOW PARTICLE REMOVAL, Light Metals 2005 as held at the 134th TMS Annual Meeting; San Francisco, CA; USA; 13-17 Feb. 2005. pp. 927-931. 2005

## Patent

Zuidema, J, Molten metal purifying method e.g. for aluminum, involves generating spiral flow within chamber to purify molten metal introduced into chamber, and discharging purified metal vertically through outlet placed above inlet, WO2004001078-A1; NL1020919-C2; AU2003248155-A1, NETHERLANDS INST METALS RES (NEME-Non-standard)

# Dankwoord

Zoals menig promovendus kan beamen is het doen van een promotie onderzoek geen kluizenaarswerk. Voor het doen van zowel experimenten als computerberekeningen is de hulp van anderen vaak hard nodig. Behalve het "harde zwoegen" zijn er natuurlijk ook nog de informele zaken zoals koffiepauzes, borrels, recepties en andere ontspannende activiteiten. Ik wil proberen in dit dankwoord degenen die mij in de afgelopen jaren met mij hebben gewerkt of op andere manier aan de tot stand koming van dit proefschrift hebben bijgedragen te bedanken voor hun bijdrage.

Ik wil beginnen met de LMP groep van de afdeling Materiaalkunde. Alweer een aantal jaren terug, in 1997 besloot ik dat ik mij met proces simulatie wilde gaan bezighouden. Ik ben toen bij Laurens Katgerman langsgegaan en heb hem gevraagd of er een mogelijkheid was in zijn groep een afstudeeropdracht en stage te doen. Dit resulteerde, mede via contacten van mijn vader, in een stage aan de Universiteit van Waterloo waar ik mij met facetten van lasbadsimulatie bezighield. Mijn afstudeerwerk wat daarna volgde had als doel de vormvulling van dunwandige gietstukken met nodulair gietijzer te beschrijven. De samenwerking met Laurens beviel goed en begin 1999 besloot ik via het nog jonge NIMR te gaan promoveren op het vloeistofstromingsgedrag van aluminium tijdens het DC Casting proces. Ik kwam op een kamer te zitten met Bart Venneker. Bart was als post-doc een goede vraagbaak voor allerhande problemen betreffende modelleren. Dmitri Eskin heeft de experimentele gietinstallatie die al jaren niet was gebruikt op orde te gebracht voor onder andere de validatie experimenten. Dit viel niet mee omdat een jaar lang de hall door asbestsanering afgesloten was geweest en de nodige spullen waren verdwenen. Zonder Jack Jansen, Jan van Etten en Tjeerd Tobi zou dit waarschijnlijk heel lang hebben geduurd, maar nu ging de opbouw van de installatie vrij snel. Dmitry, Jack en Jan hebben tijdens mijn promotie vele experimenten gedaan, die goed inzicht in het DC Casting proces hebben verschaft.

Verder wil ik natuurlijk alle promovendi, post-docs en medewerkers bedanken voor de gezelligheid tijdens de koffiepauzes en borrels. De laatste jaren zaten Suyitno en Onno Dijkstra de kamer naast mij te ploeteren. Ik kon ze altijd storen voor een gezellig praatje. Het laatste jaar kwam Simon Edwards op mijn kamer te zitten. Simon, het was altijd gezellig.

Bij het NIMR kwam ik nog wel eens bij Oscar Ruigrok langs ivm financiële regelingen. Eerst moest je dan langs Shanna en Margo zien te komen, die Oscar afschermden van opdringende collega's. Erik van Westing, die allerlei organisatorische dingen voor me regelde zoals onder andere een octrooiaanvrage

wil ik hier niet vergeten. Ook wil ik hier natuurlijk Sieb Radelaar bedanken, die mij na een pittig solicitatiegesprek aannam bij het NIMR.

Verder waren er nog de afstudeerders, die allemaal voor de KdW bokaal gingen. Dit waren Richard "Amaretto" van der Meij, Johan van Boggelen en Robert Gouwen. Wie gewonnen heeft laat ik in het midden, maar ze brachten wel veel leven in de brouwerij.

Omdat het NIMR als top-instituut het raakvlak tussen industrie en universiteit vertegenwoordigt, was er ook veel samenwerking met onderzoekers van Corus. In het begin van mijn onderzoek heb ik onder begeleiding van Ivo Opstelten gewerkt aan het invers modelleren van randvoorwaarden voor warmteoverdracht. Later kwam ik via technisch kwartaaloverleg in contact met Heiko Sportel en Wim Boender. Het waren altijd levendige discussies tijdens deze bijeenkomsten. Heiko ging naar een andere functie en zijn plaats werd ingenomen door René Kieft. Via René leerde ik het een en ander van PIV; bedankt daarvoor. Als laatste van Corus wil ik Sjaak van Oord bedanken, die mij met de waterbaksexperimenten heeft geholpen.

Mijn ouders, Jan en Rita, en broer Joost wil ik bedanken voor het doorlezen van het manuscript. Wetenschappelijk had mijn vader een goede inbreng en mijn moeder en broer konden van een grotere afstand beter over het geheel oordelen.

Ten slotte wil ik mijn steun en toeverlaat in moeilijke tijden bedanken, mijn lieve Suzanne. Mij nooit haastend heb je met geduld gewacht op het typen van de laatste punt van dit proefschrift. In het laatste jaar van mijn werkzaamheden voor het NIMR hebben wij samen het mooiste gekregen wat er is. Tom, je beseft het nu nog niet zo, maar jij brengt de zon in ons leven. Jouw broertje of zusje is nu aan het groeien bij mama in de buik en zal hopelijk net zo'n gezond en lief kind worden als jij bent.

# Curriculum vitae

## Jan Zuidema

geboren op 27 april 1974 te Rotterdam

1986 - 1992   VWO, Melanchthon College te Rotterdam

1992 - 1999   Studie Materiaalkunde aan de Technische Universiteit Delft. Afstudeerrichting Productie Technologie. Afstudeeronderzoek naar dunwandig gieten van nodulair gietijzer onder begeleiding van Prof. ir. L. Katgerman.

1999 - 2005   Promotie-onderzoek "Modelling of Flow Phenomena during DC Casting" uitgevoerd in de sectie "Light Metals Processing" van het laboratorium voor Materiaalkunde aan de Technische Universiteit Delft, onder begeleiding van Prof. ir. L. Katgerman.

2003 - heden   Researcher Ironmaking bij Corus RD&T te IJmuiden